Simulations of Systems of Cold Rydberg Atoms

Simon James Thwaite

A thesis submitted in partial fulfilment of
the requirements for the degree of
Doctor of Philosophy at the University of Oxford

Balliol College
University of Oxford
Trinity Term 2012

Simulations of Systems of Cold Rydberg Atoms

Simon James Thwaite, Balliol College, University of Oxford

A thesis submitted in partial fulfilment of the requirements for the degree of Doctor of Philosophy at the University of Oxford, Trinity Term 2012

Abstract

The past three decades have seen extraordinary progress in the manipulation of neutral atoms with laser light, to the point where it is now routine to trap and cool both individual atoms and entire atomic clouds to temperatures of only a few tens of nanoKelvin in a controlled and repeatable fashion. In this thesis we study several applications of Rydberg atoms – atoms with an electron in a highly excited state – within such ultracold atomic systems. Due to their highly-excited electron, Rydberg atoms have a number of exaggerated properties: in addition to being physically large, they have long radiative lifetimes, and interact strongly both with one another and with applied external fields. Rydberg atoms consequently find many interesting applications within ultracold atomic physics.

We begin this thesis by analysing the way in which a rubidium atom prepared in an excited Rydberg state decays to the ground state. Using quantum defect theory to model the wavefunction of the excited electron, we compute branching ratios for the various decay channels that lead out of the Rydberg states of rubidium. By using these results to carry out detailed simulations of the radiative cascade process, we show that the dynamics of spontaneous emission from Rydberg states cannot be adequately described by a truncated atomic level structure.

We then investigate the stability of ultra-large diatomic molecules formed by pairs of Rydberg atoms. Using quantum defect theory to model the electronic wavefunctions, we apply molecular integral techniques to calculate the equilibrium distance and binding energy of these molecular Rydberg states. Our results indicate that these Ryberg macro-dimers are predicted to show a potential minimum, with equilibrium distances of up to several hundred nanometres.

In the second half of this thesis, we present a new method of symbolically evaluating functions of matrices. This method, which we term the method of path-sums, has applications to the simulation of strongly-correlated many-body Rydberg systems, and is based on the combination of a mapping between matrix multiplications and walks on weighted directed graphs with a universal result on the structure of such walks. After presenting and proving this universal graph-theoretic result, we develop the path-sum approach to matrix functions. We discuss the application of path-sums to the simulation of strongly-correlated many-body quantum systems, and indicate future directions for the method.

To my parents, for all their love and support.

Contents

Chapter 1

Introduction

In this thesis we study several applications of Rydberg atoms in ultracold atomic systems. We begin with an overview of the field of ultracold atoms and a discussion of the main properties of Rydberg atoms that make them attractive for study. We then present a summary of quantum defect theory, which we use in several parts of this thesis to model the electronic wavefunctions of atoms in Rydberg states. We conclude with a summary of the work presented in each chapter of this thesis.

1.1 Rydberg atoms in cold-atom physics

Spectacular progress over the past two decades in the laser cooling and trapping of neutral atoms (see e.g. [1, 2, 3, 4] and references therein) has advanced the field to the point where the experimental preparation and characterisation of trapped collections of ultracold atoms under a wide range of conditions is now routine. These capabilities have opened the door to an exciting new era in physics, in which the coherent interaction of cold atoms with laser light can be used as a resource to engineer systems of particular scientific or technological interest.

Foremost among the attractive properties of systems of cold atoms interacting with light is their extreme versatility, which is the product of a detailed theoretical understanding of light-matter interactions combined a high degree of experimental control. As a consequence of this flexibility, atom-light systems find applications in areas of physics that cover the full spectrum from topics of fundamental academic interest to projects of real-world technological significance. Active areas of research in recent years include the use of atom interferometry for precision tests

of fundamental physical theories [5, 6], the use of cold atoms in optical lattices for simulating strongly-correlated many-body systems [7, 8, 9], the development of a robust and scalable atom- or ion-based architecture for quantum information processing [10, 11], and the development of next-generation atomic clocks for the definition of a universal time standard [12, 13].

One topic that is currently the focus of significant attention within the field of ultracold atoms is the study of Rydberg atoms [14, 15, 16]. A Rydberg atom is an atom with an electron in an excited state with principal quantum number $n_{\rm Ryd} \gg 1$. Rydberg atoms have a number of exaggerated physical properties: they are large, with a radius proportional to $n_{\rm Ryd}^2$; they have a long lifetime against spontaneous emission, which scales as $n_{\rm Ryd}^3$; and they interact strongly both with external fields and with other Rydberg atoms. This latter interaction has a distinctive nature, and is the foundation for a large part of the popularity of this field of study.

Rydberg atoms interact with one another primarily through the dipole-dipole interaction [17], and the interaction between two Rydberg atoms can be made many orders of magnitude larger than between two ground-state atoms. In the absence of an external electric field and resonant effects, the dominant interaction for large values of the interatomic separation R is of off-resonant dipole (van-der-Waals) form. In this case the potential energy between a pair of atoms with the same value of the angular momentum quantum number ℓ is C_6/R^6 for $\ell = 0$, or C_5/R^5 for $\ell = 1, 2$, where C_n is a state-dependent constant with dimensions of $\big[\text{energy}\big]/\big[\text{length}\big]^n$ [18, 19, 20]. The coefficient C_6 (C_5) scales with the Rydberg quantum number as $n_{\rm Ryd}^{11}$ ($n_{\rm Ryd}^{8}$).

At smaller values of R such that the interaction energy is the dominant energy scale (i.e. when the interaction exceeds the spacing between the energy levels) the character of the interaction is that of a resonant dipole-dipole interaction, for which the leading-order term is C_3/R^3. This resonant enhancement of the interaction strength may also be artificially engineered by carefully choosing a suitable pair of Rydberg states [21, 22, 23], or by using the AC or DC Stark shift to tune pairs of nearly-degenerate states into resonance with one another [24, 25, 26, 27].

These strong long-range interactions give rise to a wide range of interesting physics within systems that contain multiple Rydberg atoms. One spectacular example of recent interest is the blockade effect, where the simultaneous excitation of two Rydberg atoms in close proximity is suppressed by the strong Rydberg-Rydberg interaction. This occurs when the interaction shift of the doubly-excited state $|r\rangle \otimes |r\rangle$ is much larger than $\hbar\Omega$, where Ω is the Rabi frequency for the

single-atom transition $|g\rangle \longleftrightarrow |r\rangle$. In this case, the doubly-excited state is shifted out of resonance with the exciting laser. The Rydberg blockade has recently been experimentally observed between a pair of trapped rubidium atoms separated by distances of up to 10 μm [28, 29].

The conditional atomic dynamics and 'excitation saturation' that characterise the Rydberg blockade have inspired proposals for a broad range of applications, including deterministic single-atom and single-photon sources [30, 31] and neutral-atom quantum information processing schemes [32, 33, 34, 35, 36]. The blockade effect also generalises in a straightforward fashion to systems of more than two atoms [37], where it is relevant in the regime in which the atomic interactions are strong enough to shift all multiply-excited states out of resonance with the incident laser. Recent proposals for the use of the multi-atom blockade include the preparation of many-particle entanglement [38, 39, 40, 41], the preparation of collectively-encoded qubits [42, 43], and the simulation of dissipative many-body quantum systems [44, 45].

In addition to granting a better understanding of the blockade effect, studies of the interaction potential between Rydberg states have opened the door to the study of exotic long-range molecules that contain one or more Rydberg atoms. Recent theoretical investigations have led to the prediction of two classes of such molecules. The first, which are known as trilobite molecules due to the startling spatial complexity of their wavefunctions, are composed of a Rydberg atom interacting with another atom in its ground state [46, 47]. These molecules are relatively weakly bound, and – uniquely for homonuclear diatomic molecules – are predicted to have a large electric dipole moment. They have recently been observed in experiments [48, 49]. The second class of molecules consist of a pair of Rydberg atoms stabilised by purely long-range interactions [50, 51, 52, 53]. These molecules have been termed macrodimers due to their ultralarge internuclear distances, and have recently been experimentally observed [54].

Rydberg-Rydberg interactions are also of significant interest within larger systems that comprise many hundreds or thousands of atoms. The strong, long-range nature of the interaction between Rydberg states means that it is relatively simple to prepare such a system in a regime where the dominant energy scale is that of the interactions. This can be done, for example, by using a short laser pulse to resonantly excite ground-state atoms from a cold atomic cloud or a Mott insulator state to a strongly-interacting Rydberg state. The resulting strongly correlated Rydberg gases have been predicted to exhibit such many-body effects as a second-order

quantum phase transition [55] and strong spatial correlations between Rydberg excitations [56, 57, 58, 59]. Evidence for the experimental observation of mesoscopic crystalline structures in a laser-excited two-dimensional Mott insulator has very recently been reported [60].

Simulating the full many-body dynamics of these strongly correlated Rydberg systems is complicated by the fact that the dimension of the Hilbert space describing the system increases exponentially with the number of atoms. Consequently, directly integrating the many-body Schrödinger equation is only computationally feasible for small systems [61, 62]. As a result, a number of more powerful theoretical and computational methods have been developed over the past two decades. Among the most commonly used techniques applied in this field are density-matrix renormalisation group (DMRG) algorithms [63, 64] and related tensor-network approaches (see [65] for a review). While these techniques have been very successful within their domains of applicability, they are typically limited to one-dimensional systems with nearest-neighbour interactions, and are therefore not as naturally applied to strongly-correlated Rydberg systems as to – for example – systems of spins arranged on a lattice. Though attempts to extend tensor-network methods to two- and three-dimensional systems are ongoing [66], these efforts are yet to produce techniques with widespread applicability. There is therefore a strong need for the development of new theoretical approaches to simulating the quantum dynamics of strongly-correlated Rydberg gases in two and three dimensions.

1.2 Rydberg states of alkali atoms

In this section we provide a concise summary of the key properties of Rydberg states of alkali atoms, focusing on the use of quantum defect theory to describe the Rydberg energies and wavefunctions. More complete accounts of the properties of Rydberg atoms can be found in dedicated references such as [14, 15, 17].

1.2.1 Overview

The alkali metals lithium, sodium, potassium, rubidium, and francium have an electronic configuration in which all but one of the electrons occupy full shells. Together with the atomic nucleus, these electron shells form a stable ionic core with a net electric charge of $+e$. The remaining electron, which is responsible for the majority of the optical, physical, and chemical properties of the atom, is

decoupled from this ionic core. The energy eigenstates of the single valence electron are hydrogenic in character, and are characterised by the hydrogenic quantum numbers n, ℓ, m_ℓ. They can be well approximated by using the results of quantum defect theory.

Quantum defect theory is based on the following observations. Far from the core, the $+Ze$ charge of the nucleus is effectively shielded by the $Z-1$ inner core electrons, and the potential experienced by the valence electron is indistinguishable from the Coulomb potential of a single proton. At shorter distances, however, the valence electron penetrates and polarises the inner electron cloud and is exposed to a greater fraction of the nuclear charge. The potential seen in this region is therefore deeper than the Coulomb potential. As a consequence, the energy levels of an alkali atom are depressed in comparison with hydrogen, and their wavefunctions are pulled closer to the nucleus.

For many applications it is not important to know the exact form of the eigenfunctions within the core region. This is particularly true for Rydberg states, where the large spatial extent of the atomic orbitals mean that physical observables are largely insensitive to the short-range behaviour of the wavefunction. In this case it is acceptable to treat the potential within the core region as a 'black box', the net effect of which is to drag the wavefunction closer to the nucleus.

These effects are conveniently characterised by a single parameter $\mu_{n,\ell}$ known as the quantum defect, which is essentially a measure of the overall deviation of the true potential seen by the valence electron in the state n, ℓ from a pure Coulomb potential. Introducing the quantum defect encapsulates the effect of the complicated potential inside the core region in a single parameter, analogously to the manner in which the s-wave scattering length characterises the net effect of a scattering potential at low collision energies.

In the following section we present an overview of quantum defect theory as it applies to alkali atoms. We work in atomic units (summarised in Table 1.1) throughout, and neglect the atomic fine structure and other relativistic effects.

1.2.2 The hydrogen atom

We begin by summarising the well-known results for the energies and eigenstates of the hydrogen atom.

Quantity	Atomic unit	Value (7 s.f.)
length	$a_0 = 4\pi\epsilon_0\hbar^2/(m_\mathrm{e}\mathrm{e}^2)$	5.291 772 $\times 10^{-11}$ m
mass	m_e	9.109 382 $\times 10^{-31}$ kg
energy	$E_\mathrm{h} = \mathrm{e}^2/(4\pi\epsilon_0 a_0)$	4.359 744 $\times 10^{-18}$ J
time	$\hbar/E_\mathrm{h}$	2.418 884 $\times 10^{-17}$ s
angular momentum	$\hbar$	1.054 572 $\times 10^{-34}$ J·s
charge	e	1.602 176 $\times 10^{-19}$ C
electric dipole moment	$a_0\mathrm{e}$	8.478 353 $\times 10^{-30}$ C·m

Table 1.1: The atomic units of several common physical quantities. Definitions and numerical values are taken from the CODATA 2006 recommended values [67].

Energy spectrum

In atomic units, the energy levels of the hydrogen atom are given by

$$\varepsilon_{n,\ell} = -\frac{1}{2n^2}, \tag{1.1}$$

where $n = 1, 2, 3, \ldots$ is the principal quantum number. Since the energy is independent of the orbital angular momentum quantum number ℓ and the magnetic quantum number m_ℓ, the energy E_n is n^2-fold degenerate.

The Schrödinger equation for the Coulomb potential

The Schrödinger equation for a single electron moving in the Coulomb potential of an atomic nucleus of infinite mass and charge +1 is

$$\left[\nabla^2 + \frac{2}{r} + 2\varepsilon\right]\psi(r,\theta,\phi) = 0, \tag{1.2}$$

where ∇^2 is the Laplacian operator, and ε is the energy. By introducing the angular momentum operator $\mathbf{L} = -\mathrm{i}\mathbf{r}\times\nabla$, this equation may be recast as

$$\left[\frac{1}{r^2}\frac{\partial}{\partial r}\left(r^2\frac{\partial}{\partial r}\right) - \frac{|\mathbf{L}|^2}{r^2} + \frac{2}{r} + 2\varepsilon\right]\psi(r,\theta,\phi) = 0. \tag{1.3}$$

This differential equation is separable in spherical coordinates. It has solutions [68]

$$\psi(r,\theta,\phi) = \frac{\chi_{\varepsilon,\ell}(r)}{r}\,Y_\ell^m(\theta,\phi), \tag{1.4}$$

where $Y_\ell^m(\theta,\phi)$ is a spherical harmonic satisfying

$$|\mathbf{L}|^2\, Y_\ell^m(\theta,\phi) = \ell(\ell+1)\, Y_\ell^m(\theta,\phi), \tag{1.5a}$$

$$L_z\, Y_\ell^m(\theta,\phi) = m\, Y_\ell^m(\theta,\phi), \tag{1.5b}$$

where ℓ and m are integers satisfying $\ell = 0, 1, 2, \ldots$ and $-\ell \leq m \leq \ell$. The reduced radial wavefunction $\chi_{\varepsilon,\ell}(r)$ satisfies the equation

$$\left[\frac{\mathrm{d}^2}{\mathrm{d}r^2} - \frac{\ell(\ell+1)}{r^2} + \frac{2}{r} + 2\varepsilon\right] \chi_{\varepsilon,\ell}(r) = 0. \tag{1.6}$$

An overview of the solutions to Eq. (1.6) is given in Appendix A. Neglecting normalisation, which we will consider later, the general solution can be written as

$$\chi_{\varepsilon,\ell}(r) = \cos\pi\delta\; s(\varepsilon,\ell;r) + \sin\pi\delta\; c(\varepsilon,\ell;r), \tag{1.7}$$

where $s(\varepsilon,\ell;r)$ and $c(\varepsilon,\ell;r)$ are the regular and irregular Coulomb functions defined in Eq. (A.22a), and δ is a constant to be fixed by the boundary conditions imposed on $\chi_{\varepsilon,\ell}(r)$. In what follows, we are primarily interested in the atomic bound states; we therefore substitute the negative-energy forms of $s(\varepsilon,\ell;r)$ and $c(\varepsilon,\ell;r)$ (see Eq. (A.24)) into Eq. (1.7) to obtain the general solution to Eq. (1.6) for $\varepsilon < 0$:

$$\begin{aligned}\chi_{\varepsilon,\ell}(r) = \frac{(-1)^\ell}{\pi(2\nu)^{1/2}K(\nu,\ell)}\; &\sin\pi(\nu+\delta)\,\xi(\nu,\ell;r) \\ &- (-1)^\ell \left(\frac{\nu^3}{2}\right)^{1/2} K(\nu,\ell)\cos\pi(\nu+\delta)\,\Theta(\nu,\ell;r),\end{aligned} \tag{1.8}$$

where $\nu = (2|\varepsilon|)^{-1/2}$ is the effective quantum number corresponding to the energy ε. For future convenience, we note that the functions $\xi(\nu,\ell;r)$ and $\Theta(\nu,\ell;r)$ have asymptotic behaviour

$$\xi(\nu,\ell;r) \overset{r\to\infty}{\sim} (2r/\nu)^{-\nu}\,\mathrm{e}^{r/\nu}, \tag{1.9a}$$

$$\Theta(\nu,\ell;r) \overset{r\to\infty}{\sim} (2r/\nu)^{\nu}\,\mathrm{e}^{-r/\nu}. \tag{1.9b}$$

Bound-state wavefunctions for hydrogen

The bound-state wavefunctions of hydrogen are obtained by combining Eq. (1.8) with the boundary conditions

$$\chi_{\varepsilon,\ell}(r) \xrightarrow{r\to 0} 0, \tag{1.10a}$$

$$\chi_{\varepsilon,\ell}(r) \xrightarrow{r\to \infty} 0. \tag{1.10b}$$

The first of these conditions can only be satisfied if $\chi_{\varepsilon,\ell}(r)$ contains no component of the irregular function $c(\varepsilon,\ell;r)$. From Eq. (1.7), we see that this is the case whenever δ is equal to an integer; without loss of generality, we set $\delta = 0$. In order to satisfy the second boundary condition, we note that Eq. (1.9) implies that $\chi_{\varepsilon,\ell}(r)$ diverges as $r \to \infty$ unless the coefficient of $\xi(\nu,\ell;r)$ in Eq. (1.8) is identically zero; i.e. we require $\sin \pi\nu / K(\nu,\ell) = 0$. This condition is satisfied for $\nu = n$, with $n = \ell+1,\ \ell+2, \ldots$. Thus the reduced radial wavefunctions $\chi_{n,\ell}(r)$ for the bound states of hydrogen are given by

$$\chi_{n,\ell}(r) = (-1)^{n+\ell+1} \left(\frac{n^3}{2}\right)^{1/2} K(n,\ell)\, \Theta(n,\ell;r). \tag{1.11}$$

for $n = 1, 2, \ldots$ and $\ell = 0, 1, \ldots, n-1$. The corresponding energy eigenvalues are

$$\varepsilon_{n,\ell} = -\frac{1}{2n^2}. \tag{1.12}$$

1.2.3 Alkali atoms

We now consider the quantum defect theory approach to obtaining the energy eigenfunctions of the bound states of alkali atoms. More complete treatments can be found in [69, 70, 71, 72], which further include a wider range of applications of quantum defect theory.

Energy spectrum

The energy $\varepsilon_{n,\ell}$ of a Rydberg state of an alkali atom with principal quantum number $n \gg 1$ and angular momentum quantum number ℓ is well approximated by

$$\varepsilon_{n,\ell} = -\frac{1}{2(n-\mu_{n,\ell})^2}, \tag{1.13}$$

where $\mu_{n,\ell}$ is the quantum defect. The effect of the quantum defect is to lower the energy of the (n,ℓ) manifold as compared with the case of hydrogen. This energy shift is a result of the increased nuclear charge seen by the Rydberg electron in the period of time it spends within the core electron cloud. The quantum defect for a given atomic species depends strongly on ℓ, since states with low ℓ (which correspond to highly elliptical classical orbits) spend a greater proportion of their time inside the core region than high angular momentum states. The quantum defect decreases with increasing ℓ, and is typically negligible for $\ell \gtrsim 3$. For fixed ℓ the quantum defect depends only weakly on n, and is conveniently parametrised as

$$\mu_{n,\ell} = \mu_0 + \frac{\mu_2}{(n-\mu_0)^2} + \frac{\mu_4}{(n-\mu_0)^4} + \frac{\mu_6}{(n-\mu_0)^6} + \cdots \tag{1.14}$$

where for most practical purposes it is sufficient to keep only the first two terms.

Bound-state wavefunctions for alkali atoms

Quantum defect theory provides a method of obtaining analytical approximations for the excited-state wavefunctions of alkali atoms. These eigenfunctions are valid for radial distances $r > r_0$, where r_0 is the size of the atomic core. In this region, the potential seen by the valence electron is well approximated by the Coulomb potential of a single proton, and the energy eigenfunctions are given by Eq. (1.4). For bound states ($\varepsilon < 0$) we have, from Eq. (1.8),

$$\chi_{\varepsilon,\ell}(r) = \frac{(-1)^\ell}{\pi(2\nu)^{1/2}K(\nu,\ell)} \sin\pi(\nu+\delta)\,\xi(\nu,\ell;r) - (-1)^\ell \left(\frac{\nu^3}{2}\right)^{1/2} K(\nu,\ell)\cos\pi(\nu+\delta)\,\Theta(\nu,\ell;r), \tag{1.15}$$

where δ is a constant to be fixed by the boundary conditions imposed on $\chi_{\varepsilon,\ell}(r)$.

Since Eq. (1.15) is valid only for $r > r_0$, the bound-state wavefunctions of alkali atoms satisfy slightly different boundary conditions to those of hydrogen. The condition $\chi_{\varepsilon,\ell}(r) \xrightarrow{r\to\infty} 0$ is still valid, but the requirement that $\chi_{\varepsilon,\ell}(r)$ vanishes as $r \to 0$ is lifted. It is instead replaced—at least, in cases where the wavefunction in the inner core region is known—by the requirement that the inner- and outer-core pieces of the radial wavefunction are joined smoothly across $r = r_0$.

In the present case we do not calculate the wavefunction within the inner core region, and so we do not use this boundary condition. Instead we impose the (equiv-

alent) condition that the energy eigenvalues of the bound states should reproduce the experimentally observed energy levels of Eq. (1.13):

$$\varepsilon = -\frac{1}{2(n-\mu_{n,\ell})^2}. \tag{1.16}$$

The $r \to \infty$ boundary condition is satisfied if $\sin \pi(\nu+\delta)/K(\nu,\ell) = 0$, or $\nu+\delta = n$, with $n = \ell+1, \ell+2, \ldots$. In this case, the $\chi_{n,\ell}(r)$ contains only the decaying exponential $\Theta(\nu,\ell;r)$, and is a solution to Eq. (1.6) with energy eigenvalue

$$\varepsilon = -\frac{1}{2\nu^2} = -\frac{1}{2(n-\delta)^2}. \tag{1.17}$$

The energy eigenvalues therefore reproduce the observed series if δ is set equal to the quantum defect $\mu_{n,\ell}$. The reduced radial wavefunctions $\chi_{n,\ell}(r)$ for the bound states of an alkali atom with quantum defects $\mu_{n,\ell}$ are thus given by

$$\chi_{n,\ell}(r) = (-1)^{n+\ell+1} \left(\frac{(n^*)^3}{2}\right)^{1/2} K(n^*,\ell)\, \Theta(n^*,\ell;r), \tag{1.18}$$

where we have introduced the effective principal quantum number $n^* = n - \mu_{n,\ell}$.

1.3 Thesis overview

The thesis is structured as follows. We begin in Chapter 2 with a study of radiative cascades from Rydberg states. Motivated by a quantitative analysis of the suitability of a truncated level structure commonly used in the study of Rydberg dressing schemes, we use quantum defect theory to compute spontaneous emission rates and branching ratios for radiative cascades from the Rydberg states of rubidium atoms.

In Chapter 3 we study two-body interactions of Rydberg atoms, investigating the possibility of using a pair of Rydberg atoms to form a diatomic molecule with an extremely large internuclear distance. By using quantum defect theory to model the Rydberg wavefunctions, we compute potential energy curves and approximate radiative lifetimes for Rydberg dimer states up to $n = 35$.

In Chapter 4 we investigate mesoscopic crystals of several dozen dipolar atoms held in a harmonic trap. We analyse their structure and melting temperature, and describe two possible dressing schemes by which an electric dipole moment may be induced in a neutral alkali atom by admixing a small component of a Rydberg state into the ground state. We extend the radiative cascade analysis of Chapter

2 to compute the rate of heating due to spontaneous emission in one such dressing scheme, and discuss the implications of this heating on the stability of mesoscopic crystals of Rydberg-dressed atoms.

In the second portion of this thesis, which comprises Chapters 5 and 6, we present the method of path-sums, a novel method for symbolically evaluating matrix functions that aims to provide a new tool for the simulation of strongly-correlated many-body Rydberg systems. In contrast to commonly-used methods such as DMRG, the method of path-sums can be applied to systems in any number of dimensions.

The method of path-sums is based on two main concepts: firstly, a mapping between matrix multiplication and walks on finite directed graphs, and secondly, a universal result on the structure of such walks. In Chapter 5 we provide a brief review of the important concepts of graph theory, and present the main graph-theoretic result that forms the mathematical basis for the method of path-sums. In Chapter 6 we demonstrate how these results can be used to compute functions of matrices, presenting path-sum expressions for a matrix raised to a complex power, the matrix logarithm, and matrix exponential. We discuss the prospects for applying the method of path-sums to the dynamical simulation of quantum many-body systems.

In Chapter 7 we summarise the main results of this thesis, and discuss future directions in which each of the research topics could be profitably extended.

Chapter 2

Radiative cascades from Rydberg states

Recent theoretical studies of ultra-cold dipolar gases have led to the proposal of schemes to induce strong dipolar interactions between neutral atoms by exploiting the enormous electric dipole moments associated with atomic Rydberg states [73, 74]. By using off-resonant laser light to admix a small component of a Rydberg state $|r\rangle$ into the atomic ground state $|g\rangle$, a non-zero time-averaged electric dipole moment can be induced in a ground-state alkali atom.

Due to the finite lifetime of the state $|r\rangle$, such dressing schemes necessarily introduce spontaneous emission into the system: at random intervals, the Rydberg component of the dressed state decays, a photon is emitted, and the atom receives a corresponding momentum kick. A detailed understanding of the consequent atomic heating is likely to be crucial in understanding the limitations of using Rydberg dressing schemes in the context of ultra-cold dipolar gases.

In current treatments, the rate at which spontaneous emission takes place and the heating it produces are typically estimated by assuming that every event leaves the atom back in the ground state $|g\rangle$: that is, the possibility that the atom may pass through one or more intermediate states on its way to the ground state is discounted [74]. This approximation is reasonable for small values of the Rydberg principal quantum number n, but is expected to progressively worsen as n is increased. In this chapter, we quantitatively analyse the validity of this approximation by computing spontaneous emission rates and branching ratios for the decay channels leading out of the Rydberg states of rubidium. We achieve this by using

quantum defect theory to calculate the wavefunctions of the Rydberg electron in states up to $n = 40$, and applying the theory of spontaneous emission of hydrogenic atoms. For completeness, we present a summary of the theory of spontaneous emission of hydrogenic atoms in Appendix B.

This work was motivated by discussions with Andrew Daley, Andrea Micheli, and Peter Zoller at the University of Innsbruck. All calculations and analysis contained in this chapter are the work of the present author.

2.1 Branching ratios and cascade paths

The probability per unit time for a hydrogenic atom in a state with quantum numbers (n_i, ℓ_i, m_i) and energy ε_i to emit a photon and decay into the manifold of states with quantum numbers (n_i, ℓ_f) and energy ε_f, where $\ell_f = \ell_i \pm 1$, is given in atomic units by [68]

$$\Gamma^{n_f,\ell_f}_{n_i,\ell_i,m_i} = \frac{4}{3}\alpha^3\big(\varepsilon_i - \varepsilon_f\big)^3 \left[\mathcal{R}^{n_f,\ell_f}_{n_i,\ell_i}\right]^2 \frac{\max(\ell_i,\ell_f)}{(2\ell_i+1)}, \tag{2.1}$$

where $\alpha \approx 1/137.036$ is the fine-structure constant and $\mathcal{R}^{n_f,\ell_f}_{n_i,\ell_i}$ is given by

$$\mathcal{R}^{n_f,\ell_f}_{n_i,\ell_i} = \int_0^\infty \mathrm{d}r\, \chi^*_{\varepsilon_f,\ell_f}(r)\, r\, \chi_{\varepsilon_i,\ell_i}(r), \tag{2.2}$$

where $\chi_{\varepsilon,\ell}(r)$ is the reduced radial wavefunction for the state with energy ε and angular momentum quantum number ℓ (see Eq. (1.18)). The total rate of spontaneous emission from the state (n_i, ℓ_i, m_i) is thus

$$\Gamma_{\mathrm{tot}} = \sum_{\substack{\varepsilon_f < \varepsilon_i \\ \ell_f = \ell_i \pm 1}} \Gamma^{n_f,\ell_f}_{n_i,\ell_i,m_i} \tag{2.3}$$

and the radiative lifetime of the state is $\Gamma^{-1}_{\mathrm{tot}}$.

For a given atomic state (n_i, ℓ_i), we define the branching ratios $p^{n_f,\ell_f}_{n_i,\ell_i}$ for states with quantum numbers (n_f, ℓ_f) such that $\varepsilon_f < \varepsilon_i$ and $\ell_f = \ell_i \pm 1$ by

$$p^{n_f,\ell_f}_{n_i,\ell_i} = \frac{\Gamma^{n_f,\ell_f}_{n_i,\ell_i,m_i}}{\Gamma_{\mathrm{tot}}}. \tag{2.4}$$

These quantities yield information about the most likely route for a highly excited alkali atom to follow as it decays to the ground $n = 5$, $\ell = 0$ state, and therefore

provide quantitative information on the validity of the assumption that every decay event leads directly to the ground state. The branching ratios $p_{n_i,\ell_i}^{n_f,\ell_f}$ for $n_i = (19, 29, 37)$ are illustrated in Figure 2.1.

By viewing the branching ratios in Figure 2.1 as a function of n_f for a fixed initial state (n_i, ℓ_i), it is clear that the decays are strongly biased towards states with small values of n_f: approximately $70 - 90\%$ of emission events leave the atom in a state with $n_f \leq 10$, while 40 – 50% of events lead directly to a state with $n_f = 5$. This behaviour is evident even for large values of n_i, since even though the radial overlap integral $\mathcal{R}_{n_i,\ell_i}^{n_f,\ell_f}$ for fixed n_f becomes smaller as n_i increases, this is more than compensated for by the increasing energy difference $\varepsilon_i - \varepsilon_f$, upon which the branching ratio has a cubic dependence.

To elucidate the structure of the branching ratios $p_{n_i,\ell_i}^{n_f,\ell_f}$ as a function of ℓ_i, in Figure 2.2 we compare the quantities

$$\sum_{\varepsilon_f<\varepsilon_i} p_{n_i,\ell_i}^{n_f,\ell_i-1} \qquad \text{and} \qquad \sum_{\varepsilon_f<\varepsilon_i} p_{n_i,\ell_i}^{n_f,\ell_i+1} \tag{2.5}$$

for $5 \leq n_i \leq 37$ and $\ell_i = 1, 2, 3$. By viewing these plots as a function of ℓ_i for fixed n_i, we see that the ratio of 'upward' ($\ell_f = \ell_i + 1$) to 'downward' ($\ell_f = \ell_i - 1$) transitions drops rapidly with increasing ℓ_i, becoming small ($\ll 5\%$) even for $\ell_i = 3$. A rubidium atom decaying from a Rydberg state to the ground state $(5, 0)$ thus only rarely visits states with $\ell \geq 3$ along the way.

2.2 Emission spectra and cascade lengths

A rubidium atom in a Rydberg state may decay to the ground state by any of a large number of possible routes. Each route corresponds to a sequence of atomic decay events, which take the atom from (n_i, ℓ_i) to the ground state $(5, 0)$. In the course of this radiative cascade, the atom emits a sequence of photons with wavevectors $\mathbf{k}_1, \mathbf{k}_2, \ldots, \mathbf{k}_m$, where m is the cascade length. As a consequence of the selection rules associated with electric dipole radiation, m is odd if the initial state has odd parity ($\ell_i = 1, 3, \ldots$), or even if the initial state has even parity ($\ell_i = 0, 2, 4, \ldots$). Further, the conservation of energy means that the photon wavevectors must satisfy $\hbar\left(|\mathbf{k}_1| + |\mathbf{k}_2| + \ldots + |\mathbf{k}_m|\right) = \varepsilon_f - \varepsilon_i$, where ε_i is the energy of the initial state (n_i, ℓ_i), and ε_f is the energy of the atomic ground state. Beyond these two simple observations, a quantitative study of the dynamics of a cascading atom requires detailed knowledge of the branching ratios $p_{n_i,\ell_i}^{n_f,\ell_f}$. Specifically, the probability that an atom

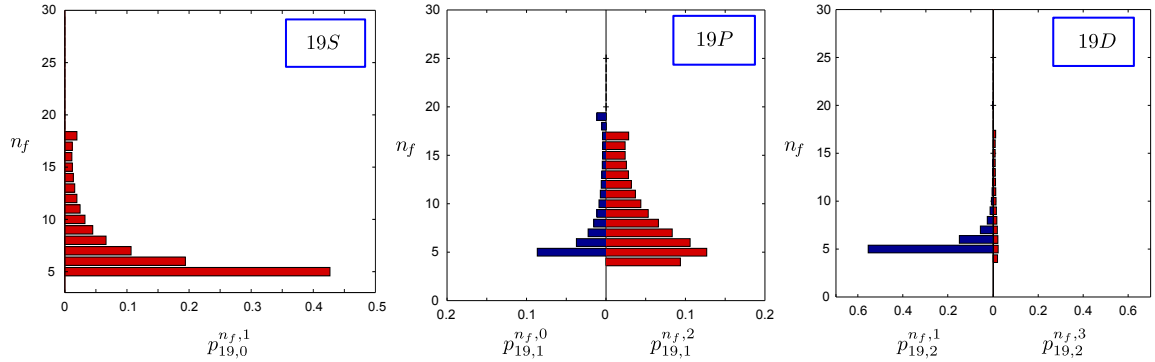

(a) Branching ratios for decay from the $n_i = 19, \ell_i = 0, 1, 2$ states of rubidium to the $(n_f, \ell_i - 1)$ manifold (blue bars) and the $(n_f, \ell_i + 1)$ manifold (red bars).

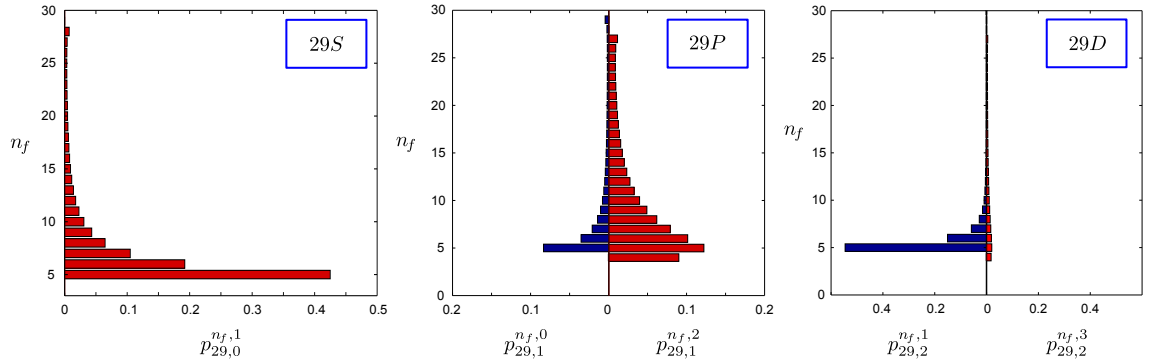

(b) Branching ratios for decay from the $n_i = 29, \ell_i = 0, 1, 2$ states of rubidium to the $(n_f, \ell_i - 1)$ manifold (blue bars) and the $(n_f, \ell_i + 1)$ manifold (red bars).

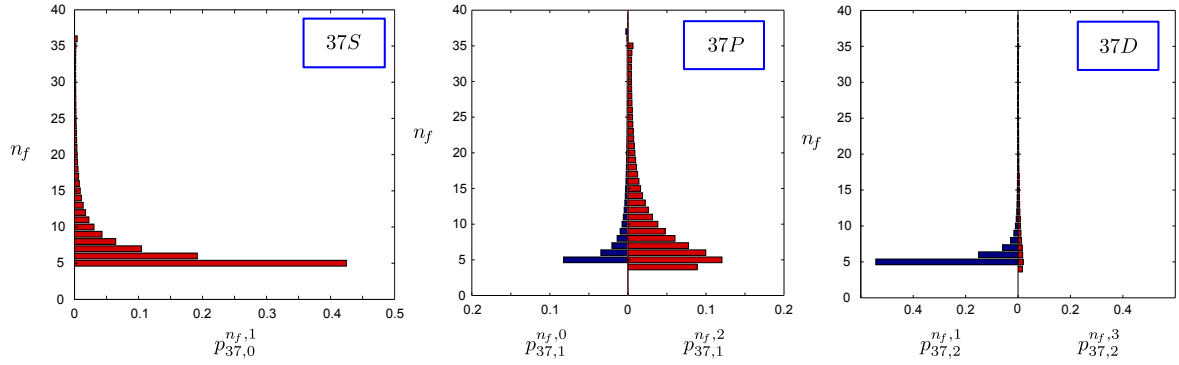

(c) Branching ratios for decay from the $n = 37, \ell_i = 0, 1, 2$ states of rubidium to the $(n_f, \ell_i - 1)$ manifold (blue bars) and the $(n_f, \ell_i + 1)$ manifold (red bars).

Figure 2.1: Branching ratios $p^{n_f,\ell_f}_{n_i,\ell_i}$ for rubidium states with $n_i = 19, 29, 37$ and $1 \leq \ell_i \leq 3$. The branching ratios are significantly biased towards small values of n_f.

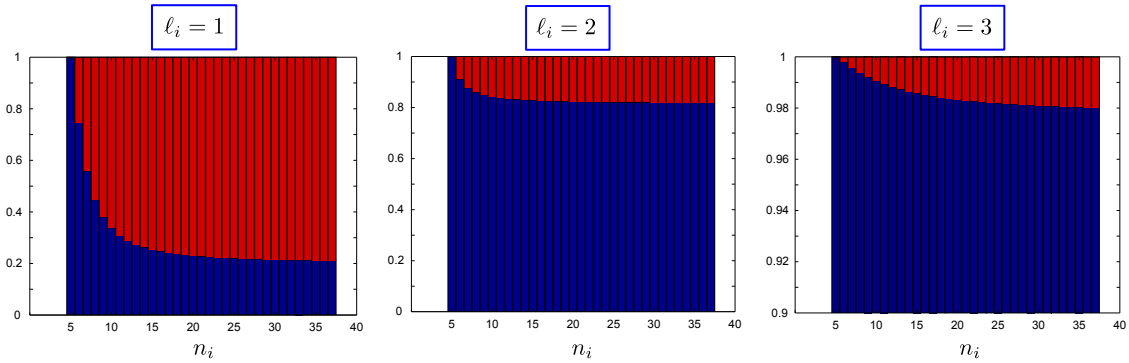

(a) Decays from $(n_i, 1)$ states. (b) Decays from $(n_i, 2)$ states. (c) Decays from $(n_i, 3)$ states.

Figure 2.2: A comparison of the relative probabilities for a Rubidium atom in an (n_i, ℓ_i) state to decay to a lower state with $\ell_f = \ell_i - 1$ (blue) or $\ell_f = \ell + 1$ (red), plotted for $5 \leq n_i \leq 37$. The quantities on the y-axis are the left-hand side (blue) and right-hand side (red) of Eq. (2.5). Note the difference in y-axis scale for the plot with $\ell_i = 3$.

initialized in (n_i, ℓ_i) passes through the states $(n_2, \ell_2), (n_3, \ell_3), \ldots, (n_{m-1}, \ell_{m-1})$ en route to the ground state is

$$p_{n_i,\ell_i}^{n_2,\ell_2} \, p_{n_2,\ell_2}^{n_3,\ell_3} \cdots p_{n_m,\ell_m}^{5,0}. \tag{2.6}$$

One convenient method of obtaining radiative cascades statistics is to use a simple Monte Carlo procedure to simulate the cascade process. The Monte Carlo procedure for simulating a radiative cascade is as follows:

(i) Initialize the atom in the state (n_i, ℓ_i).

(ii) Label the decay channels leading out of the current state according to some (freely chosen) ordering convention. For convenience, we denote the final state of the j^{th} decay channel by (n_j, ℓ_j).

(iii) Generate a random variate r from the uniform distribution on $[0, 1]$.

(iv) Identify the index x that satisfies

$$\sum_{j=1}^{x-1} p^{(j)} < r \leq \sum_{j=1}^{x} p^{(j)} \tag{2.7}$$

where $p^{(j)}$ is the branching ratio associated with decay channel j.

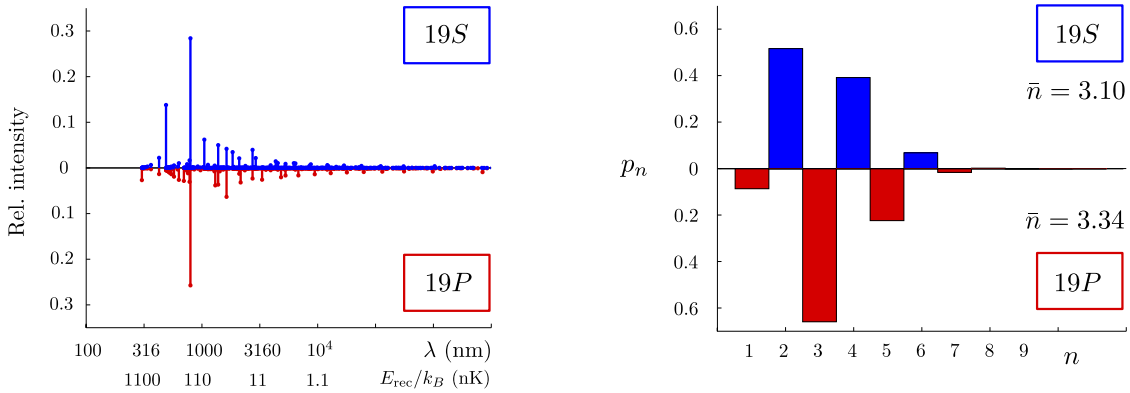

(a) Emission spectrum (left) and distribution of radiative cascade lengths (right) for cascades starting from the (19,0) and (19,1) states of rubidium.

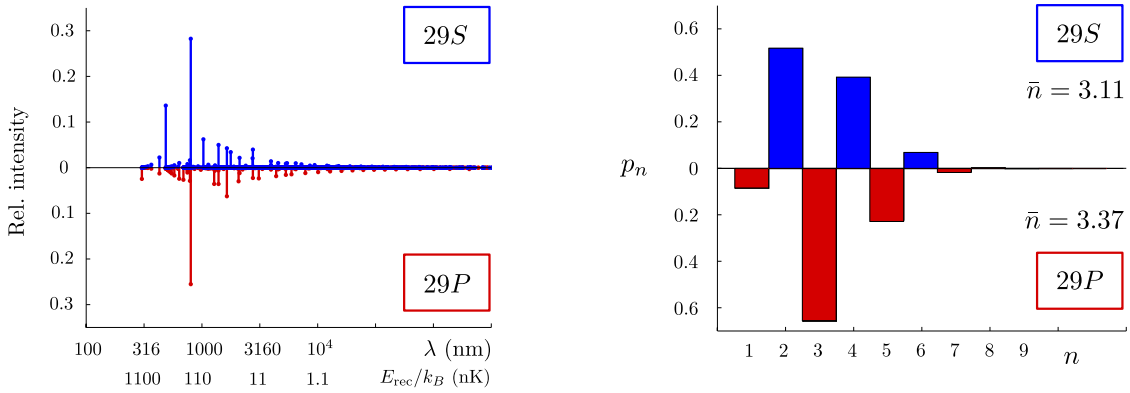

(b) Emission spectrum (left) and distribution of radiative cascade lengths (right) for cascades starting from the (29,0) and (29,1) states of rubidium.

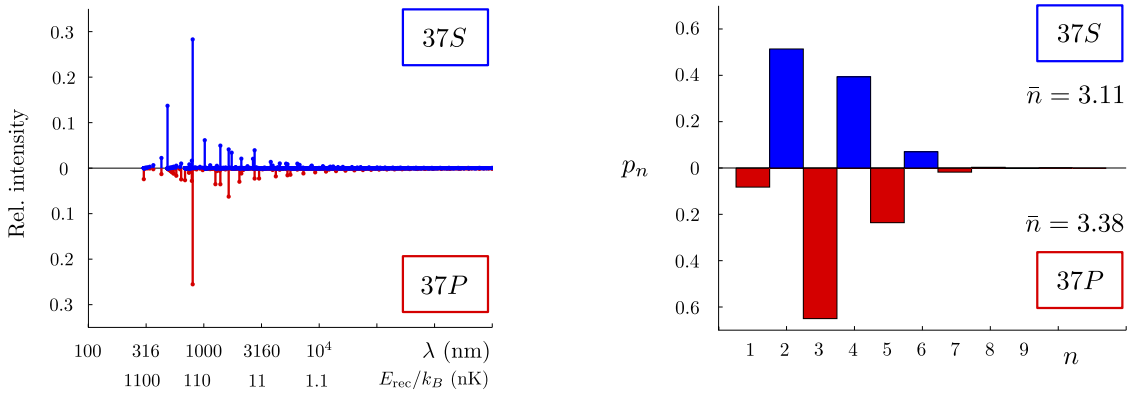

(c) Emission spectrum (left) and distribution of radiative cascade lengths (right) for cascades starting from the (37,0) and (37,1) states of rubidium.

Figure 2.3: The spectrum of the emitted radiation (left) and the distribution of the number of photons emitted (right) during the radiative cascade of a rubidium atom from a Rydberg state to the ground (5,0) state. This data reflects the results of 1×10^5 simulated cascades from each (n_i, ℓ_i) to the ground state.

(v) Transfer the atom to (n_x, ℓ_x), the final state of decay channel x. If this is the ground state $(5, 0)$, then stop; otherwise, return to step (ii).

Figure 2.3 summarises the results of 1×10^5 such simulations. The left-hand plots show the spectrum of the photons emitted during a radiative cascade from the (n_i, ℓ_i) state, for $n_i = 19, 29, 37$ and $\ell_i = 0, 1$ (spectra for higher values of ℓ_i do not differ significantly from those for $\ell_i = 0, 1$, and are not included here). The plots on the right show the probability distribution for the length of the radiative cascade (i.e. the number of photons emitted in returning to the ground state) for the same initial state parameters. These probability distributions also change only negligibly with increasing n_i.

These plots make several points apparent. From the distributions of cascade lengths, it is clear that the most likely cascade length from an $\ell = 1$ state is 3. Perhaps surprisingly, the direct single-photon decay to the ground state occurs only rarely, in somewhat less than 10% of cases. This behaviour is a consequence of the branching ratios, as seen in Figure 2.2: although for fixed n_i the quantities $p_{n_i,\ell_i}^{n_f,\ell_f}$ are biased towards low values of n_f, an $\ell_i = 1$ state is much more likely to decay upwards to an $\ell = 2$ state than downwards to an $\ell = 0$ state. Specifically, the most likely final states are $(n, 2)$ with $n \lesssim 8$. This is likely to be followed by a decay to an $(n', 1)$ state with $n' \leq n$ (often $n' = 5$ or 6), followed by a rapid decay to the $(5, 0)$ state.

Cascades that start from an $\ell = 0$ state follow a similar pattern: the first emission is highly likely to leave the atom in a state $(n', 1)$ with $n' \lesssim 10$. Depending on the value of n', the atom proceeds to the ground state either by a direct decay (if n' is small) or by a 3-photon cascade similar to that described above (if n' is larger).

The emission spectra on the left-hand side of Figure 2.3 provide evidence for this interpretation. The dominant peak appearing in each spectrum corresponds to the $5P \rightarrow 5S$ transition. The relative height of this peak indicates that 25–30% of all radiative cascades pass through this decay channel as the final step in their route to the ground state. Further, this fraction is essentially constant for all values of n_i and ℓ_i studied here, evidencing the central involvement of this transition in radiative cascades from Rydberg states of all energies. Evidence for other $nP \rightarrow 5S$ transitions with $n \lesssim 10$, in particular the $6P \rightarrow 5S$ transition, can be seen at shorter wavelengths.

2.2.1 On the validity of a restricted level scheme

As noted in the introduction to this section, it is a common approximation in the study of systems of Rydberg atoms to assume that all spontaneous emission events lead directly to the ground state. The branching ratios and radiative cascade results presented in Figures 2.1 – 2.3 suggest that this approximation is not particularly accurate: taking the example of $n = 29$, we see from Figure 2.1 that somewhat less than 50% of decay events lead to a final state with $n = 5$. This implies that any physical results that depend on the details of the spontaneous emission processes that occur within Rydberg dressing schemes should be computed using a more complete treatment of the atomic level structure.

2.3 Summary

It is a common approximation within proposals for the Rydberg dressing of ground-state atoms to assume that every spontaneous emission event from a Rydberg state leads directly back to the ground state. In order to quantitatively investigate the validity of this approximation, we calculated the spontaneous emission rates and branching ratios for the Rydberg states of rubidium up to $n = 40$, using quantum defect theory to calculate the Rydberg wavefunctions. Through simulations of spontaneous emission cascades, we found that the most common path to the ground $5S$ state taken by a rubidium atom in a highly excited S or P state consists of either a 2- or 4-photon cascade (from an S state) or a 3-photon cascade (from a P state). This suggests that a full treatment of the atomic level structure is essential in cases where a quantitatively correct treatment of spontaneous emission behaviour from Rydberg states is required.

Chapter 3

Ultra-large Rydberg dimers in optical lattices

In this chapter we investigate the possibility of using Rydberg atoms to form cold diatomic molecules with extremely large internuclear distances: so-called macro-dimers.

The work presented in this chapter was carried out in collaboration with Benoît Vaucher, and was published in 2008 in *Physical Review A* [75]. The primary contribution of the present author to this work was in carrying out the radiative lifetime calculations of §3.2.4. The molecular potential calculations in §3.2.2 were carried out by Benoît Vaucher, with the present author acting as a discussion partner.

3.1 Introduction and motivation

The preparation, manipulation, and characterisation of collections of ultra-cold molecules is currently a very active field of study within cold matter physics [76, 77], motivated by aims that range from new techniques for probing the time-variation of fundamental constants [78] to the formation of strongly-interacting dipolar gases for quantum simulation purposes [79, 80] to proposals for the detection of dark matter [81]. Central among the attractive properties of molecules for such applications are their complex energy level structures and large number of degrees of freedom, which provide for a much wider range of possibilities for the control and manipulation of molecules as compared with single atoms.

The task of cooling molecules to the exceptionally low temperatures routinely seen in atomic gases is made significantly more challenging by the failure of the laser cooling techniques which have seen such spectacular success in atomic systems. The reason for this is simple: the complex rovibrational energy level structure behind much of the rich physics of molecules is at odds with the existence of a simple closed electronic transition that can be used to scatter many thousands of photons during the cooling process. While research towards the laser cooling of molecules continues [82, 83, 84], the difficulty of this process has motivated the development of range of alternative cooling techniques, including Stark deceleration and buffer gas cooling [85, 86, 87]. However, while these methods are more widely applicable, the lowest temperatures they provide access to are in the range of a few milliKelvin – several orders of magnitude higher than the temperatures routinely achieved in atomic gases. It is therefore an attractive proposition to form molecules from pre-cooled atoms, circumventing the difficult task of cooling the molecules themselves [88].

One topic that has recently attracted significant theoretical and experimental interest in this area is the creation and characterisation of molecules formed by Rydberg atoms. As noted in Chapter 1, two classes of such molecules have recently been predicted and observed: firstly, dimers consisting of one Rydberg atom interacting with a ground-state atom [46, 47, 48, 49]; and secondly, 'macrodimer' molecules formed by a pair of Rydberg atoms stabilised by purely long-range interactions [50, 51, 52, 53].

In this chapter we investigate the possibility of creating ultralarge dimers by the photoassociation of a pair of Rydberg atoms whose nuclear positions are fixed by an optical lattice. By using quantum defect theory to calculate approximate electronic Rydberg wavefunctions, we study the feasibility of creating ultralarge dimers with equilibrium distances of the order of typical lattice spacings and binding energies of the order of 10^3 GHz.

3.2 Molecular potentials of ultra-large Rydberg dimers

In this section we present a method of evaluating the energy of highly excited diatomic molecular states with large internuclear distances. We utilise an efficient symbolic method for computing one- and two-center molecular integrals over

electronic wavefunctions with large principal quantum numbers, and calculate the depth and equilibrium position of molecular potentials for values of the principal quantum n up to $n = 35$. Further, we estimate the radiative lifetime of these highly excited molecular states, and discuss the likely importance of their decay via autoionisation.

3.2.1 Overview

The appropriate model for the investigation of diatomic molecules depends crucially on the regime of interest. Theoretical treatments to date have focused on the regime of very large internuclear separations, where the overlap between charge distributions is negligible and the atomic orbitals are only minimally distorted by their mutual interaction [89, 50]. In this regime the interatomic potential can be written as a multipole expansion in powers of the inverse of the internuclear distance R. However, this expansion is not suitable for small internuclear distances where the atomic orbitals begin to interact directly with one another and effects such as the exchange interaction must be taken into account. A commonly used estimate of the internuclear separation at which this crossover from 'physical' to 'chemical' behaviour occurs is the Le Roy radius R_{LR} [90], defined as

$$R_{\mathrm{LR}} = 2\left[\langle r_1^2\rangle^{1/2} + \langle r_2^2\rangle^{1/2}\right], \tag{3.1}$$

where r_1 and r_2 are the coordinates of the two valence electrons. Figure 3.1 provides a schematic illustration of the situation for different values of the interatomic separation R as compared with the Le Roy radius R_{LR}.

Although a number of well-established quantum chemistry techniques for calculating molecular properties within the Le Roy radius exist (e.g. molecular orbital-linear combination of atomic orbitals, or MO-LCAO, methods [91]), these approaches become prohibitively expensive when applied to Rydberg molecules due to the size of the basis set needed to represent the spatially diffuse Rydberg orbitals. This provides motivation for an approach to the problem using molecular integrals.

3.2.2 Model

We consider an optical lattice consisting of an array of double-well potentials, which are assumed to be separated by sufficiently high potential barriers that each double

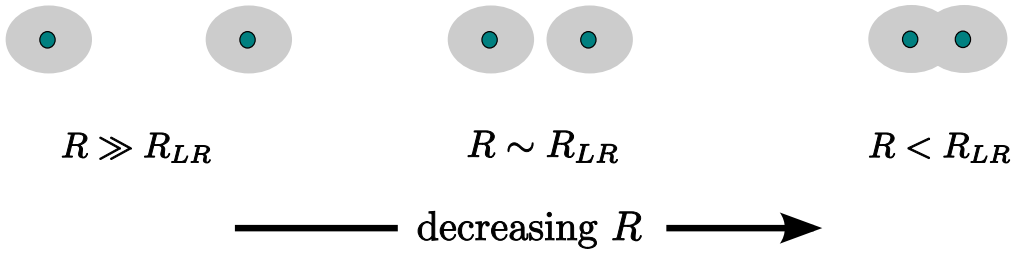

Figure 3.1: A schematic illustration of the different regimes for molecular potential calculations. When the internuclear distance R is much larger than the Le Roy radius R_{LR} (left), the interatomic potential is well approximated by a multipole expansion: $V(R) \approx \sum_{n\geq 1} C_n R^{-n}$. When R is smaller than R_{LR} (right), the atomic orbitals overlap significantly, and quantum chemistry methods such as MO-LCAO are commonly used. The transitional regime where R is comparable to R_{LR} (centre) remains computationally challenging, especially when highly excited Rydberg orbitals are considered.

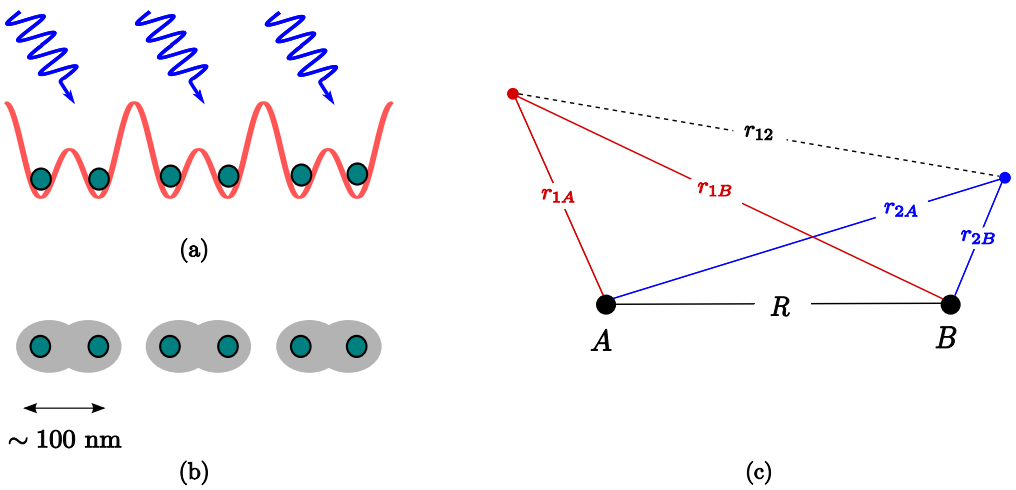

Figure 3.2: By applying a short laser pulse to pairs of ultracold ^{87}Rb atoms held in an optical superlattice of double-well potentials (a), the atoms are promoted to highly excited Rydberg states, such that the electronic charge distribution of atoms in neighbouring wells overlap. We aim to study the basic properties of the resultant diatomic molecules (b), which have extremely large internuclear separations. (c) The coordinate system used in this chapter, showing the positions of the atomic cores (labelled A and B) and the excited Rydberg electrons (red and blue dots).

well may be considered independently of its neighbours (see Figure 3.2(a)). This lattice arrangement can be created by a retro-reflected laser beam with careful phase control [92]. We assume that each double well is occupied by a pair of ^{87}Rb atoms, with one atom localised in each half of the double well. By applying a brief laser pulse to the system, the valence electron of each atom can be promoted to a highly excited Rydberg state. If the spatial extent of the Rydberg orbital is comparable with the inter-well spacing, the electronic charge distributions of the two atoms within a double well overlap, and under certain conditions a stable molecular state is formed. We aim to study the basic properties of these molecules and explore whether they may be produced in an optical lattice with experimentally realistic parameters.

Since the temperature of the system is very low, the velocity of the electrons - even in highly excited states - is much greater than that of the trapped ions, and the electrons respond almost instantaneously to displacements of the ions [50]. Consequently, we will calculate molecular potentials in the Born-Oppenheimer (BO) approximation [91, 93].

Neglecting interactions between atoms belonging to different double wells, the energy levels of a homonuclear molecule formed by the atoms in a double well are given by the eigenvalues of the Hamiltonian

$$H(R) = -\frac{\hbar^2}{2m_e}\left(\nabla^2_{\mathbf{r}_1} + \nabla^2_{\mathbf{r}_2}\right) + \frac{e^2}{4\pi\varepsilon_0}\left(\frac{1}{R} + \frac{1}{r_{12}} - \frac{1}{r_{1A}} - \frac{1}{r_{1B}} - \frac{1}{r_{2A}} - \frac{1}{r_{2B}}\right) \quad (3.2)$$

where $\mathbf{r}_i$ for $i = 1, 2$ is the position of the i^{th} electron; $\mathbf{r}_{i\xi}$ ($\xi = A, B$) is the distance between the i^{th} electron and the nucleus of atom ξ; r_{12} is the distance between the two electrons; and R is the distance between the nuclei. Within the Born-Oppenheimer approximation, R is treated as a classical variable upon which the eigenvalues and eigenfunctions of the Hamiltonian depend parametrically.

Following a similar approach to that of [94, 95], we approximate the molecular energy at a particular internuclear distance R by diagonalising the Hamiltonian of Eq. (3.2), using as a basis the two-electron states defined by

$$\Psi^{\pm}_{\mathbf{q},\mathbf{q}'}(\mathbf{r}_1, \mathbf{r}_2) = N^{\pm}_{\mathbf{q},\mathbf{q}'}\left[\mathrm{A}_{\mathbf{q}}(\mathbf{r}_1)\mathrm{B}_{\mathbf{q}'}(\mathbf{r}_2) \pm \mathrm{A}_{\mathbf{q}}(\mathbf{r}_2)\mathrm{B}_{\mathbf{q}'}(\mathbf{r}_1)\right], \quad (3.3)$$

where $\mathrm{A}_{\mathbf{q}}(\mathbf{r})$ ($\mathrm{B}_{\mathbf{q}}(\mathbf{r}_1)$) is a hydrogenic single-electron wavefunction with quantum numbers $\mathbf{q} = (n, \ell, m)$ centred on nucleus A (B), and the normalisation factor $N^{\pm}_{\mathbf{q},\mathbf{q}'}$

is equal to

$$N^{\pm}_{\mathbf{q},\mathbf{q}'} = \left[2(1 \pm |S_{\mathbf{q},\mathbf{q}'}|^2)\right]^{-1/2}, \tag{3.4}$$

where $S_{\mathbf{q},\mathbf{q}'}$ is the overlap integral defined by [91]

$$S_{\mathbf{q},\mathbf{q}'} = \int \mathrm{d}\mathbf{r}\, \mathrm{A}^*_{\mathbf{q}}(\mathbf{r})\, \mathrm{B}_{\mathbf{q}'}(\mathbf{r}). \tag{3.5}$$

In keeping with fermionic exchange statistics, the basis functions that are symmetric or antisymmetric in the spatial coordinates $\mathbf{r}_1$ and $\mathbf{r}_2$ are associated with an antisymmetric (singlet) or symmetric (triplet) spin function, respectively.

Since the rubidium atoms considered here have only a single valence electron, the atomic wavefunctions $\xi_{\mathbf{q}}(\mathbf{r})$ ($\xi = \mathrm{A}, \mathrm{B}$) are well approximated by quantum defect theory. Further, the interatomic interactions we are interested in are due to the interaction of the atomic wavefunctions at distances far from each of the nuclei. In view of this, we define $\xi_{\mathbf{q}}(\mathbf{r})$ to be the (unnormalized) function

$$\xi_{\mathbf{q}}(\mathbf{r}) = P_\ell(\cos\theta_\xi)\, \frac{\mathrm{e}^{\mathrm{i}m\phi}}{a_0^{3/2}} \left(\frac{2\rho_\xi}{n^*}\right)^{n^*} \mathrm{e}^{-\rho_\xi/n^*} \sum_{k=0}^{k_{\max}} b_k\, \rho_\xi^{-(k+1)}, \tag{3.6}$$

where $\rho_\xi = r_\xi/a_0$ is a dimensionless radial coordinate, with $r_\xi = |\mathbf{r} - \mathbf{r}_\xi|$ the radial distance from atom ξ; θ_ξ is the angle between the vector $\mathbf{r}_\xi$ and the internuclear axis; ϕ is the azimuthal angle; $P_\ell(x)$ is a Legendre polynomial; and $n^* = n - \delta_{n,\ell}$ with $\delta_{n,\ell}$ the quantum defect for the (n, ℓ, m) state is the effective principal quantum number. The coefficients $\{b_k\}$ are defined recursively, with $b_0 = 1$ and

$$\mathrm{b}_k = \mathrm{b}_{k-1} \left(\frac{n^*}{2k}\right) \left[\ell(\ell+1) - (n^*-k)(n^*-k+1)\right], \tag{3.7}$$

while the upper index of the summation $k_{\max}$ is an integer satisfying $n^* - \ell - 1 \leq k_{\max} < n^* - \ell$ [96, 97].

The wavefunction of Eq. (3.6) is an asymptotic form of the hydrogenic quantum defect wavefunction with quantum numbers (n^*, ℓ, m). For $\delta_\ell = 0$ it reproduces the hydrogen wavefunction, while for $\delta_\ell \neq 0$ it provides an accurate description of a Rydberg state of an alkali atom in the mid- and long-range. It differs from the exact quantum defect wavefunction only at short distances from the atomic cores, which is of little consequence to us since the region of interest in which the electron wavefunctions overlap and interact is far from the atomic nuclei.

For $n \gtrsim 20$ and $\mathbf{q} = \mathbf{q}'$, the overlap $S_{\mathbf{q},\mathbf{q}'}$ between the charge-density distributions of a pair of atoms separated by a distance smaller than the Le Roy radius is typically of the order of $S_{\mathbf{q},\mathbf{q}'} \simeq 10^{-1} - 10^{-2}$. This suggests that the overlap between atomic wavefunctions is not negligible in this regime, and the approximation of the Coulomb potential by a multipole expansion commonly used to study interactions at larger internuclear separations [18, 19] is not suitable. This is because the multipole expansion diverges significantly from the true Coulomb potential even in the presence of small charge-density overlap, so that the results obtained using this approach below the Le Roy radius are not trustworthy [50, 98].

Consequently, we estimate the energy of the dimer by evaluating the expectation value of the Hamiltonian Eq. (3.2) in the basis states defined by Eq. (3.3). The molecular energy at an internuclear separation R is given by

$$E^{\mathrm{mol}}_{\mathbf{q},\mathbf{q}'}(R) = \iint \mathrm{d}\mathbf{r}_1 \mathrm{d}\mathbf{r}_2 \, \left[\Psi^{\pm}_{\mathbf{q},\mathbf{q}'}(\mathbf{r}_1, \mathbf{r}_2)\right]^* H(R) \, \Psi^{\pm}_{\mathbf{q},\mathbf{q}'}(\mathbf{r}_1, \mathbf{r}_2). \tag{3.8}$$

This task requires the evaluation of a number of integrals over atomic orbitals. These integrals fall into two classes. The first group is the set of one-centre integrals, which comprises the overlap integral $S_{\mathbf{q},\mathbf{q}'}$, the Coulomb integral

$$J_{\mathbf{q},\mathbf{q}'} = \frac{e^2}{4\pi\varepsilon_0} \int \mathrm{d}\mathbf{r} \, \mathrm{B}^*_{\mathbf{q}}(\mathbf{r}) \frac{1}{r_A} \mathrm{B}_{\mathbf{q}'}(\mathbf{r}) = \frac{e^2}{4\pi\varepsilon_0} \int \mathrm{d}\mathbf{r} \, \mathrm{A}^*_{\mathbf{q}}(\mathbf{r}) \frac{1}{r_B} \mathrm{A}_{\mathbf{q}'}(\mathbf{r}) \tag{3.9a}$$

and the charge-overlap integral

$$K^{\xi}_{\mathbf{q},\mathbf{q}'} = \frac{e^2}{4\pi\varepsilon_0} \int \mathrm{d}\mathbf{r} \, \mathrm{A}^*_{\mathbf{q}}(\mathbf{r}) \frac{1}{r_\xi} \mathrm{B}_{\mathbf{q}'}(\mathbf{r}). \tag{3.9b}$$

The second group consists of the two-centre integrals, of which there are four:

$$U^{\mathbf{q},\mathbf{q}'}_{\mathbf{p},\mathbf{p}'} = [\mathrm{A}_{\mathbf{q}}\mathrm{A}_{\mathbf{q}'}|\mathrm{A}_{\mathbf{p}}\mathrm{A}_{\mathbf{p}'}]\,, \qquad W^{\mathbf{q},\mathbf{q}'}_{\mathbf{p},\mathbf{p}'} = [\mathrm{A}_{\mathbf{q}}\mathrm{B}_{\mathbf{q}'}|\mathrm{A}_{\mathbf{p}}\mathrm{B}_{\mathbf{p}'}]\,, \tag{3.10a}$$

$$V^{\mathbf{q},\mathbf{q}'}_{\mathbf{p},\mathbf{p}'} = [\mathrm{A}_{\mathbf{q}}\mathrm{A}_{\mathbf{q}'}|\mathrm{B}_{\mathbf{p}}\mathrm{B}_{\mathbf{p}'}]\,, \qquad X^{\mathbf{q},\mathbf{q}'}_{\mathbf{p},\mathbf{p}'} = [\mathrm{A}_{\mathbf{q}}\mathrm{A}_{\mathbf{q}'}|\mathrm{A}_{\mathbf{p}}\mathrm{B}_{\mathbf{p}'}]\,, \tag{3.10b}$$

where

$$[\alpha\beta|\gamma\nu] = \frac{e^2}{4\pi\varepsilon_0} \iint \mathrm{d}\mathbf{r}_1 \, \mathrm{d}\mathbf{r}_2 \, \alpha^*(\mathbf{r}_1)\beta(\mathbf{r}_2)\frac{1}{r_{12}}\gamma^*(\mathbf{r}_2)\nu(\mathbf{r})2). \tag{3.11}$$

Evaluating the one- or two-centre molecular integrals directly for large values of n runs into problems with slow convergence and the accumulation of numerical errors, a well-known phenomenon known in the field as numerical erosion [99, 100].

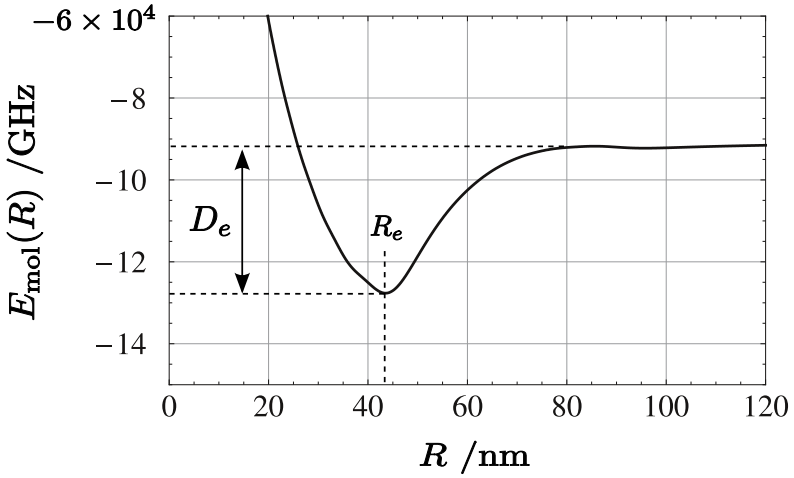

Figure 3.3: The calculated molecular potential curve connecting to the atomic $25p_z + 25p_z$ state, showing the depth D_e of the predicted potential well and the associated equilibrium internuclear distance R_e.

In order to evaluate these molecular integrals, we follow an approach suggested by Barnett [100, 101], and use a computer algebra based method to generate analytical formulas for the integrals in Eqs. (3.9) and (3.10). The full details of this approach can be found in our 2008 publication [75].

Even with the use of exact symbolic calculations, evaluating the molecular integrals for large values of n is computationally challenging. In order to make the calculations tractable for large n, we restrict the value of the projection of the electronic angular momentum along the internuclear axis to $m = 0$. This restricts us to studying only those molecular states with symmetries ${}^1\Sigma_g^+$ and ${}^3\Sigma_u^+$, which are associated with the $\Psi^+_{\mathbf{q},\mathbf{q}'}$ and $\Psi^-_{\mathbf{q},\mathbf{q}'}$ basis states respectively. By applying this restriction, we were able to compute molecular integrals involving wavefunctions with principal quantum numbers up to $n = 35$.

3.2.3 Results

Since we envisage producing the Rydberg dimers by applying a laser pulse to a system of ground-state atoms, we are primarily interested in the molecular states that are most strongly coupled to ground-state atoms by the dipole transition operator: namely, those of ${}^3\Sigma_u^+$ symmetry with a high p-character. We therefore restrict our analysis to these states. However for values of $n \gtrsim 10$, the molecular states of ${}^3\Sigma_u^+$ and ${}^1\Sigma_g^+$ symmetry become quasidegenerate [19, 50], and so the results presented here apply to molecular states of either of these symmetries.

By using the Heitler-London approach, we calculated the molecular potentials

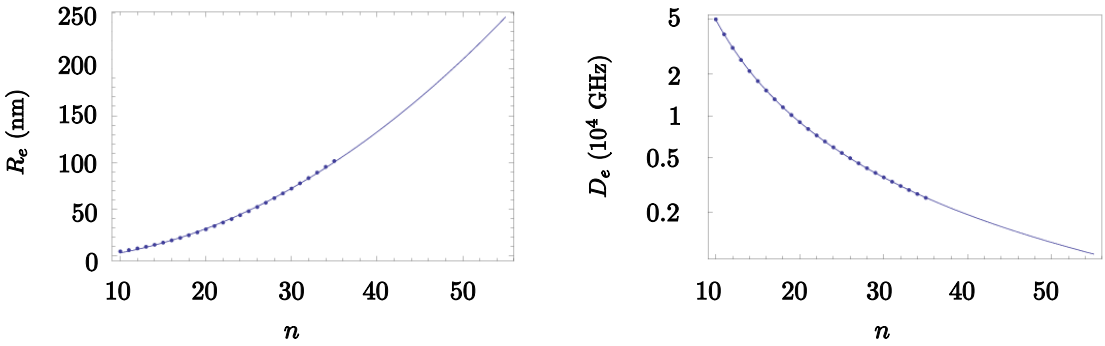

Figure 3.4: Equilibrium distance R_e (left) and potential well depth D_e (right) of the $np + np$ molecular potential curves of rubidium for $10 \leq n \leq 35$ computed using the Heitler-London method. The dots denote the values calculated numerically, while the curves represent the fitted functions mentioned in the text.

resulting from the interaction of np_z orbitals on the two atoms for values of the principal quantum number up to $n = 35$. We used these potential curves to estimate the equilibrium distance R_e and potential well depths $D_e = E_{\rm mol}(\infty) - E_{\rm mol}(R_e)$ of $np + np$ molecular potentials of ${}^3\Sigma_u^+$ symmetry. Figure 3.3 shows one example of a calculated molecular potential curve.

We then used these potential curves to extract the scaling behaviour of R_e and D_e as a function of n, the principal quantum number of the atomic Rydberg orbitals. These results are summarised in Figure 3.4. We find that the equilibrium distance of these potentials is well fitted by the formula

$$R_e \simeq (1.628n^2 - 100.25)\, a_0 \tag{3.12}$$

which is smaller than the Le Roy radius by a factor of approximately 4 for all values of n. For larger values of the principal quantum number $n > 35$, the equilibrium distances predicted by our scaling law are comparable to ($\sim 20\%$ smaller than) those found by Boisseau *et al.* in [50], who use the multipole expansion of the Coulomb potential to examine the same molecular potentials below the Le Roy radius.

The depth of the molecular potential for $n = 35$ is $D_e = 2000$ GHz, some three orders of magnitude larger than the potential depth of ultralarge molecules bonded by long-range dipole-dipole interactions studied in [50]. We find that the molecular binding energy decreases exponentially as the principal quantum number increases,

being well approximated by the relation

$$D_e = \exp\left(\alpha_1 + \alpha_2 n^{\beta_2} + \alpha_3 n_3^{\beta_3}\right) \text{GHz}, \tag{3.13}$$

where $(\alpha_1, \alpha_2, \alpha_3) = (-6.53, -24.44, -20.51)$ and $(\beta_2, \beta_3) = (0.14, -223.45)$. Our predicted potential depths differ from those calculated using the multipole expansion by up to an order of magnitude; as Boisseau *et al.* point out in [50], this is most likely a consequence of the inaccuracy of the multipole expansion below the Le Roy radius.

3.2.4 Radiative lifetimes

We have obtained an order-of-magnitude estimate of the lifetime of the photoassociated molecules by assuming for simplicity that the dominant decay mode is radiative dissociation into a pair of ^{87}Rb atoms. We neglect the rotational fine structure of the energy levels and any bound-bound decay channels and consider a transition between a bound state of vibrational quantum number ν' and energy $E_{\nu'}$ to a free continuum state of wavenumber k'' and energy $E_{k''} = \hbar^2 k''^2/(2\mu)$, where $\mu = m_{\text{Rb}}/2$ is the reduced mass of the molecule. The Einstein A coefficient is given by

$$A_{\nu' k''} = \frac{32\pi^3}{3\varepsilon_0 h^5 c^3}\sqrt{\frac{2\mu}{E_{k''}}}(E_{\nu'} - E_{k''})^3 \times \left| \int \left[\psi_{\nu'}^{\text{vib}}(R)\right]^* D(R) \psi_{k''}^{\text{vib}}(R)\, \mathrm{d}R \right|^2 \quad \text{J}^{-1}\,\text{s}^{-1} \tag{3.14}$$

while the radiative lifetime of a single bound vibrational level is given by $\tau_{\nu'} = A_{\nu'}^{-1}$, where

$$A_{\nu'} = \int_0^\infty A_{\nu' k''}\, \mathrm{d}E_{k''}. \tag{3.15}$$

Here $h = 2\pi\hbar$ is the Planck constant, c is the speed of light, $\psi_{\nu'}^{\text{vib}}$ and $\psi_{k''}^{\text{vib}}$ are vibrational wave functions for the discrete and continuum states respectively, and the dipole moment $D(R)$ is given by

$$D(R) = -e \iint \mathrm{d}\mathbf{r}_1 \mathrm{d}\mathbf{r}_2 \left[\Psi^{\pm}_{\mathbf{q}_i, \mathbf{q}_i}\right]^* (z_1 + z_2) \Psi^{\pm}_{\mathbf{q}_f, \mathbf{q}_f} \tag{3.16}$$

where z_1 and z_2 are the z-coordinates of the electrons and $\mathbf{q}_i$ and $\mathbf{q}_f$ denote the quantum numbers of the initial and final states. For large internuclear distances

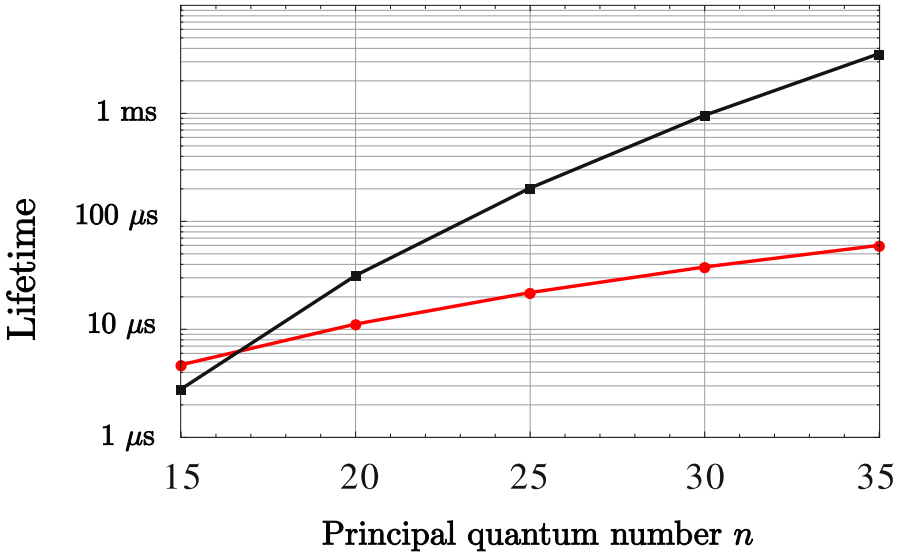

Figure 3.5: Radiative lifetimes for the $\nu' = 0$ vibrational level in molecular excited states with principal quantum numbers $n = 15$–35 (black line). The radiative lifetime $\tau = \tau_0 n^3$ of a free Rydberg atom is plotted for comparison purposes (red line).

the continuum wave function $\psi_{k''}^{\text{vib}}$ has the asymptotic form

$$\psi_{k''}^{\text{vib}} \sim \sin(k''R + \eta) \tag{3.17}$$

where η is the scattering phase shift, which at low energies is given by $\eta = -k''a_s$ with a_s the s-wave scattering length. In the initial molecular state we approximate the true bound vibrational wavefunctions $\psi_{\nu'}^{\text{vib}}(R)$ by the eigenstates of a harmonic approximation to the molecular potential centered about $R = R_e$. Due to the asymmetric nature of the molecular potential curves, this approximation becomes progressively worse as ν' increases. However, we expect that the ability to impose an interatomic spacing close to the equilibrium distance of the targeted molecular state before applying the photoassociation pulse will provide a measure of control over the range of vibrational levels occupied by the molecules, thus making the lowest vibrational levels the most relevant.

Although there are a huge number of final states to which the molecule could decay, the dependence of the decay rate given by Eq. (3.14) on $(E_{\nu'} - E_{k''})^3$ favors transitions that involve the emission of a high-energy photon. We therefore consider only transitions that finish within the continuum above the $5s$–$5s$ potential curve, neglecting all other decay channels. The radiative lifetimes thus calculated for

the ground vibrational state $\nu' = 0$ are shown in Fig. 3.5; the lifetimes of higher vibrational levels (up to $\nu' = 10$) are the same to within $\sim 5\%$. Also plotted for comparison purposes is the radiative lifetime $\tau = \tau_0 n^3$ of a free Rydberg atom, where $\tau_0 = 1.4$ ns for ^{87}Rb [14]. Our calculations indicate that for $n \gtrsim 17$ the Rydberg dimers are more stable than the free atoms. For the highest molecular state considered ($n = 35$) we find lifetimes of the order of a few milliseconds, indicating that even if contributions from neglected decay channels were to reduce this lifetime by several orders of magnitude, the system could still be successfully interrogated and characterised by short (nanosecond to picosecond) laser pulses. To avoid possible stimulated emission contributions to the radiative decay process, the laser fields forming the optical lattice could be switched off as the Rydberg excitation pulse is applied. The subsequent free expansion of the atoms would not limit the window of time within which the system may be characterized, since the atoms are expected to remain localized within a few lattice spacings for a time of the order of 10 μs [102].

3.2.5 Decay via autoionisation

It has been known for some time that ionising decay channels – decay channels that involve the conversion of one or more atoms into ions, with the emission of free electrons – frequently play an important role in determining the dynamics and lifetime of Rydberg atoms in ultracold atomic gases. Experiments with ultracold, dense, Rydberg gases show that such systems typically spontaneously ionise to form an ultracold plasma on a time scale of a few μs [103, 104, 105, 106]. This is significantly shorter than the radiative lifetimes of Rydberg states with $n \gtrsim 10$ (cf. the red line of Figure 3.5), indicating the importance of ionising decay modes as compared with radiative decay modes in such systems.

The mechanism behind this ionisation is thought to be blackbody photoionisation of a small percentage of Rydberg atoms [107], followed by an avalanche of collisional ionisation as Rydberg atoms are accelerated by attractive or repulsive dipole-dipole forces [108, 109, 110, 111, 112, 113]. Despite its importance in such systems, we have neglected collisional ionisation in this work because our proposal is concerned with a very dilute ultracold gas prepared in a Mott insulator state. The rate of photoionisation and subsequent collisional avalanches is therefore significantly reduced as compared with the cold, dense, Rydberg gases mentioned above.

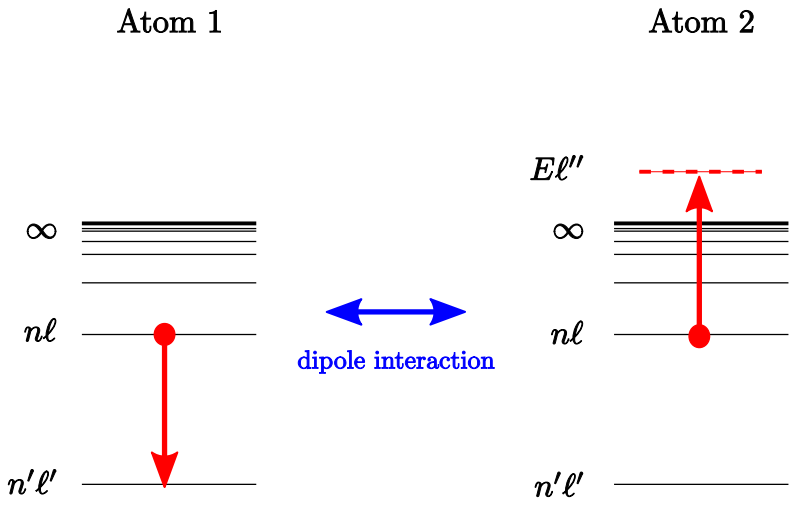

Figure 3.6: The process of autoionisation. Two Rydberg atoms are separated by a distance such that the two-atom states $|n\ell, n\ell\rangle$ and $|n'\ell', E\ell''\rangle$ are degenerate. One atom is ionised, while the other relaxes to a lower bound state, the process being driven by the dipole interaction. Figure after Amthor *et al.* [114].

However, theoretical and experimental results published since the completion of the work presented here suggest that collisional ionisation alone is not sufficient to explain the short lifetime of cold Rydberg gases against ion formation: other processes must also play a role [115]. One such process is autoionisation, where the dipole-dipole interactions between Rydberg atoms drive two-atom transitions of the form

$$|n\ell, n\ell\rangle \longrightarrow |n'\ell', E\ell''\rangle, \tag{3.18}$$

where $|E\ell''\rangle$ represents an continuum state with angular momentum ℓ'' and energy E. This process is schematically represented in Figure 3.6.

A recent theoretical paper investigated the relevance of this process to the autoionisation of a dilute ultracold Rydberg gas [114]. Studying a gas of Rydberg atoms interacting by long-range interactions, the authors concluded that the estimated rates of autoionisation are not sufficient to explain the observed non-collisional ionisation in Rydberg gases, and indeed are too small to be observed experimentally. However, since this paper considers the regime of $R \gg R_{LR}$, its conclusions do not necessarily extend to the regime of $R \sim R_{LR}$, in which our proposal lies. In fact, as pointed out in [114], the ionisation probability can be enhanced by several orders of magnitude when the electronic wavefunctions of the

atomic pair overlap one another [116]. Since the macrodimers that we study in this chapter have significant wavefunction overlap, autoionisation is expected to be an important factor in determining their decay behaviour and stability.

A quantitative calculation of autoionisation decay rates of the macrodimers of this chapter is a complicated task, which requires detailed knowledge of the wavefunctions of the bound molecular states in order to calculate the dipole matrix elements for both the bound-bound transition $|n\ell\rangle \longrightarrow |n'\ell'\rangle$ and the bound-free transition $|n\ell\rangle \longrightarrow |E\ell'\rangle$. This calculation goes beyond the scope of the work presented here. However, since autoionisation is expected to play an important role in determining the stability of these macrodimers, any further research in this direction should include calculations of autoionisation rates and their scaling behaviour with the atomic principal quantum number n.

3.3 Summary

In this chapter we showed that an optical lattice forming an array of double-well potentials may be exploited to selectively photoassociate pairs of atoms to molecular states with equilibrium distances of up to several hundred nanometries and binding energies of the order of 10^3 GHz, several orders of magnitude larger than the binding energies of long-range molecules stabilised by dipole-dipole forces. These molecular states are expected to have equilibrium distances of the order of typical optical lattice spacings. Decay via autoionisation is expected to be the dominant factor that determines the lifetime of these dimers. A quantitative computation of autoionisation decay rates is a priority for future research in this direction.

Chapter 4

Mesoscopic crystals of Rydberg-dressed atoms

Ultracold gases with dipolar interactions are a topic of intense current interest within atomic and laser physics. Due to the long range and anisotropic character of the dipole-dipole interaction, these systems display a rich range of physics: recent proposals for applications with dipolar gases include the formation of self-assembled crystalline structures [117, 118], the preparation of strongly-correlated many-body systems with three-body interactions [119, 120, 121], and the realization of novel quantum phases with hidden topological order [122, 123, 124]. When loaded into an optical lattice, dipolar particles can be used to realise extended Hubbard-type models [125] and are expected to form a ground state with a supersolid phase for accessible experimental parameters [126, 127, 128]. Two recent reviews [129, 130] give full details of the state of the art in ultracold dipolar gases.

Due to the existence of well-established cooling and trapping techniques, gases of neutral alkali atoms form an attractive system for the realisation of such systems. Since an atom in its ground state has zero electric dipole moment, experimental efforts in this direction have focused on elements with strong magnetic interactions. The magnetic elements of chromium [131, 130] and, very recently, dysprosium [132] have been successfully cooled to the regime of quantum degeneracy. However, the interaction of magnetic dipoles is significantly weaker than that of electric dipoles, and although it is possible to tune the strength of the magnetic dipolar interactions by using Feshbach resonances [133], attaining the regime in which the dipolar interaction is dominant over the isotropic contact interaction remains a difficult

task. This observation motivates the study of atomic gases with induced electric dipolar interactions.

In order to induce a non-zero electric dipole moment in the ground state of an alkali atom, an external field must be applied. Due to the small electric polarisability of the ground state, direct polarisation by way of a static electric field would require an extremely strong field. However, an alternative method that exploits the enormous electric dipole moments of the Rydberg states has been proposed [73, 74]. By weakly coupling the ground state to a Rydberg state with an incident laser, a small amount of the Rydberg electric dipole moment is admixed into the ground state, producing an time-averaged non-zero electric dipole moment in the neutral atom. Rydberg-dressed alkali atoms thus form promising systems for the future study of ultra-cold dipolar physics.

Motivated by these observations, we now study mesoscopic crystals of dipolar particles held in a 2D harmonic trapping potential. We analyse the equilibrium structure of the crystals, investigate the process by which they melt, and obtain an estimate of their melting temperatures.

In the second half of the chapter we outline two possible schemes for inducing dipolar interactions between neutral ground-state atoms by using off-resonant laser light to weakly couple the atomic ground state to an excited Rydberg state. By extending the radiative cascade simulations of Chapter 2, we compute the rate of atomic recoil heating resulting from spontaneous emission within one of these schemes, and analyse the extent to which the use of a reduced three-level approximation, in place of the full atomic level structure, is justified.

This work originated as part of a project carried out in collaboration with Guido Pupillo, Andrea Micheli, and Peter Zoller at the University of Innsbruck. All calculations and analysis contained in this chapter are the work of the present author. The Innsbruck group has continued their research in this direction; their findings have very recently been published [134].

4.1 Mesoscopic clusters of dipolar particles in a harmonic trap

A cluster of dipolar particles held in a harmonic trapping potential and restricted to move in two dimensions is predicted to exhibit several quantum phases, depending on the relative strengths of the dipolar interaction and the trapping potential [135].

For sufficiently strong dipolar interactions, the cluster is expected to behave as a classical crystal [74]. In this section we present results on the zero-temperature structure and melting behaviour of these mesoscopic classical crystals of dipolar particles.

4.1.1 System overview

We consider a collection of N particles, each of which has mass m and an electric dipole moment of magnitude d, moving in the x-y plane. The dipole moments of the particles are aligned perpendicular to the plane, so that in-plane interactions between the particles are strictly repulsive. In-plane confinement is provided by a radially symmetric harmonic trapping potential with frequency ω. We neglect particle motion in the z direction, which is assumed to be frozen out by the application of a strong trapping potential along that axis. This system could be realised by a collection of neutral atoms loaded into a single site of a tight 1D optical lattice, with a radial trapping potential provided by the Gaussian profile of the trapping beam.

Assuming purely dipolar interactions between the particles, the Hamiltonian for the system reads

$$\frac{H}{E_0} = \sum_{i=1}^{N} \left[\frac{\mathbf{p}_i^2}{2\kappa^2} + \frac{\mathbf{r}_i^2}{2} \right] + \sum_{\substack{i=1 \\ j>i}}^{N} \frac{1}{|\mathbf{r}_i - \mathbf{r}_j|^3} \tag{4.1}$$

where $\mathbf{r}_i = (x_i, y_i)$ and $\mathbf{p}_i = (p_x^{(i)}, p_y^{(i)})$ are 2D position and momentum of the i^{th} particle measured in dimensionless units; length, momentum, and energy scales have been defined as

$$r_0 = \left(\frac{d^2}{4\pi\varepsilon_0 m\omega^2} \right)^{1/5}, \qquad p_0 = \frac{\hbar}{r_0}, \qquad E_0 = m\omega^2 r_0^2, \tag{4.2}$$

and $\kappa = E_0/(\hbar\omega)$ is a dimensionless constant that characterises the strength of the dipole-dipole interaction. In the limit of strong interactions ($\kappa \gg 1$) the system is expected to behave as a classical crystal [136]. In what follows, we treat the system semi-classically; that is, we treat the position $\mathbf{r}_i$ and momentum $\mathbf{p}_i$ as classical variables.

The structure and dynamics of clusters of trapped dipolar particles have previously been investigated in [137, 138], which also contain results on the melting

of large clusters ($N \sim 40 - 80$). Here we present complementary results for the mesoscopic regime ($N \leq 40$).

4.1.2 Equilibrium crystal structures

To find the equilibrium structure of the cluster, we minimise the total potential energy

$$E_{\text{pot}} = \sum_{i=1}^{N} \frac{\mathbf{r}_i^2}{2} + \sum_{\substack{i=1 \\ j>i}}^{N} \frac{1}{|\mathbf{r}_i - \mathbf{r}_j|^3}, \tag{4.3}$$

which is a function of the $2N$ position variables only. Figure 4.1 shows the equilibrium configurations of clusters of various sizes up to $N = 40$, which show the following general trend: for small values of N, the cluster forms a regular collection of polygonal shells. As the cluster size is increased, additional particles join the outermost shell or contribute to the formation of a new shell. For clusters with $N \gtrsim 20$, defects in the shell structure begin to appear; the shell structure gradually gives way to a regular triangular lattice, which is the dominant ordering for $N \gtrsim 30$.

4.1.3 Melting behaviour

In order to gain an understanding of the robustness of the crystalline structures against heating, we now investigate how, and at what temperature, they melt. We achieve this by using Monte Carlo sampling to calculate canonical ensemble averages of crystal order parameters. We employ the standard Metropolis sampling scheme; all temperatures are given in terms of $T_0 = E_0/k_B$, which for typical experimental parameters is of the order of 100 nK — 10 μK. Full details of the order parameters are given in the next section. We find that as the temperature of the cluster is increased, the crystalline structure vanishes in the following fashion (cf. [138]):

(i) At $T \lesssim 1 \times 10^{-4}$ the shells begin to rotate freely relative to one another. The low activation temperature indicates that the potential energy barrier for this mode of motion is very small; this is a consequence of the radial symmetry of the in-plane confinement. This rotation could be prevented by making the trapping potential anisotropic.

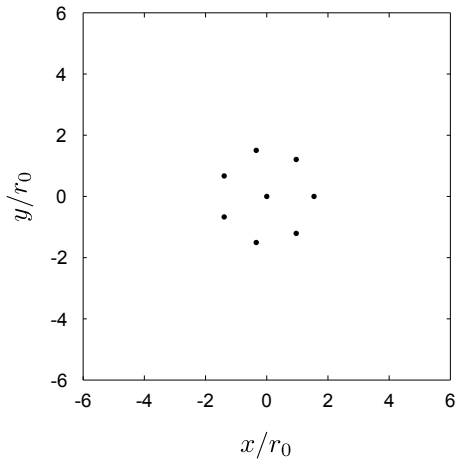

(a) $N = 8$, $E_{\mathrm{pot}} = 13.9099$

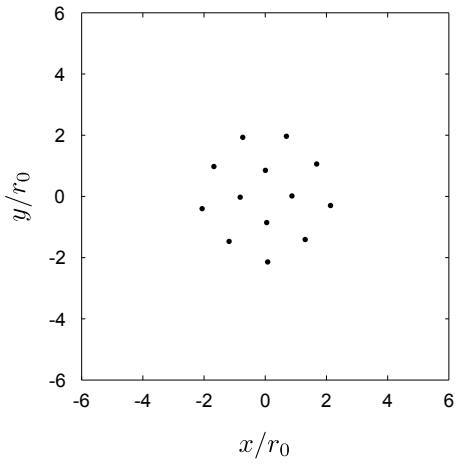

(b) $N = 13$, $E_{\mathrm{pot}} = 33.4060$

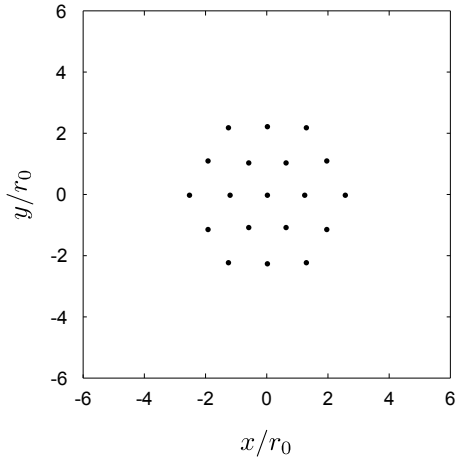

(c) $N = 19$, $E_{\mathrm{pot}} = 64.9342$

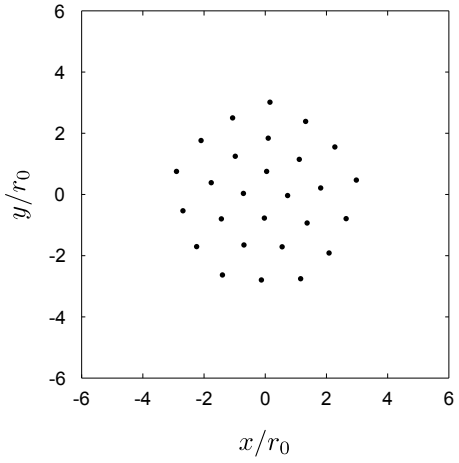

(d) $N = 27$, $E_{\mathrm{pot}} = 119.0663$

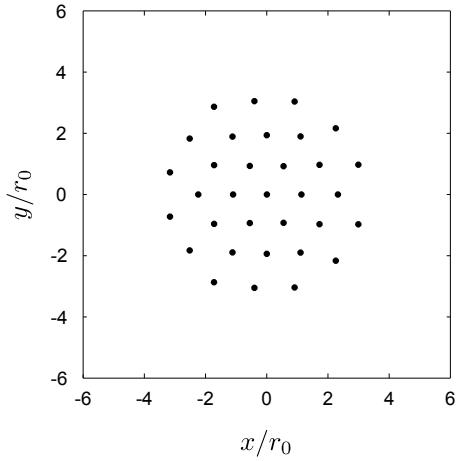

(e) $N = 33$, $E_{\mathrm{pot}} = 167.3695$

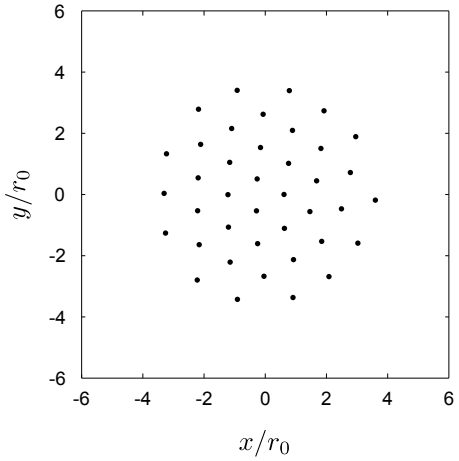

(f) $N = 40$, $E_{\mathrm{pot}} = 231.8685$

Figure 4.1: Equilibrium configurations of dipolar particles in a harmonic trap. For larger numbers of particles the triangular lattice becomes increasingly dominant over the shell structure.

(ii) At $T \simeq T_1$, the shells begin to exchange particles. As the temperature increases further, the shells exchange particles freely, but remain well-defined: i.e. the radial deviations of the particles within a shell remain smaller than the radial distance between shells.

(iii) At $T \simeq T_2$, the radial deviations of the particles within each shell become comparable to the distance between the shells, and the cluster no longer exhibits any shell structure.

Figure 4.2 illustrates this sequence for the cluster with $N = 10$. The left-hand plots show 1×10^4 spatial configurations drawn from the canonical ensemble and plotted in the x-y plane. The right-hand plots show histogram counts for the radial coordinates of two particles, one from each shell, obtained from 1×10^6 samples from the canonical ensemble.

Note that even though the trapping potential is isotropic in the x and y directions, the configurations in the left-hand plots of Figure 4.2 do not show the expected circular symmetry. This is not a physical reality, but an artefact of the analysis: before each configuration was plotted, a global rotation was applied to bring the azimuthal angle of particle 1 in our predetermined numbering scheme (this corresponds to the particle located at approximately $(0.8, 0)$ in the $N = 10$ equilibrium configuration) to zero. This was done in order to be able to distinguish relative rotation of the inner and outer shells (which is the first step in the melting process) from absolute rotation of the entire crystal (which is energetically costless, and therefore always present). Within this convention, a shell only appears as a solid band if it is rotating relative to the shell in which particle 1 lies; otherwise, both shells would always appear as solid bands due to the costless global rotation mode.

The melting of the shell structure is apparent on viewing the evolution of the the radial probability density function of an individual particle as a function of temperature. For $T < T_1$ the pdf is a narrow peak centred about the equilibrium value of r. As T increases past T_1 the radial pdf evolves into a mixture of peaks at different values of r, consistent with the particle moving between shells. However, there is no significant probability to find the particle *between* shells until significantly higher temperatures. As T increases further, the probability peaks continue to broaden until they begin to overlap at $T \simeq T_2$. At this point the particle has a non-zero probability of being found between the shells, and the cluster no longer has a distinguishable shell structure.

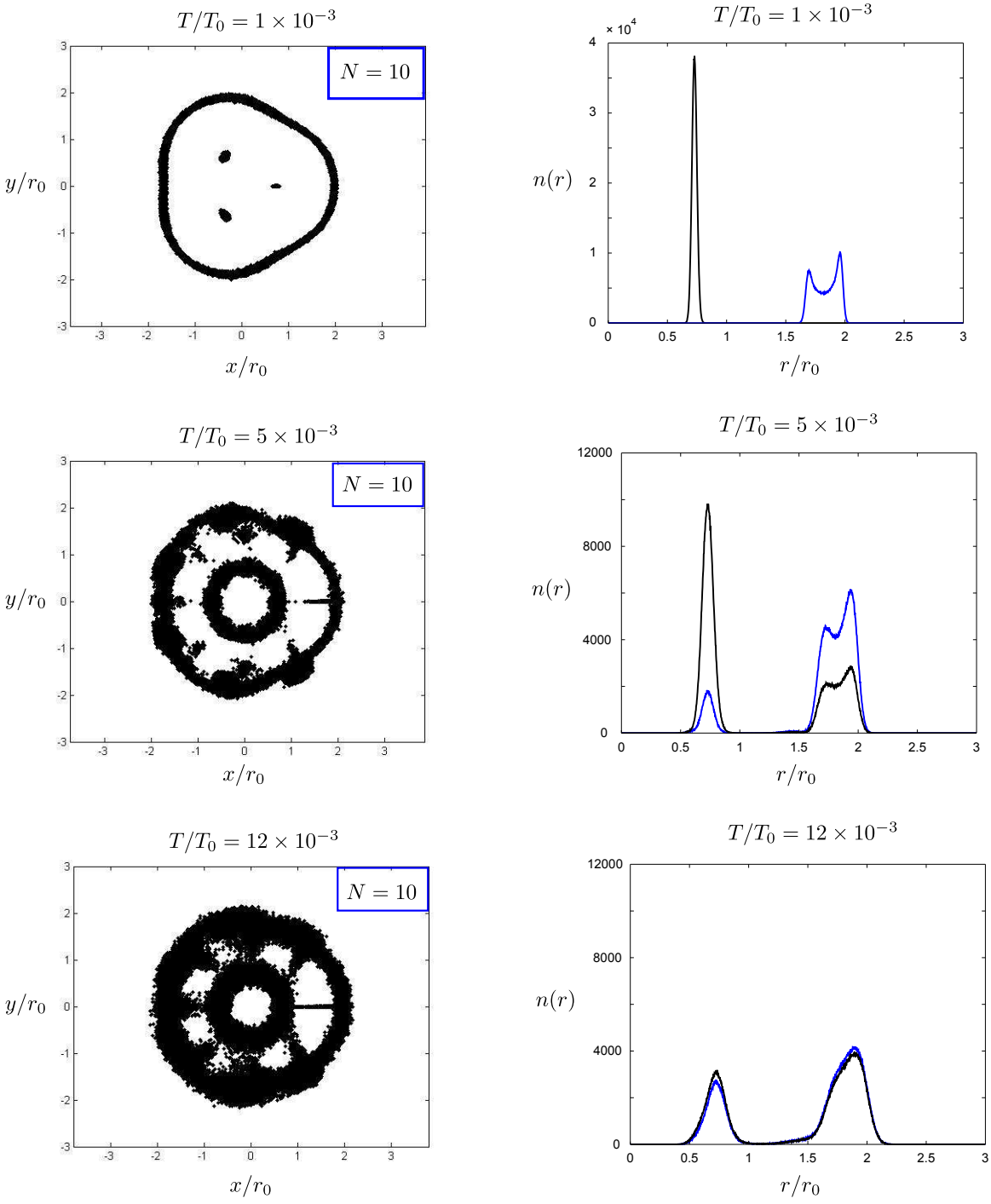

Figure 4.2: Illustration of the melting process of a 10-particle cluster. The figures in the left column show 1×10^4 spatial configurations drawn from the canonical ensemble and plotted in the x-y plane (see text); the right-hand figures show histogram counts for the radial coordinates of two particles, one from each shell, obtained from 1×10^6 samples drawn from the canonical ensemble. From top to bottom, the temperature of the ensemble is $T/T_0 = (1, 5, 12) \times 10^{-3}$. Particles exchange between shells at $T > T_1 = 3.5 \times 10^{-3}$, and the shell structure disintegrates for $T > T_2 \approx 2 \times 10^{-2}$.

4.1.4 Extracting the melting temperatures

In order to extract the value of T_1 from the canonical ensemble samples generated we define the radial deviation δr_i $(i = 1, 2, \ldots, N)$ for each cluster configuration by $\delta r_i = r_i - \langle r_i \rangle$, where $\langle r_i \rangle$ indicates the Monte Carlo average over all generated configurations. The variance in the radial coordinate of the i^{th} particle which increases sharply at $T = T_1$ as as particles begin switching between shells, is then $\langle (\delta r_i)^2 \rangle$. We therefore introduce the dimensionless quantity

$$(\delta r)_{\text{tot}} = \frac{1}{Na^2} \sum_{i=1}^{N} \langle (\delta r_i)^2 \rangle, \tag{4.4}$$

where a is the average interparticle separation of the cluster at $T = 0$, and define T_1 to be the temperature at which $(\delta r)_{\text{tot}}$ shows a sharp increase. Figure 4.3 illustrates the temperature dependence of $(\delta r)_{\text{tot}}$ for clusters of various sizes.

4.1.5 Melting temperatures of mesoscopic crystals

We generated up to 1×10^6 configurations of dipolar clusters of up to 30 particles from the canonical distribution, and used the order statistic $(\delta r)_{\text{tot}}$ to obtain a value for the melting temperature T_1 for each cluster. The melting temperatures are plotted in Figure 4.4. In agreement with what was reported in [138] for larger clusters, we find that the melting temperature is a non-monotonic function of N, with the most stable clusters being those with a completed outer shell of particles. We compared our results for $N = 19$ and $N = 35$ with the figures quoted in [138], and found our melting temperatures to be smaller by a factor of approximately 2. We do not consider this difference to be significant, since it is smaller than the width of the melting transition (see Figure 4.3).

4.2 Dipole moments in Rydberg-dressed atoms

An electric dipole moment may be induced in the ground state $|g\rangle$ of a neutral alkali atom by using laser light to weakly couple $|g\rangle$ to a Rydberg state $|r\rangle$ of the atom. The resultant dressed state contains a small fraction of the large electric dipole moment of $|r\rangle$, which gives rise to dipole-dipole interactions between the neutral atoms. In this section we outline two schemes by which this Rydberg dressing could be realized.

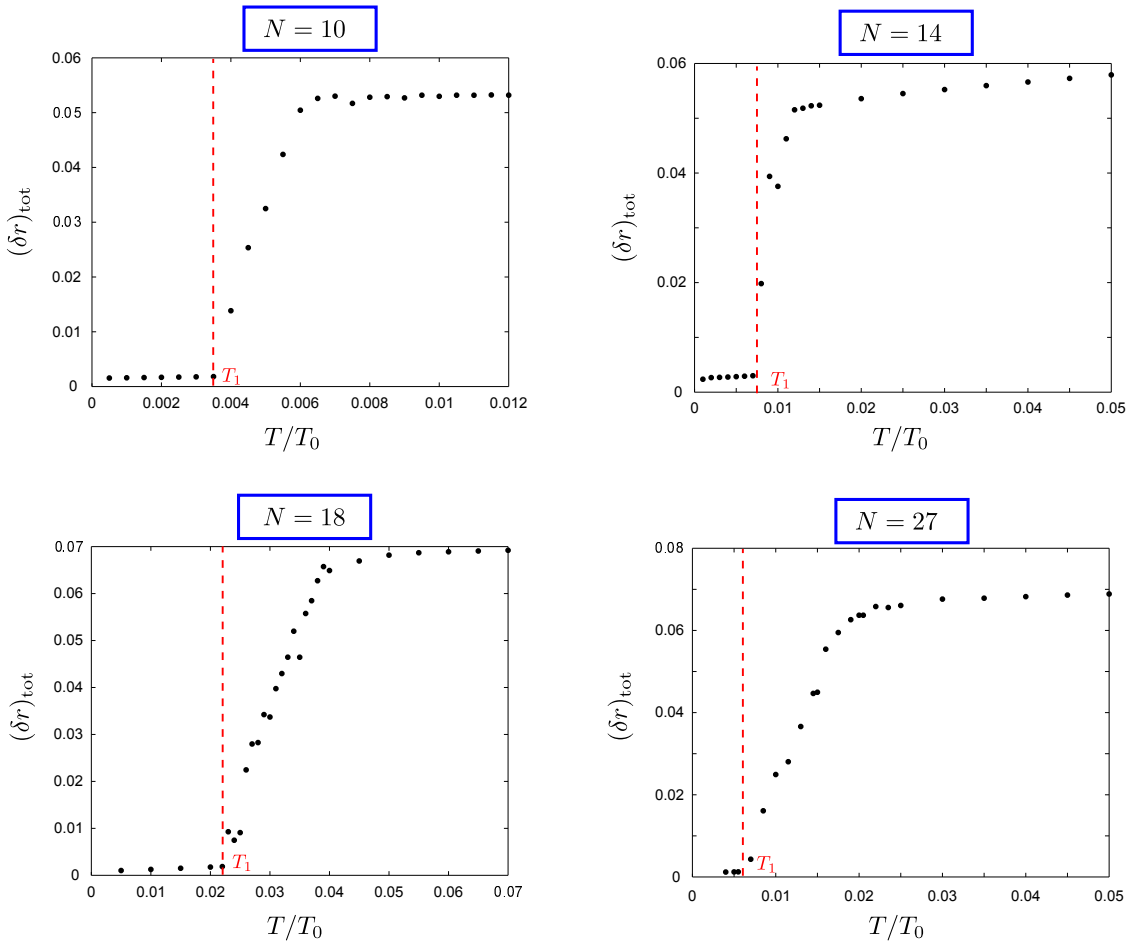

Figure 4.3: The variation of $(\delta r)_{\rm tot}$ with temperature for clusters of different sizes. The extracted melting temperature T_1 is indicated in each case.

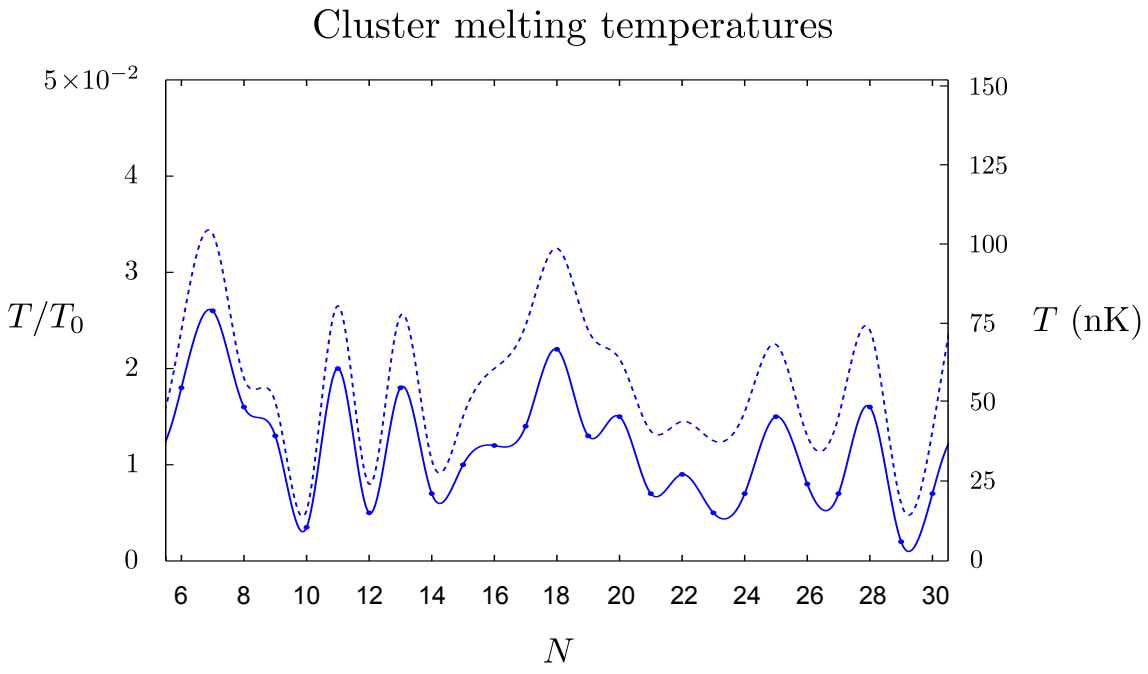

Figure 4.4: The melting temperatures of dipolar clusters of $N = 6$ to 30 particles. Solid line: the temperature T_1 at which particles begin to exchange between shells. Dashed line: an estimate of the width of the melting transition. Left axis: the scaled temperature T/T_0. Right axis: the corresponding temperature in nK, for a system of rubidium atoms ($m = 85.5$ u) with $\omega = 2\pi \times 3$ kHz, $d = 7\ ea_0 \approx 18$ Debye. These parameters correspond to $r_0 \approx 910$ nm, $\kappa \approx 21$, $T_0 \approx 3\ \mu$K.

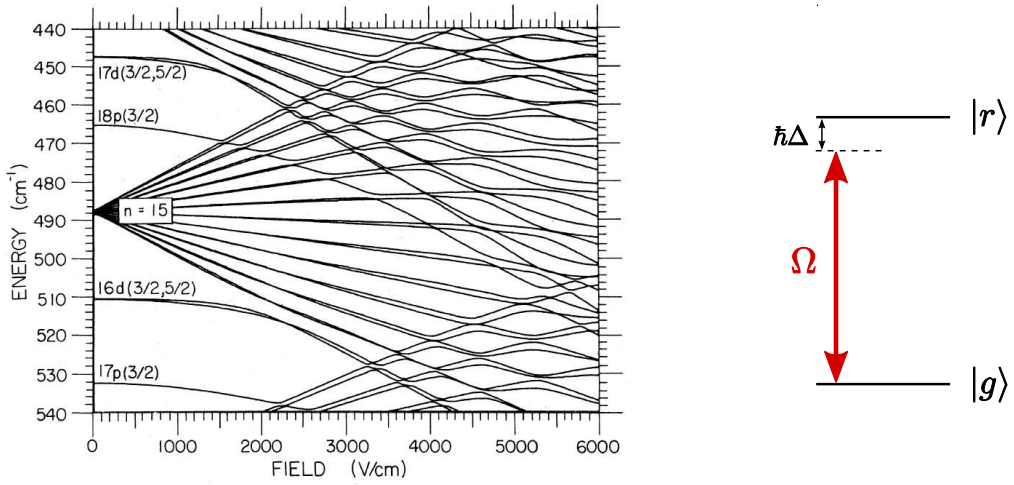

(a) (b)

Figure 4.5: (a) The Stark map of $|m_j| = \frac{3}{2}$ states of rubidium in the neighbourhood of $n = 15$, showing the characteristic Stark fan structure. The highest-energy Stark state of the $n = 15$ manifold would be a good candidate to use for $|r\rangle$ in the dressing scheme of §4.2.1: for electric fields below ~ 1500 V/cm it is well separated in energy from neighbouring states and exhibits a strong energy shift, indicating a large electric dipole moment. Reprinted Figure 16 with permission from [139], available at https://journals.aps.org/pra/abstract/10.1103/PhysRevA.20.2251. Copyright (1979) by the American Physical Society. (b) The two-level atomic model of §4.2.1: the ground state $|g\rangle$ is coupled to a Rydberg Stark state $|r\rangle$ by an off-resonant laser beam with Rabi frequency Ω and detuning Δ.

4.2.1 Ground state coupled to a Stark-split Rydberg state

When a static electric field is applied to a neutral alkali atom, the atomic energy levels split into a 'Stark fan' (see Figure 4.5(a) for an example). Each energy eigenstate is a mixture of bare (field-free) eigenstates, and has an induced permanent electric dipole moment. If required, the exact eigenstates may be obtained by diagonalising the Hamiltonian describing the atom-field interaction (see e.g. [139]); however, for many purposes they are well approximated by the hydrogenic result, for which analytic solutions are available [68, 140].

The energy eigenstates of hydrogen in a static electric field $\mathbf{E} = E_z\,\hat{\mathbf{z}}$ can be written as $|n, m, n_1, n_2\rangle$, where $n \geq 1$ is the principal quantum number, $m \geq 0$ is the modulus of the magnetic quantum number, and n_1 and n_2 are parabolic quantum numbers that take on integer values such that $n_1 + n_2 = n - m - 1$. To

first order in the field strength E_z, this state has an energy (in atomic units) of

$$E_{n,n_1,n_2,m} = -\frac{1}{2n^2} - \frac{3E_z}{2} n(n_1 - n_2) \tag{4.5}$$

and a constant induced electric dipole moment of $\mathbf{d} = \frac{3}{2} n(n_1 - n_2)\hat{\mathbf{z}}$.

Here we consider applying an off-resonant laser field to couple the atomic ground state $|g\rangle$ to the highest-energy Stark state of a particular n, m manifold. The resultant dynamics can be studied by considering a simple two-level model, which is illustrated in Figure 4.5(b). We expand the atomic state vector as $|\psi(t)\rangle = c_g(t)\,|g\rangle + c_r(t)\,|r\rangle$. This evolves subject to the Hamiltonian

$$H = \frac{\hbar\Delta}{2}\big(|g\rangle\langle g| - |r\rangle\langle r|\big) + \hbar\Omega\big(|r\rangle\langle g| + |g\rangle\langle r|\big) \tag{4.6}$$

where Ω is the Rabi frequency of the driven $|g\rangle \leftrightarrow |r\rangle$ transition, and Δ is the detuning of the driving laser from the state $|r\rangle$. The electric dipole moment of the atom is given by

$$\mathbf{d}(t) = \big|c_g(t)\big|^2\,\mathbf{d}_{gg} + c_g^*(t)\,c_r(t)\,\mathbf{d}_{gr} + c_g(t)\,c_r^*(t)\,\mathbf{d}_{rg} + \big|c_r(t)\big|^2\,\mathbf{d}_{rr},$$

where $\mathbf{d}_{gg} = \langle g|\hat{\mathbf{d}}|g\rangle$ is the electric dipole moment of the state $|g\rangle$, with $\hat{\mathbf{d}} = -e\hat{\mathbf{r}}$ the electric dipole moment operator. These quantities satisfy $|\mathbf{d}_{rr}| \gg |\mathbf{d}_{gr}|, |\mathbf{d}_{rg}|, |\mathbf{d}_{gg}|$. Solving the time-dependent Schrödinger equation subject to the initial condition of $c_g(0) = 1$, $c_r(0) = 0$ gives

$$c_g(t) = \cos\left(\tfrac{1}{2}\sqrt{4\Omega^2 + \Delta^2}\,t\right) - \frac{\mathrm{i}\Delta}{\sqrt{4\Omega^2 + \Delta^2}} \sin\left(\tfrac{1}{2}\sqrt{4\Omega^2 + \Delta^2}\,t\right) \tag{4.7a}$$

$$c_r(t) = \frac{-2\mathrm{i}\Omega}{\sqrt{4\Omega^2 + \Delta^2}} \sin\left(\tfrac{1}{2}\sqrt{4\Omega^2 + \Delta^2}\,t\right). \tag{4.7b}$$

We are interested in the parameter regime where $2\Omega \ll \Delta$. In this case the effective Rabi frequency $\Omega' = \frac{1}{2}\sqrt{(2\Omega)^2 + \Delta^2}$ at which the dipole moment oscillates is much larger than Ω, and the dipole moment $\mathbf{d}(t)$ can be replaced by its time-averaged value:

$$\bar{\mathbf{d}} = \frac{\Omega'}{2\pi} \int_0^{\frac{2\pi}{\Omega'}} \mathbf{d}(t')\,\mathrm{d}t'. \tag{4.8}$$

To second order in the small parameter Ω/Δ, we have

$$\bar{\mathbf{d}} = \left(1 - \frac{2\Omega^2}{\Delta^2}\right)\mathbf{d}_{gg} + \frac{\Omega}{\Delta}\left(\mathbf{d}_{rg} + \mathbf{d}_{gr}\right) + \frac{2\Omega^2}{\Delta^2}\,\mathbf{d}_{rr}. \tag{4.9}$$

For typical values of the Rydberg principal quantum number ($n \sim$ 20-50), the dipole moment $\mathbf{d}_{rr}$ is several orders of magnitude larger than $\mathbf{d}_{gg}, \mathbf{d}_{gr}$, and $\mathbf{d}_{rg}$. To a very good approximation the atom exhibits an induced electric dipole moment of (in atomic units)

$$\bar{\mathbf{d}} \approx 3\left(\frac{\Omega}{\Delta}\right)^2 n(n-1)\,\hat{\mathbf{z}}. \tag{4.10}$$

It is important to note that this treatment focuses only on the single-atom dynamics, and neglects the impact of any multi-particle effects on the dressing scheme. Equation 4.10 is therefore valid in the regime where any interaction-induced level shift V_{rr} is much smaller than the laser detuning Δ, so that the dressing is not significantly affected by the interactions. If we assume that only two-body interactions are important, and that the interaction energy has the simple form $V_{rr} = \pm C_3/R^3$, with R the interatomic separation, we find a minimum atomic separation of $R_c \sim \left(|C_3|/\Delta\right)^{1/3}$. Thus Eq. (4.10) is only valid for atoms that are separated from their neighbours by $R \gg R_c$.

A recent theoretical treatment of interactions between Rydberg-dressed ground state atoms describes how the interaction potential is modified at smaller values of R due to two-atom interactions [141]. The mechanism is the following feedback effect: the interaction-induced level shifts change the effective detuning of the laser dressing, which affects the strength of the coupling between $|g\rangle$ and $|r\rangle$, and so the size of the induced dipole moment. The net result is that the effective interaction between a pair of Rydberg-dressed atoms is expected to deviate from a $1/R^3$ form for $R \sim R_c$, becoming independent of R at small R [141].

4.2.2 Ground state coupled to a dressed Rydberg state

It is also possible to use a Rydberg state to induce an effective electric dipole moment in the ground state without applying an external electric field. In this case a microwave field is used to resonantly couple a pair of Rydberg states of opposite parity, such as an s and a p state. This resonant coupling converts the s and p states into a pair of dressed states, each of which has mixed s+p character and

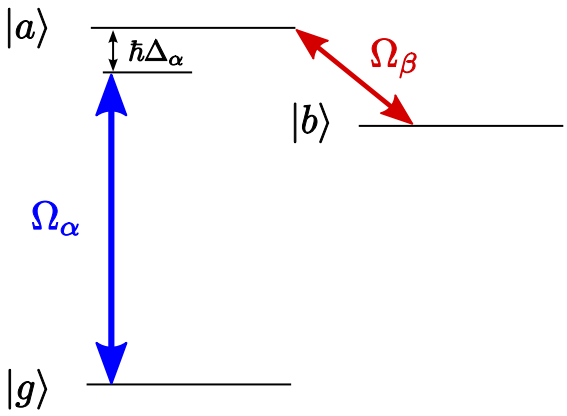

Figure 4.6: The atomic level scheme considered in the dressing scheme of Section 4.2.2. The resonant dressing field Ω_β converts $|a\rangle$ and $|b\rangle$ into a pair of dressed states with a rapidly-oscillating electric dipole moment. The dressing field Ω_α then off-resonantly couples one of these dressed states to the atomic ground state.

a rapidly-oscillating electric dipole moment. By applying an off-resonant optical field to weakly couple one of these dressed states to the atomic ground state, an effective electric dipole moment is induced in the ground state of the atom.

To gain further insight into this dressing scheme we consider a simple model based on the atomic level structure illustrated in Figure 4.6. The ground state $|g\rangle$ is off-resonantly coupled to a Rydberg state $|a\rangle$; the Rabi frequency and detuning of this coupling are given by Ω_α and Δ_α respectively. A second field resonantly couples $|a\rangle$ to another Rydberg state $|b\rangle$ with Rabi frequency Ω_β. The parameter regime of interest for inducing a weak admixture of $|a\rangle$ and $|b\rangle$ into $|g\rangle$ is $(\Omega_\alpha, \Omega_\beta) \ll \Delta_\alpha$. The atomic Hamiltonian can be written in a suitable interaction picture as $H_0+H_\alpha+H_\beta$, where

$$H_0 = -\hbar\Delta_\alpha \big(|a\rangle\langle a| + |b\rangle\langle b|\big), \tag{4.11a}$$

$$H_\alpha = \tfrac{1}{2}\hbar\Omega_\alpha \big(|g\rangle\langle a| + |a\rangle\langle g|\big), \tag{4.11b}$$

$$H_\beta = \tfrac{1}{2}\hbar\Omega_\beta \big(|b\rangle\langle a| + |a\rangle\langle b|\big). \tag{4.11c}$$

The eigenstates of $H_0 + H_\beta$ can be written down exactly. In terms of the bare atomic states $|g\rangle, |a\rangle, |b\rangle$, they are given by

$$|v_g\rangle = |g\rangle, \qquad |v_\pm\rangle = \frac{1}{\sqrt{2}}\big(|b\rangle \pm |a\rangle\big). \tag{4.12}$$

In the regime where $(\Omega_\alpha, \Omega_\beta) \ll \Delta_\alpha$, the coupling induced by H_α can be treated as a perturbation on top of $H_0 + H_\beta$. In this case, the atomic eigenstates to first

order in the perturbation are

$$\begin{pmatrix} |\psi_+\rangle \\ |\psi_-\rangle \\ |\psi_g\rangle \end{pmatrix} = \begin{pmatrix} 1 & 0 & -\frac{x}{\sqrt{2}(1-y)} \\ 0 & 1 & \frac{x}{\sqrt{2}(1+y)} \\ \frac{x}{\sqrt{2}(1-y)} & -\frac{x}{\sqrt{2}(1+y)} & 1 \end{pmatrix} \begin{pmatrix} |v_+\rangle \\ |v_-\rangle \\ |v_g\rangle \end{pmatrix} \tag{4.13}$$

where $|\psi_i\rangle$ is the state that connects adiabatically to $|v_i\rangle$ as $x \to 0$, and $x = \Omega_\alpha/(2\Delta_\alpha)$ and $y = \Omega_\beta/(2\Delta_\alpha)$ are small dimensionless parameters. The eigenenergies of the system are unchanged to first order in the perturbation. By inverting the transformation to express the ground state $|g\rangle$ in terms of the dressed eigenstates and assuming that the transition dipole moments $|\mathbf{d}_{ga}|$ and $|\mathbf{d}_{gb}|$ are negligible in comparison with $|\mathbf{d}_{ab}|$, we find that the induced electric dipole moment of an atom prepared in the ground state $|g\rangle$ at time $t = 0$ is approximately

$$\begin{aligned} \mathbf{d}(t) &= \mathbf{d}_{ab}\left[\frac{x^2}{(1-y)^2}\Big[1-\cos\big((1-y)\Delta_\alpha t\big)\Big] - \frac{x^2}{(1+y)^2}\Big[1-\cos\big((1+y)\Delta_\alpha t\big)\Big]\right] \\ &\approx \mathbf{d}_{ab}\, x^2\Big[4y\big(1-\cos\Delta_\alpha t\,\cos\tfrac{1}{2}\Omega_\beta t\big) - 2\sin\Delta_\alpha t\,\sin\tfrac{1}{2}\Omega_\beta t\Big], \end{aligned} \tag{4.14}$$

where the second line is valid when $(1 \pm y)^{-2} \approx (1 \mp 2y)$. Thus $\mathbf{d}(t)$ has a time-averaged value of $4x^2y\,\mathbf{d}_{ab}$, about which fluctuations of size $4x^2y$ (on a timescale $t_1 = 2\pi/\Delta_\alpha$) and $2x^2$ (on a timescale $t_2 = 4\pi/\Omega_\beta$) take place.

Typical experimental parameters for this dressing scheme could be $\Delta_\alpha = 2\pi \times 1$ GHz, $\Omega_\alpha = 2\pi \times 200$ MHz, $\Omega_\beta = 2\pi \times 300$ MHz, corresponding to $x = 0.1$, $y = 0.15$.

4.3 Heating by spontaneous emission: a comparison of level schemes

As noted in Chapter 2, it is a common approximation in the study of systems of Rydberg atoms to assume that all spontaneous emission events lead directly to the ground state. In analysing the microwave dressing scheme of §4.2.2, for example, this leads to a three-level approximation of the atom: the states $|a\rangle, |b\rangle$, and $|g\rangle$ are retained, but all other states $\{|i\rangle\}$ are ignored [136, 74].

In view of the results of Chapter 2, which indicate that a complete treatment of the atomic level scheme is important, we now make a quantitative comparison of the rate of heating within the microwave dressing scheme of §4.2.2 for two different treatments of the atomic level structure. The two different atomic level schemes we

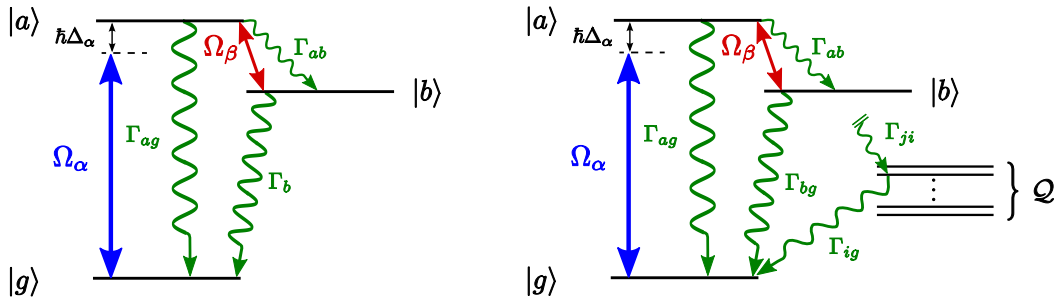

Figure 4.7: The two atomic level schemes compared in §4.3. (a) In the three-level approximation, the atom is restricted to the driven subspace $\mathcal{P} = \text{span}(|g\rangle, |a\rangle, |b\rangle)$. (b) The full set of atomic levels includes the non-driven subspace $\mathcal{Q} = \mathcal{P}^{\perp}$. Within the full atomic level scheme, a decay event from state $|a\rangle$ or $|b\rangle$ can leave the atom in any one of a large number of different states in $\mathcal{Q}$, from which it eventually returns to the ground state $|g\rangle$.

consider are illustrated in Figure 4.7. Firstly, we consider the case where the atomic state is restricted to the driven subspace $\mathcal{P} = \text{span}(|g\rangle, |a\rangle, |b\rangle)$. This treatment, which we will refer to as the three-level approximation, ignores the existence of the non-driven subspace $\mathcal{Q} = \mathcal{P}^{\perp}$. Secondly, we consider the case where the full set of atomic levels is included, and compare the rate of heating with the corresponding prediction within the three-level approximation.

4.3.1 Atomic dynamics

Coherent dynamics

In the absence of spontaneous emission, the atomic state evolves coherently within the driven subspace $\mathcal{P}$ under the influence of the Hamiltonian of Eq. (4.11): $H = H_0 + H_\alpha + H_\beta$, where

$$H_0 = -\hbar\Delta_\alpha \left(\sigma_{aa} + \sigma_{bb}\right), \tag{4.15a}$$

$$H_\alpha = \tfrac{1}{2}\hbar\Omega_\alpha \left(\sigma_{ga} + \sigma_{ag}\right), \tag{4.15b}$$

$$H_\beta = \tfrac{1}{2}\hbar\Omega_\beta \left(\sigma_{ba} + \sigma_{ab}\right). \tag{4.15c}$$

Here $\sigma_{ij} = |i\rangle\langle j|$ is an atomic transition operator. The atomic density matrix $\rho(t) = |\phi(t)\rangle\langle\phi(t)|$ evolves according to the von Neumann equation:

$$\frac{\mathrm{d}\rho}{\mathrm{d}t} = \frac{1}{\mathrm{i}\hbar}\left[H, \rho\right]. \tag{4.16}$$

Dissipative dynamics

To include spontaneous emission in the atomic evolution, it is sufficient to add the terms arising from the irreversible coupling of the atom with the vacuum radiation field directly to the coherent evolution of Eq. (4.16). Denoting the average decay rate from state $|i\rangle \equiv (n_i, \ell_i, m_i)$ to state $|j\rangle \equiv (n_j, \ell_j, m_j)$ by $\Gamma_{i\to j} \equiv \Gamma^{n_j,\ell_j,m_j}_{n_i,\ell_i,m_i}$ and setting $\Gamma_i \equiv \Gamma_{n_i,\ell_i,m_i} = \sum_j \Gamma_{i\to j}$, the appropriate terms to add to the master equation are (see e.g. §IV.C of [142]):

$$\sum_{i,\,j\neq i} \Gamma_{j\to i}\,\sigma_{ij}\,\rho\,\sigma_{ji} - \sum_{i,\,j\neq i} \Gamma_{i\to j}\,\sigma_{ii}\,\rho\,\sigma_{ii} \tag{4.17a}$$

$$-\frac{1}{2}\sum_{i,\,j\neq i} \Gamma_{i}\,\sigma_{ii}\,\rho\,\sigma_{jj} - \frac{1}{2}\sum_{i,\,j\neq i} \Gamma_{j}\,\sigma_{ii}\,\rho\,\sigma_{jj}. \tag{4.17b}$$

The first two terms describe the feeding and decay of the population $\rho_{ii} = \langle i|\rho|i\rangle$, while the second two describe the decay of the atomic coherences $\rho_{ij} = \langle i|\rho|j\rangle$. The full master equation in the presence of spontaneous emission is thus

$$\begin{aligned}\frac{\mathrm{d}\rho}{\mathrm{d}t} = \frac{1}{\mathrm{i}\hbar}\,[H,\rho] &+ \sum_{i,\,j\neq i} \Gamma_{j\to i}\,\sigma_{ij}\,\rho\,\sigma_{ji} - \sum_{i,\,j\neq i} \Gamma_{i\to j}\,\sigma_{ii}\,\rho\,\sigma_{ii} \\ &- \tfrac{1}{2}\sum_{i,\,j\neq i} \Gamma_{i}\,\sigma_{ii}\,\rho\,\sigma_{jj} - \tfrac{1}{2}\sum_{i,\,j\neq i} \Gamma_{j}\,\sigma_{ii}\,\rho\,\sigma_{jj}.\end{aligned} \tag{4.18}$$

4.3.2 Three-level approximation: the optical Bloch equations

In order to restrict the atomic system to the states $|a\rangle, |b\rangle, |g\rangle$ while maintaining the correct decay properties of $|a\rangle$ and $|b\rangle$ we divert all decay paths into $\mathcal{Q}$ to instead lead into $|g\rangle$; that is, we set

$$\Gamma_{a\to g} = \Gamma_{a\to g} + \sum_{i\in\mathcal{Q}} \Gamma_{a\to i}, \qquad \Gamma_{b\to g} = \Gamma_{b\to g} + \sum_{i\in\mathcal{Q}} \Gamma_{b\to i}. \tag{4.19}$$

Within the three-level approximation, the density matrix ρ is 3×3; by flattening the density matrix into a vector, the master equation of Eq. (4.18) can be written as

$$\frac{\mathrm{d}\boldsymbol{\rho}}{\mathrm{d}t} = \mathbf{M}\boldsymbol{\rho} \tag{4.20}$$

where $\boldsymbol{\rho} = \begin{pmatrix} \rho_{gg} & \rho_{gb} & \rho_{ga} & \rho_{bg} & \rho_{bb} & \rho_{ba} & \rho_{ag} & \rho_{ab} & \rho_{aa} \end{pmatrix}^{\mathrm{T}}$, and $\mathbf{M}$ is the 9×9 matrix

$$\begin{pmatrix} 0 & 0 & \frac{1}{2}\mathrm{i}\Omega_\alpha & 0 & \Gamma_{b\to g} & 0 & -\frac{1}{2}\mathrm{i}\Omega_\alpha & 0 & \Gamma_{a\to g} \\ 0 & -\mathrm{i}-\frac{1}{2}\Gamma_b & \frac{1}{2}\mathrm{i}\Omega_\beta & 0 & 0 & 0 & 0 & -\frac{1}{2}\mathrm{i}\Omega_\alpha & 0 \\ \frac{1}{2}\mathrm{i}\Omega_\alpha & \frac{1}{2}\mathrm{i}\Omega_\beta & -\mathrm{i}-\frac{1}{2}\Gamma_a & 0 & 0 & 0 & 0 & 0 & -\frac{1}{2}\mathrm{i}\Omega_\alpha \\ 0 & 0 & 0 & \mathrm{i}-\frac{1}{2}\Gamma_b & 0 & \frac{1}{2}\mathrm{i}\Omega_\alpha & -\frac{1}{2}\mathrm{i}\Omega_\beta & 0 & 0 \\ 0 & 0 & 0 & 0 & -\Gamma_b & \frac{1}{2}\mathrm{i}\Omega_\beta & 0 & -\frac{1}{2}\mathrm{i}\Omega_\beta & \Gamma_{a\to b} \\ 0 & 0 & 0 & \frac{1}{2}\mathrm{i}\Omega_\alpha & \frac{1}{2}\mathrm{i}\Omega_\beta & -\frac{1}{2}(\Gamma_a+\Gamma_b) & 0 & 0 & -\frac{1}{2}\mathrm{i}\Omega_\beta \\ -\frac{1}{2}\mathrm{i}\Omega_\alpha & 0 & 0 & -\frac{1}{2}\mathrm{i}\Omega_\beta & 0 & 0 & \mathrm{i}-\frac{1}{2}\Gamma_a & 0 & \frac{1}{2}\mathrm{i}\Omega_\alpha \\ 0 & -\frac{1}{2}\mathrm{i}\Omega_\alpha & 0 & 0 & -\frac{1}{2}\mathrm{i}\Omega_\beta & 0 & 0 & -\frac{1}{2}(\Gamma_a+\Gamma_b) & \frac{1}{2}\mathrm{i}\Omega_\beta \\ 0 & 0 & -\frac{1}{2}\mathrm{i}\Omega_\alpha & 0 & 0 & -\frac{1}{2}\mathrm{i}\Omega_\beta & \frac{1}{2}\mathrm{i}\Omega_\alpha & \frac{1}{2}\mathrm{i}\Omega_\beta & -\Gamma_a \end{pmatrix}.$$

The steady-state density matrix $\boldsymbol{\rho}^{\mathrm{ss}}$ can be straightforwardly obtained by finding the null space of the matrix $\mathbf{M}$. The average rate of increase of the x-component of the atomic kinetic energy due to momentum kicks from emitted photons is then

$$\frac{\mathrm{d}\langle E_x\rangle}{\mathrm{d}t} = \rho_{aa}^{\mathrm{ss}}\left(\Gamma_{a\to b}\, E_R^{(ab)}\beta_x^{(ab)} + \Gamma_{a\to g}\, E_R^{(ag)}\beta_x^{(ag)}\right) + \rho_{bb}^{\mathrm{ss}}\,\Gamma_{b\to g}\, E_R^{(bg)}\beta_x^{(bg)}, \qquad (4.21)$$

where $E_R^{(ij)} = \hbar^2 k_{ij}^2/(2m)$ with m the mass of the rubidium atom is the atomic recoil energy for the $i \to j$ transition, and $\beta_x^{(ij)}$ is a constant of order unity that accounts for the angular emission pattern of the $i \to j$ transition (see §B.3 of Appendix B). Analogous expressions hold for the average heating rate in the y- and z- directions.

4.3.3 Full level scheme: quantum trajectory simulations

In order to model the internal atomic dynamics beyond the three-level approximation, it is sufficient to work with a basis of states (n, ℓ, m) such that $\varepsilon_{n,\ell} \leq \max(\varepsilon_a, \varepsilon_b)$. For computational reasons, we further restrict this basis to contain only those states with $\ell \leq \ell_{\max}$. This truncation is physically justified by the observations of §2.1 that the ratio of $\ell \to \ell+1$ to $\ell \to \ell-1$ transitions decreases rapidly with increasing ℓ (see e.g. Figure 2.1). A radiative cascade from a state with $\ell = 0$ or $\ell = 1$ is thus very unlikely to visit any state with $\ell \gtrsim 5$, and we therefore see rapid convergence of our results to physically accurate values as $\ell_{\max}$ is increased.

The full atomic basis described above consists of many hundreds of levels, even for moderate values of n_a. This makes an exact solution of the master equation

Eq. (4.18) for the full level scheme computationally infeasible. However, the atomic dynamics can be efficiently simulated by means of quantum jump simulations [143, 144, 145, 146, 147]. To facilitate this, we note that Eq. (4.18) can be recast into the equivalent Lindblad form

$$\frac{\mathrm{d}\rho}{\mathrm{d}t} = \frac{1}{\mathrm{i}\hbar}\big[H,\rho\big] + \frac{1}{2}\sum_{(ij)}\Big(2c_{ij}\,\rho\,c_{ij}^{\dagger} - c_{ij}^{\dagger}c_{ij}\rho - \rho\,c_{ij}^{\dagger}c_{ij}\Big) \tag{4.22}$$

where $c_{ij} = \sqrt{\Gamma_{j\to i}}\,\sigma_{ij}$ is the collapse operator associated with the $j \to i$ decay channel, and the sum runs over all the allowed decay channels in the system. An algorithm for carrying out quantum jump simulations of a master equation in Lindblad form is given in Appendix C.

Method and parameters

We set $|a\rangle = |n_a, 1, 0\rangle$ and $|b\rangle = |n_b, 0, 0\rangle$, where n_a is in the range 6 – 40. A value of $\ell_{\max} = 7$ was used for the truncation of the atomic basis set. We carried out a total of $M = 1 \times 10^3$ trials on the interval $t = [0, t_{\max}]$, with $t_{\max} = 50$ ms. For each trial, we calculated the increase in the kinetic energy of the atom as follows. In the m^{th} trial, let n_m photons with wavevectors $\mathbf{k}_1, \ldots, \mathbf{k}_{n_m}$ be emitted. The corresponding change in the kinetic energy of the atom is

$$\Delta E^{(m)} = \Delta E_x^{(m)} + \Delta E_y^{(m)} + \Delta E_z^{(m)} \tag{4.23}$$

where

$$\Delta E_x^{(m)} = \frac{1}{2m}\Big[\,(\mathbf{p}_f\cdot\hat{\mathbf{e}}_x)^2 - (\mathbf{p}_i\cdot\hat{\mathbf{e}}_x)^2\,\Big], \tag{4.24}$$

together with the analogous expressions obtained by replacing x by y or z. Here $\mathbf{p}_i$ and $\mathbf{p}_f = \mathbf{p}_i - \hbar\sum_{i=1}^{n_m}\mathbf{k}_i$ denote the initial and final atomic momenta; without loss of generality we set $\mathbf{p}_i = 0$. The average rate of increase of the kinetic energy in the x-direction over all M Monte Carlo trials is then given by

$$R_x = \frac{1}{Mt_{\max}}\sum_{m=1}^{M}\Delta E_x^{(m)}, \tag{4.25}$$

with analogous expressions holding for y and z. As a result of the dipolar emission patterns, the in-plane (x, y) and out-of-plane (z) heating rates differ slightly.

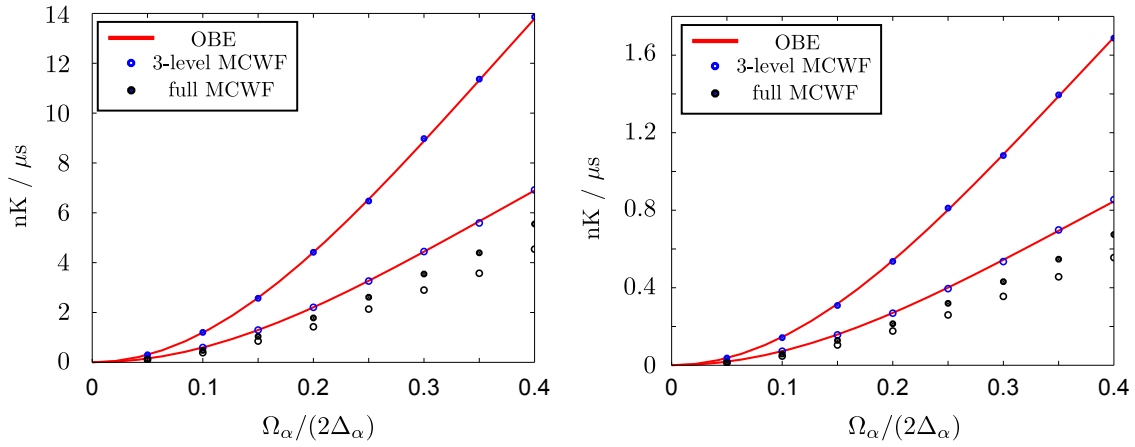

(a) $n_a = 15$ (b) $n_a = 28$

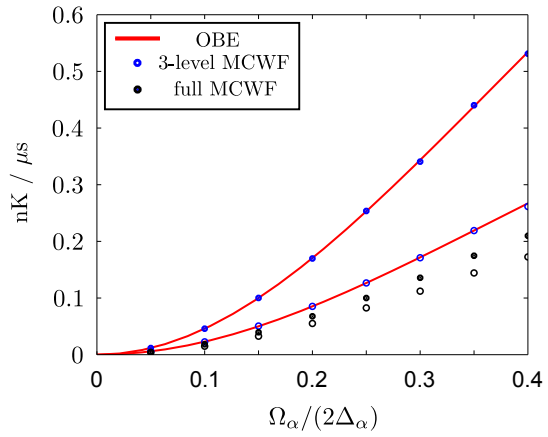

(c) $n_a = 40$

Figure 4.8: The heating rate due to photon recoil for the dressing scheme of Figure 4.6 as a function of Ω_α for $(\Omega_\beta, \Delta_\alpha) = 2\pi \times (150, 300)$ MHz. The atomic states involved in the dressing scheme are $|a\rangle = |n_a, 1, 0\rangle, |b\rangle = |n_a, 0, 0\rangle$: (a) $n_a = 15$, (b) $n_a = 28$, and (c) $n_a = 40$. In each plot, the red line represents the result obtained from the exact numerical solution of the three-level approximation, while circles mark the result obtained from quantum trajectory simulations of the master equation within the three-level approximation (blue) and in the full level scheme (black). Filled circles denote the rate of heating in the x-y plane, while empty circles denote the heating rate in the z-direction.

4.3.4 Results

The rates of motional heating due to photon recoil for $(\Omega_\beta, \Delta_\alpha) = 2\pi \times (150, 300)$ MHz as a function of Ω_α for three different values of n_a are illustrated in Figure 4.8. Each plot contains results for the rate of heating along each of the x, y and z axes, both within the three-level approximation and for the full level scheme. The results for the full level scheme were obtained by quantum trajectory calculations following the algorithm described in Appendix C, while the results within the three-level approximation were obtained in two ways: firstly, by directly computing the steady-state solution to the master equation Eq. (4.18) and obtaining the heating rate through Eq. (4.21); and secondly, by carrying out a quantum trajectory simulation of Eq. (4.18) restricted to the driven subspace $\mathcal{P}$. The results obtained by the different methods show excellent agreement with one another, which serves to validate the quantum trajectory treatment used.

Figure 4.8 indicates that the typical rate of heating arising from spontaneous emission in the dressing scheme of outlined in Section §4.2.2 is of the order of a few nanoKelvin per microsecond. The rate of heating in the x-y plane is higher than that in the z-direction, due to the preferential in-plane emission arising from the dipole emission profile. The rate of recoil heating in all three dimensions increases with increasing Ω_α, since the excited states $|a\rangle$ and $|b\rangle$ are more strongly populated, leading to a higher spontaneous emission rate. Conversely, the heating rate decreases with increasing n_a, in accordance with the longer radiative lifetimes and lower spontaneous emission rates of Rydberg states with higher principal quantum numbers.

We can now make a direct comparison between the predicted heating rate both with and without the three-level approximation. From Figure 4.8, we see that the rate of heating in the full level scheme is significantly the lower of the two: in the x-y plane (z-direction) the rate is 40% (65%) of that predicted by the 3-level approximation. These figures are essentially constant for all $n_a \geq 12$. This is a direct consequence of the fact that within the full level scheme, the atom typically decays to the ground state via a radiative cascade, rather than by a single photon (see Figure 2.3). The emission of a sequence of photons with wavevectors $\mathbf{k}_1, \mathbf{k}_2, \ldots$ whose magnitudes sum to k_{ag} results in a smaller average increase in kinetic energy than the emission of a single photon with wavevector magnitude k_{ag}.

4.4 Stability of crystals of Rydberg-dressed atoms

In §4.1.5 we found that the melting temperature of mesoscopic crystals of dipolar atoms is likely to be less than 100 nK for realistic experimental parameters. As can be seen from the emission spectra in Figure 2.3, this is lower than the recoil energy associated with nearly all of the photons that can be emitted in a decay event from the excited states $|a\rangle$ or $|b\rangle$ for the values of n_a considered here. This indicates that recoil heating associated with spontaneous emission from the excited component of the dressed ground state is likely to threaten the stability of mesoscopic crystals formed by Rydberg-dressed atoms. However, this is not necessarily a fatal blow to creating such crystals, since the stability of a crystal consisting of $N \gg 1$ atoms will depend to a large extent on how the atomic recoil energy of a single spontaneous emission event is distributed among the atoms. If the motion of neighbouring atoms is strongly coupled, so that the recoil energy is shared widely among many atoms, then the average heating rate calculated in §4.3 is relevant, and the crystal might be expected to have a lifetime ranging up to several hundreds of microseconds, depending on the exact dressing parameters used. On the other hand, if the motion of neighbouring atoms is only weakly coupled, the hot single atom could be expected to exit rapidly from the neighbourhood of the crystal. The relative importance of each of these scenarios could be investigated by performing a molecular dynamics simulation of the atomic motion simultaneously with a quantum trajectory simulation of the cascade process. Another interesting avenue is the possibility of stabilising the crystal through active laser cooling of the Rydberg-dressed atoms, as recently proposed and investigated in [134].

4.5 Summary

We studied the equilibrium structures of mesoscopic ($6 \leq N \leq 40$) clusters of dipolar particles, and found that for small values of N, the cluster consists of a regular collection of polygonal shells. Defects in the shell structure begin to appear as the size of the cluster is increased past $N \gtrsim 20$, and for $N \gtrsim 30$ the shell structure gives way to a regular triangular lattice. We investigated the melting behaviour of these clusters through Monte Carlo simulations, and found that the onset of melting for realistic experimental parameters takes place at temperatures of 25 – 75 nK, though remnants of crystalline order are expected to be observable at higher temperatures.

We outlined two possible schemes by which the exaggerated electric dipole moment of an excited Rydberg state could be exploited to induce a non-zero electric dipole moment in a neutral atom. In one scheme, a DC electric field is applied to the atom, and the ground state is weakly coupled to an extremal state in the 'Stark fan' of levels produced from each Rydberg manifold. In the other scheme, an AC dressing field is used to couple two excited Rydberg states, thereby forming a pair of dressed states which have rapidly-oscillating electric dipole moments. One such dressed state is weakly coupled into the ground state by an admixing laser.

We then investigated the rate of atomic heating due to spontaneous emission in the AC dressing scheme for two treatments of the atomic level structure. By using quantum trajectory simulations of the master equation governing the dynamics of the atomic density matrix, we made a quantitative comparison of the heating rate predicted by a reduced three-level approximation, as compared with a full treatment of the atomic level structure. We found that the heating rate predicted within the full level scheme is approximately half of that predicted by the three-level approximation, due to the high probability of the atom returning to the ground state by a radiative cascade rather than through a single photon emission.

Chapter 5

Uniquely decomposing walks on directed graphs

In the first three chapters of this thesis, we used quantum defect theory as a tool to study several different proposals involving cold Rydberg atoms. We began by calculating the radiative cascade behaviour of single Rydberg atoms, then investigated the stability of diatomic molecular Rydberg states, before analysing classical crystalline structures comprising several dozen atoms. In keeping with this progression in system size, we now introduce a novel method of evaluating matrix functions which promises to provide a useful tool for simulating the quantum dynamics of systems of many hundreds or even thousands of cold Rydberg atoms.

Large systems of Rydberg atoms currently from an active and fertile topic of research within cold matter physics, since they exhibit a rich range of physics due to the dipolar interactions between Rydberg states. Because these dipolar interactions are both strong and long-range, many-body effects play an important role in determining the physical behaviour of such systems, so that standard perturbative approaches are not suitable for their analysis. Further, although standard techniques such as DMRG have achieved great success for strongly-correlated one-dimensional systems, the simulation of two- and three-dimensional systems with long-range interactions remains a difficult problem.

Motivated by this, we now develop a novel technique for symbolically evaluating matrix functions in closed form. This method, which we term the method of path-sums, is based on two main concepts: firstly, a mapping between matrix multiplications and walks on weighted directed graphs, and secondly, a universal

result on the structure of such walks. We expect that applying the method of path-sums to the evaluation of the time-evolution operator $\mathsf{U}(t) = \exp(-\mathrm{i}\mathsf{H}t/\hbar)$ will form a promising new approach to the simulation of large systems of Rydberg atoms.

We present the method of path sums over the next two chapters. In the current chapter, we state and prove the graph-theoretic result that forms the foundation for the path-sum method. This result amounts to a universal statement about the structure of walks on a directed graph: specifically, that any walk on an arbitrary directed graph can be decomposed into a simple path plus a collection of recursively-nested simple cycles. In Chapter 6, we develop the method of path-sums by combining this graph-theoretic result with the aforementioned mapping between matrix multiplications and walks on directed graphs.

The current chapter is structured as follows. We begin by providing an overview of the main concepts of graph theory in §5.1, which serves to establish our terminology and notation. We then present and prove the main results of the chapter in §5.2 and §5.3. In §5.4 we present two illustrative examples of how these results can be applied, by obtaining a continued-fraction representation of the walk-generating function of a graph and a novel recursive formula for the quasideterminants of a matrix. We summarise our results in §5.5.

The work appearing in this chapter was carried out in collaboration with Pierre-Louis Giscard. The results of §5.2 and §5.3 are due to the present author, while the illustrative applications of §5.4 were developed in collaboration with Pierre-Louis Giscard. The results presented here form the basis for a publication that has recently been submitted to the *SIAM Journal on Discrete Mathematics*; a preprint of this manuscript, which also includes a number of new developments, has recently been made available [148].

5.1 A review of graph theory

A graph is a mathematical structure consisting of a set of vertices joined by a collection of edges. In addition to their intrinsic mathematical interest, graphs are useful for providing abstract representations of relationships among sets of objects. Graph theory therefore finds many applications within science, mathematics, and engineering: vertices and edges may be used to represent anything from software packages and the dependencies between them, to the system states and possible transitions of a discrete-state Markov chain, to an ensemble of vector spaces and a

collection of linear mappings linking them.

In this section we summarise some concepts in graph theory in order to establish our terminology and notation. In general we follow standard graph theory references such as [149, 150].

5.1.1 Graphs

A directed graph $\mathcal{G}$ is a pair of sets $(\mathcal{V}, \mathcal{E})$ such that the elements of the *edge set* $\mathcal{E}$ are ordered pairs of elements of the *vertex set* $\mathcal{V}$. A graph is *infinite* if it has infinitely many edges, vertices, or both; or *finite* otherwise. An edge connecting a vertex to itself will be called a *loop*, and two or more edges that connect the same two vertices in the same direction are called *multiple edges*. Throughout this thesis we consider finite directed graphs that may contain loops, but not multiple edges. We denote the vertices of $\mathcal{G}$ by Greek letters $\alpha, \beta, \ldots$, and an edge that leads from vertex μ to vertex ν by $(\mu\nu)$. Further, we denote the graph obtained by deleting all loops from $\mathcal{G}$ by $\mathcal{G}_0$, and the graph obtained by deleting vertices $\alpha, \beta, \ldots$ from $\mathcal{G}$ by $\mathcal{G}\backslash\{\alpha, \beta, \ldots\}$.

A convenient representation of a graph $\mathcal{G}$ is its adjacency matrix $\mathsf{A}_\mathcal{G}$, the square matrix of size $|\mathcal{V}|$ with entries

$$\mathsf{A}_\mathcal{G}[\mu, \nu] = \begin{cases} 1 & \text{if the edge } (\mu\nu) \text{ exists in } \mathcal{G}, \\ 0 & \text{otherwise.} \end{cases} \tag{5.1}$$

5.1.2 Walks

A *walk* w of length n from α to ω is a sequence of n contiguous edges $(\alpha\mu_2), (\mu_2\mu_3), \ldots, (\mu_n\omega)$. If it happens that $\omega = \alpha$, then w is a *closed walk*; walks that are not closed are *open*. We will typically represent a walk either by its edge sequence $(\alpha\mu_2)(\mu_2\mu_3)\cdots(\mu_n\omega)$ or by its vertex string $(\alpha\mu_2\mu_3\cdots\mu_n\omega)$. The head and tail vertices of w are $h(w) = \alpha \equiv \mu_1$ and $t(w) = \omega \equiv \mu_{n+1}$, respectively; the remaining vertices $\mu_2, \ldots, \mu_n$ are the *internal vertices* of w. In addition to walks of positive length, we define for every vertex $\mu \in \mathcal{V}$ a *trivial walk* of length zero, which we will denote by (μ). When convenient, these trivial walks may be inserted into the edge sequence of a longer walk: thus $(\alpha\mu_2)(\mu_2\omega)$ and $(\alpha)(\alpha\mu_2)(\mu_2)(\mu_2\omega)(\omega)$ represent the same walk of length 2 from α to ω. The set of all walks from α to ω on $\mathcal{G}$ will be denoted by $W_{\mathcal{G};\alpha\omega}$.

5.1.3 Paths

The terms *path* and *simple path* will be used interchangeably to refer to a walk whose vertices are all distinct. The set of all paths from α to ω on $\mathcal{G}$ will be denoted by $P_{\mathcal{G};\alpha\omega}$. Since $\mathcal{G}$ is finite, this set is finite.

5.1.4 Cycles

A *cycle* off α is a walk that starts and finishes on α, but does not revisit α in between. Every cycle is a closed walk, but not every closed walk is a cycle. A cycle will be called a *simple cycle* if it visits each of its internal vertices only once. A simple cycle is necessarily a *loop* if it is of length 1, or a triangle, square, ... if it is of length $3, 4, \ldots$, and will be called a *backtrack* if it is of length 2. The set of all cycles off α on $\mathcal{G}$ will be denoted by $\tilde{C}_{\mathcal{G};\alpha}$. The set of all simple cycles off α on $\mathcal{G}$ will be denoted by $C_{\mathcal{G};\alpha}$; since $\mathcal{G}$ is finite, this set is finite.

5.1.5 Concatenating walks

Given a pair of walks w_1, w_2 that satisfy $h(w_2) = t(w_1)$, we define their concatenation $w_1 w_2$ to be the walk obtained by concatenating their edge sequences. We extend this operation to sets of walks as follows: given two walk sets W_1 and W_2 such that $h(w_2) = t(w_1)$ for every $w_1 \in W_1$ and $w_2 \in W_2$, the set $W_1 \circ W_2$ is defined as

$$W_1 \circ W_2 = \{w_1 w_2 : w_1 \in W_1, w_2 \in W_2\}. \tag{5.2}$$

It follows that a set of closed walks may be concatenated with itself. Given a set W of closed walks off μ, we define $W^0 = \{(\mu)\}$ and $W^n = W^{n-1} \circ W$ for $n \in \{1, 2, \ldots\}$. Finally, we define the Kleene star W^* of a set W of closed walks to be the set of walks formed by concatenating any number of elements of W:

$$W^* = \bigcup_{n=0}^{\infty} W^n. \tag{5.3}$$

5.1.6 Nesting walks

Let $w_1 = (\beta\mu_2 \cdots \mu_m\beta)$ be a closed walk of length m off β, and let $w_2 = (\alpha\eta_2 \cdots \beta \cdots \eta_n\omega)$ be a walk of length n that has β as precisely one vertex. Then the walk of length $m + n$ formed by replacing β by w_1 in the vertex string of w_2 will be said to

consist of w_1 *nested into* w_2 (off the vertex β). This walk has vertex sequence $(\alpha\eta_2\cdots\beta\mu_2\cdots\mu_m\beta\cdots\eta_n\omega)$.

5.1.7 The walk algebra $K\mathcal{G}$

Let K be a field. Then the *walk algebra* or *path algebra* $K\mathcal{G}$ is the vector space over K with basis $B_{K\mathcal{G}}$ given by the set of all walks on $\mathcal{G}$:

$$B_{K\mathcal{G}} = \bigcup_{\alpha,\omega\in\mathcal{V}} W_{\mathcal{G};\alpha\omega}. \tag{5.4}$$

The dimension of $K\mathcal{G}$ is infinite if $\mathcal{G}$ contains any cycles.

5.1.8 Weighted graphs

A *weighted graph* is formed by pairing a graph $\mathcal{G}$ with a weight function φ that assigns a weight $\varphi[e]$ to each edge $e \in \mathcal{E}$. To retain maximum generality, we let the weight of an edge from μ to ν be any invertible morphism from an object V_μ, associated with the vertex μ, to an object V_ν, associated with the vertex ν. We extend the domain of φ from the edge set $\mathcal{E}$ to the walk algebra $K\mathcal{G}$ by setting $\varphi[(\mu)] = \mathrm{Id}_\mu$, the identity morphism on V_μ, and defining

$$\varphi[we] = \varphi[e]\varphi[w] \tag{5.5a}$$

for any walk w and edge e satisfying $h(e) = t(w)$, and

$$\varphi[w_i + w_j] = \varphi[w_i] + \varphi[w_j] \tag{5.5b}$$

for walks w_i, w_j satisfying $h(w_i) = h(w_j)$ and $t(w_i) = t(w_j)$. Note that the ordering of weights when two edges are concatenated is suitable for the composition of morphisms to be carried out.

5.2 The path decomposition of a walk

We now present the central result of this chapter: that any walk on a graph $\mathcal{G}$ can be decomposed into a collection of concatenated and recursively-nested simple cycles nested into an underlying simple path. This result is valid for directed graphs either with or without self-loops. This decomposition, which we refer to as

the path decomposition of a walk, is carried out in a fashion that natively respects the ordering of the edges in the walk.

An intuitive way of understanding the path decomposition of a walk w is as follows. Consider traversing w from start to finish, pausing at each vertex to check whether or not it has been visited previously. Upon arriving at a vertex μ that has been visited previously, remove from w the sequence of edges traversed since the most recent encounter with μ, and set this sequence aside. Proceed in this fashion until the end of w is reached. At this point, the remaining vertex string contains no repeated elements, and so defines a simple path. Further, each of the removed sections of w contains no repeated internal vertices, and so defines a simple cycle off the relevant vertex μ.

By following this procedure, any walk can be decomposed into a simple path and a collection of simple cycles. Further, the original walk can be reconstructed by nesting and concatenating the simple cycles and simple path together. Walks and path decompositions are therefore in one-to-one correspondence. The remainder of this section is dedicated to formalising and proving this statement, and showing that this one-to-one correspondence can be used to write the basis of the path algebra $K\mathcal{G}$ in a compact form.

5.2.1 Description and definition

The path decomposition of a walk w is an ordered tree T_w such that

(i) the root node of T_w contains a simple path p, and has $\ell + 1$ children, where ℓ is the length of p;

(ii) each child node of T_w contains an ordered sequence $c_1 c_2 \cdots c_k$ of $k \geq 0$ simple cycles, and has $m_1 + m_2 + \cdots + m_k - k$ children, where m_i is the length of c_i. If $k = 0$ then the child node is empty, in which case it functions as a placeholder to maintain the positions of the children to its right;

(iii) collapsing T_w produces the walk w. To collapse the tree T_w, start at the leaf nodes and work upwards until the root is reached. At each node N, collapse the children of N into N by nesting the contents of the i^{th} child either off the i^{th} internal vertex of the cycles in N (counting across cycle boundaries), if N is a child node of T_w; or off the i^{th} vertex of the simple path p, if N is the root node of T_w.

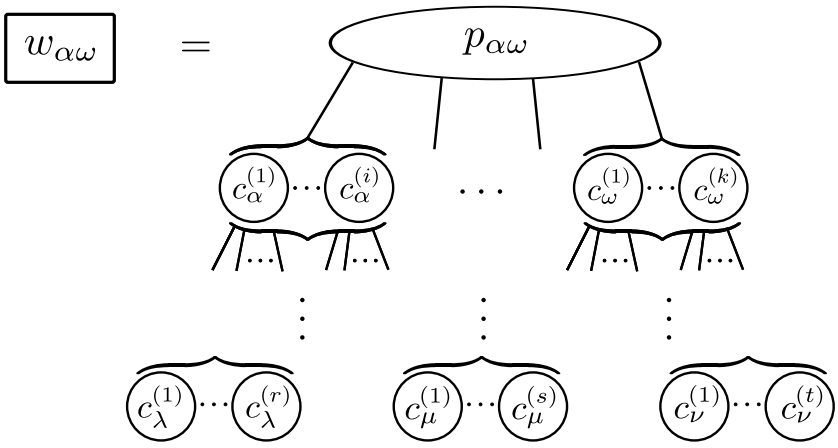

Figure 5.1: An illustration of the structure of a path decomposition of a walk $w_{\alpha\omega}$ from α to ω. Each of the children of a given node N contains a sequence of concatenated simple cycles that are nested into the contents of the node N. Here i, k, r, s, and t are non-negative integers denoting the number of simple cycles in a particular concatenated sequence.

Figure 5.1 provides an illustration of the structure of a path decomposition.

Two points are worth noting. Firstly, every walk admits at least one path decomposition. This can be seen by considering the intuitive decomposition procedure described in the introduction to §5.2, which sequentially extracts simple cycles from a walk until only a simple path remains. By noting the order in which the cycles are extracted during this process, the tree T_w can be constructed (starting at the leaf nodes, and working upwards) as the decomposition proceeds. Secondly, many walks admit more than one path decomposition. To avoid ambiguity in these cases, we adopt the convention that the *standard* or *canonical* path decomposition of a walk is the one that places all child nodes as far towards the left of the tree as possible. This corresponds to nesting each simple cycle off as early a vertex as possible. An example is given in Figure 5.2.

5.2.2 Decomposing the basis of the path algebra $K\mathcal{G}$

Having formalised the structure of a canonical path decomposition, we now establish the one-to-one correspondence between walks and canonical path decompositions. We achieve this by providing a constructive step-by-step procedure that builds T_w by starting at the root node and working downwards (i.e. the path p is first isolated, then each branch is constructed). This procedure differs from the

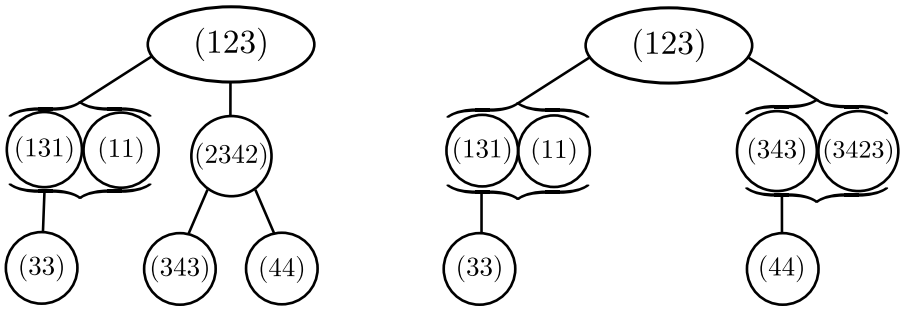

Figure 5.2: Two different path decompositions of the walk $w = (1331123434423)$. The left-hand decomposition is the canonical decomposition for this walk.

decomposition method described earlier, which builds the tree by starting at the leaf nodes and working upwards. In either case, the final tree is the same; however, the top-down decomposition procedure lends itself more readily to a recursive implementation, which we find convenient here.

As a consequence of the one-to-one correspondence between walks and path decompositions, the set of all walks on $\mathcal{G}$ can be constructed by taking the union of all possible path decompositions. This leads us to a compact expression for the basis of the path algebra $K\mathcal{G}$. We state the result as follows:

Theorem 5.2.1. *The set of all walks from α to ω on a graph $\mathcal{G}$ can be written as*

$$W_{\mathcal{G};\alpha\omega} = \bigcup_{P_{\mathcal{G};\alpha\omega}} \tilde{C}^*_{\mathcal{G};\alpha} \circ \big\{(\alpha\nu_2)\big\} \circ \tilde{C}^*_{\mathcal{G}\setminus\{\alpha\};\nu_2} \circ \cdots \circ \big\{(\nu_\ell\omega)\big\} \circ \tilde{C}^*_{\mathcal{G}\setminus\{\alpha,\nu_2,\ldots,\nu_\ell\};\omega} \tag{5.6a}$$

where ℓ is the length of the simple path $(\alpha\nu_2\cdots\nu_\ell\omega) \in P_{\mathcal{G};\alpha\omega}$, and the cycle set $\tilde{C}_{\mathcal{G};\alpha}$ is

$$\tilde{C}_{\mathcal{G};\alpha} = \bigcup_{C_{\mathcal{G};\alpha}} \big\{(\alpha\eta_2)\big\} \circ \tilde{C}^*_{\mathcal{G}\setminus\{\alpha\};\eta_2} \circ \big\{(\eta_2\eta_3)\big\} \circ \cdots \circ \tilde{C}^*_{\mathcal{G}\setminus\{\alpha,\eta_2,\ldots,\eta_{m-1}\};\eta_m} \circ \big\{(\eta_m\alpha)\big\}, \tag{5.6b}$$

where m is the length of the simple cycle $(\alpha\eta_2\cdots\eta_m\alpha) \in C_{\mathcal{G};\alpha}$. The basis for the walk algebra $K\mathcal{G}$ can therefore be written as

$$B_{K\mathcal{G}} = \bigcup_{\alpha,\omega} \bigcup_{P_{\mathcal{G};\alpha\omega}} \tilde{C}^*_{\mathcal{G};\alpha} \circ \big\{(\alpha\nu_2)\big\} \circ \tilde{C}^*_{\mathcal{G}\setminus\{\alpha\};\nu_2} \circ \cdots \circ \big\{(\nu_\ell\omega)\big\} \circ \tilde{C}^*_{\mathcal{G}\setminus\{\alpha,\nu_2,\ldots,\nu_\ell\};\omega}. \tag{5.6c}$$

Proof. We prove Theorem 5.2.1 by providing a step-by-step procedure for con-

structing the canonical path decomposition of an arbitrary walk. This procedure serves to establish two points: firstly, it demonstrates the one-to-one correspondence between walks and canonical path decompositions; and secondly, it shows that the structure of a canonical path decomposition matches the structure of an element of the set on the right-hand side of Theorem 5.2.1: that is, that the form of a canonical path decomposition mandates the sequential removal of vertices from $\mathcal{G}$ seen in Eq. (5.6a) and (5.6b).

The step-by-step procedure for constructing a canonical path decomposition consists of three parts, each of which we state as a Lemma. We show firstly that any walk can be decomposed into a path p and a collection of closed walks nested off the vertices of p (Lemma 5.2.2); secondly, that any closed walk is a concatenated sequence of cycles (Lemma 5.2.3); and thirdly, that any cycle can be decomposed into a simple cycle c and a collection of closed walks nested off the internal vertices of c (Lemma 5.2.4).

Lemma 5.2.2. *The set of all walks from α to ω on $\mathcal{G}$ can be written as*

$$W_{\mathcal{G};\alpha\omega} = \bigcup_{P_{\mathcal{G};\alpha\omega}} W_{\mathcal{G};\alpha\alpha} \circ \big\{(\alpha\nu_2)\big\} \circ W_{\mathcal{G}\setminus\{\alpha\};\nu_2\nu_2} \circ \cdots \big\{(\nu_\ell\omega)\big\} \circ W_{\mathcal{G}\setminus\{\alpha,\nu_2,\ldots,\nu_\ell\};\omega\omega}, \quad (5.7)$$

where ℓ is the length of the path $(\alpha\nu_2\cdots\nu_\ell\omega) \in P_{\mathcal{G};\alpha\omega}$.

Proof. The following procedure uniquely decomposes an arbitrary walk into a path and a collection of closed walks. Let $(\alpha\mu_2)(\mu_2\mu_3)\cdots(\mu_n\alpha)$ be the edge sequence of w, and consider traversing this sequence from start to finish. Upon arriving at a vertex ν, remove from w the sequence of edges joining the current appearance of ν to the final appearance of ν. In other words, extract from w the longest possible closed walk off ν (if ν only appears once, extract the trivial closed walk (ν)). Setting this closed walk aside, continue along the remaining edges. By the time the end vertex ω is reached, the surviving edges define a simple path $p = (\alpha\nu_2\cdots\nu_\ell\omega)$, with a length we denote by ℓ. A total of $\ell+1$ closed walks have been set aside, the i^{th} of which starts and finishes on ν_i and does not visit any of the vertices $\alpha, \nu_2, \ldots \nu_{i-1}$. The original walk w is unambiguously reconstructed by nesting each of the extracted closed walks off the appropriate vertex of p. This procedure therefore provides a one-to-one mapping from walks to paths and closed walks. This mapping, which is represented symbolically in Fig. 5.3(a), directly implies Eq. (5.7). ■

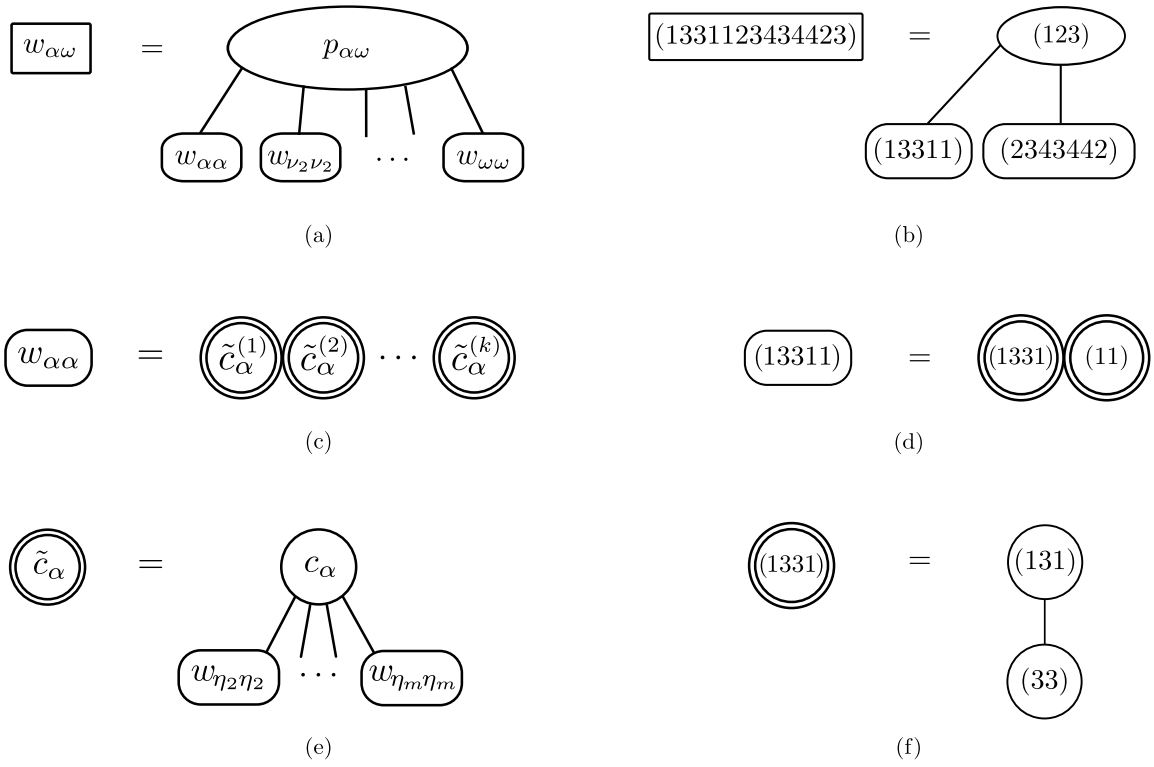

Figure 5.3: Symbolic representations of the decompositions described in Lemmas 5.2.2–5.2.4 (left), together with an example of each decomposition (right). Ovals represent simple paths; rectangles (rounded rectangles) represent walks (closed walks); double circles represent cycles; single circles represent simple cycles. (a)-(b) Lemma 5.2.2: a walk can be decomposed into a path p and a collection of closed walks nested off the vertices of p; (c)-(d) Lemma 5.2.3: a closed walk can be decomposed into a sequence of concatenated cycles; (e)-(f) Lemma 5.2.4: a cycle can be decomposed into a simple cycle c and a collection of closed walks nested off the internal vertices of c.

Lemma 5.2.3. *The set of all closed walks off α on $\mathcal{G}$ can be written as*

$$W_{\mathcal{G};\alpha\alpha} = \tilde{C}^*_{\mathcal{G};\alpha}, \tag{5.8}$$

Proof. A closed walk can be decomposed into cycles as follows. We define the trivial walk (α) to consist of zero cycles. Otherwise, let $n \geq 0$ be the number of times that α appears as an internal vertex of w. Then w consists of $n+1$ cycles, which are identified by splitting the edge sequence of w at each internal appearance of α. If the $n+1$ cycles are stored as an ordered list, the original closed walk is

recovered by concatenating the cycles in the appropriate order. This mapping, which is represented symbolically in Fig. 5.3(c), directly implies Eq. (5.8). ■

Lemma 5.2.4. *The set of all cycles off α on $\mathcal{G}$ can be written as*

$$\tilde{C}_{\mathcal{G};\alpha} = \bigcup_{C_{\mathcal{G};\alpha}} \big\{(\alpha\eta_2)\big\} \circ W_{\mathcal{G}\setminus\{\alpha\};\eta_2\eta_2} \circ \big\{(\eta_2\eta_3)\big\} \circ \cdots \circ W_{\mathcal{G}\setminus\{\alpha,\eta_2,\ldots,\eta_{m-1}\};\eta_m\eta_m} \circ \big\{(\eta_m\alpha)\big\} \tag{5.9a}$$

$$= \bigcup_{C_{\mathcal{G};\alpha}} \big\{(\alpha\eta_2)\big\} \circ \tilde{C}^*_{\mathcal{G}\setminus\{\alpha\};\eta_2} \circ \big\{(\eta_2\eta_3)\big\} \circ \cdots \circ \tilde{C}^*_{\mathcal{G}\setminus\{\alpha,\eta_2,\ldots,\eta_{m-1}\};\eta_m} \circ \big\{(\eta_m\alpha)\big\}, \tag{5.9b}$$

where m is the length of the simple cycle $(\alpha\eta_2\cdots\eta_m\alpha) \in C_{\mathcal{G};\alpha}$.

Proof. The following procedure uniquely decomposes a cycle into a simple cycle and a collection of closed walks. Let $(\alpha\mu_2)(\mu_2\mu_3)\cdots(\mu_n\alpha)$ be the edge sequence of $\tilde{c}_\alpha$. Then $\tilde{c}$ can be decomposed into a simple cycle and a collection of closed walks by an essentially identical method to that described in the proof to Lemma 5.2.2: the only difference is that the traversal should not start at α, but rather at the first internal vertex μ_2. Upon reaching the end of the cycle, the remaining edge sequence defines a simple cycle $c = (\alpha\eta_2)(\eta_2\eta_3)\cdots(\eta_m\alpha)$ of length $m \leq n$, and a total of $m-1$ closed walks have been set aside. The i^{th} closed walk starts and finishes on η_{i+1}, and does not visit any of the vertices $\alpha, \eta_2, \ldots, \eta_i$. The cycle $\tilde{c}$ is reconstructed by nesting each of the closed walks off the appropriate internal vertex of c. This mapping, which is represented symbolically in Fig. 5.3(e), directly implies Eq. (5.9a). Equation (5.9b) then follows on using the result of Lemma 5.2.3. ■

Taken together, the results of Lemmas 5.2.2–5.2.4 lead to the result of Theorem 5.2.1. Given a walk w, consider applying Lemma 5.2.2 to decompose w into a path p and a collection of closed walks, then repeatedly applying Lemmas 5.2.3 and 5.2.4 to each closed walk thus produced. This procedure converts each closed walk into a sequence of simple cycles, each of which has a concatenated sequence of recursively-nested simple cycles nested off each internal vertex. Since one or more vertices are deleted from the graph with each increase in the level of nesting (see Lemma 5.2.4), the recursive decomposition of closed walks into sequences of nested simple cycles is guaranteed to eventually terminate. At this point the canonical path decomposition of w has been obtained. ■

The decomposition of a walk into a simple path and a collection of simple cycles bears many similarities to the decomposition of an integer into a product

of prime numbers [151]. In each case, a composite object is decomposed into a collection of simpler objects, which are fundamental in the sense that they cannot themselves be decomposed any further. Within this analogy, our simple paths and simple cycles play the role of the prime numbers, and our unique 'canonical path decomposition' of a walk is analogous to the unique 'standard form' of an integer, in which the prime factors are written in increasing order. Theorem 5.2.1 then mirrors the Fundamental Theorem of Arithmetic.

5.3 The sum of all walks on a graph

The results of the previous section give a detailed understanding of the structure of walks on $\mathcal{G}$. We now use these results to recast the sum of all walks linking a given pair of vertices on $\mathcal{G}$ into a compact form consisting of a finite number of terms. Specifically, by using the fact that every walk on a graph can be decomposed into a simple path and a collection of concatenated and nested simple cycles (Theorem 5.2.1), we rewrite the sum of all walks from α to ω on $\mathcal{G}$ as a sum over simple paths from α to ω by modifying each simple path to include all possible collections of concatenated and nested simple cycles off the vertices it visits. This modification amounts to replacing each vertex μ in a path by a 'dressed vertex' $(\mu)'_{\mathcal{G}}$ that includes all possible concatenations and nestings of simple cycles off μ. We then formally resum each of the sums of simple cycles into a closed form, thereby obtaining a compact expression for the sum of all walks from α to ω on $\mathcal{G}$.

This section consists of two parts. In the first we recast the sum of all walks from α to ω as a sum over paths with dressed vertices. This result represents a general formal statement on the sum of the elements of the walk set $W_{\mathcal{G};\alpha\omega}$. In the second part we extend the result from the sum of walks on $\mathcal{G}$ to the sum of the weights of all walks from α to ω on the weighted graph $(\mathcal{G}, \varphi)$. Since the weight of each walk from α to ω is a morphism from V_α to V_ω (for example, a linear mapping between vector spaces), the sum of walk weights is a morphism equal to the sum of all the individual morphisms.

5.3.1 The sum of walks on a directed graph

Given a graph $\mathcal{G}$ and a pair of vertices α, ω, we denote the sum of all walks from α to ω on $\mathcal{G}$ by $\Sigma_{\mathcal{G};\alpha\omega}$:

$$\Sigma_{\mathcal{G};\alpha\omega} = \sum_{W_{\mathcal{G};\alpha\omega}} (\alpha\eta_2)\,(\eta_2\eta_3)\cdots(\eta_n\omega)\,. \tag{5.10}$$

where n is the length of the walk $(\alpha\eta_2\cdots\eta_n\omega) \in W_{\mathcal{G};\alpha\omega}$. In this section we use the result of Theorem 5.2.1 to write $\Sigma_{\mathcal{G};\alpha\omega}$ in a compact closed form.

Theorem 5.3.1. *The sum of all walks from α to ω on $\mathcal{G}$ is given by*

$$\Sigma_{\mathcal{G};\alpha\omega} = \sum_{P_{\mathcal{G};\alpha\omega}} (\alpha)'_{\mathcal{G}}\,(\alpha\nu_2)\,(\nu_2)'_{\mathcal{G}\setminus\{\alpha\}}\cdots(\nu_\ell\omega)\,(\omega)'_{\mathcal{G}\setminus\{\alpha,\nu_2,\ldots,\nu_\ell\}}\,, \tag{5.11a}$$

where ℓ is the length of the path $(\alpha\nu_2\cdots\nu_\ell\omega) \in P_{\mathcal{G};\alpha\omega}$, and $(\alpha)'_{\mathcal{G}} = \Sigma_{\mathcal{G};\alpha\alpha}$ denotes the vertex α dressed on $\mathcal{G}$, which is equal to

$$(\alpha)'_{\mathcal{G}} = \left[(\alpha) - \sum_{C_{\mathcal{G};\alpha}} (\alpha)\,(\alpha\mu_2)\,(\mu_2)'_{\mathcal{G}\setminus\{\alpha\}}\,(\mu_2\mu_3)\cdots(\mu_m)'_{\mathcal{G}\setminus\{\alpha,\mu_2,\ldots,\mu_{m-1}\}}\,(\mu_m\alpha)\,(\alpha)\right]^{-1}, \tag{5.11b}$$

where m is the length of the simple cycle $(\alpha\mu_2\cdots\mu_m\alpha) \in C_{\mathcal{G};\alpha}$, and $\big[(\alpha) - \sum_{C_{\mathcal{G}_\alpha}}(\alpha)(\alpha\mu_2)\cdots(\alpha)\big]^{-1}$ is the formal power series $\sum_{p=0}^{\infty}\big[\sum_{C_{\mathcal{G}_\alpha}}(\alpha)(\alpha\mu_2)\cdots(\alpha)\big]^p$.

Proof. This result follows from Theorem 5.2.1. By summing over set elements on each side of Eq. (5.6a), Eq. (5.11a) is obtained directly, with the dressed vertex $(\alpha)'_{\mathcal{G}}$ taking the form

$$(\alpha)'_{\mathcal{G}} = \sum_{n=0}^{\infty}\left[\sum_{\tilde{C}_{\mathcal{G};\alpha}} (\alpha\eta_2)\,(\eta_2\eta_3)\cdots(\eta_m\alpha)\right]^n, \tag{5.12}$$

where m is the length of the cycle $(\alpha\eta_2\cdots\eta_m\omega) \in \tilde{C}_{\mathcal{G};\alpha}$. By using Eq. (5.6b) to recast the sum over cycles in this expression into a sum over simple cycles with dressed internal vertices, the recursive form of Eq. (5.11b) for $(\alpha)'_{\mathcal{G}}$ is obtained. ■

5.3.2 The sum of walk weights on a weighted directed graph

We now move to a weighted graph $(\mathcal{G}, \varphi)$ and present the equivalent of Theorem 5.3.1 for the weights of walks, rather than the walks themselves. We convert the sum of the weights of all walks from α to ω to a sum over weighted paths by assigning an 'effective weight' to each vertex visited by each path. This effective weight accounts for the vertex being dressed by the weights of all possible combinations of concatenated and nested simple cycles off it.

Theorem 5.3.2. *The sum of the weights of all walks from α to ω on a weighted graph $(\mathcal{G}, \varphi)$ is given by*

$$\varphi\big[\Sigma_{\mathcal{G};\alpha\omega}\big] = \sum_{P_{\mathcal{G};\alpha\omega}} \mathsf{F}_{\mathcal{G}\setminus\{\alpha,\nu_2,\ldots,\nu_\ell\};\omega}\, \mathsf{f}_{\omega\nu_\ell} \cdots \mathsf{F}_{\mathcal{G}\setminus\{\alpha\};\nu_2}\, \mathsf{f}_{\nu_2\alpha}\, \mathsf{F}_{\mathcal{G};\alpha}, \tag{5.13a}$$

where $\mathsf{f}_{\nu\mu} = \varphi[(\mu\nu)]$ is the weight of the edge $(\mu\nu)$, and

$$\mathsf{F}_{\mathcal{G};\alpha} = \varphi\big[(\alpha)'_{\mathcal{G}}\big] = \left[\mathrm{Id}_\alpha - \sum_{C_{\mathcal{G};\alpha}} \mathsf{f}_{\alpha\mu_m}\, \mathsf{F}_{\mathcal{G}\setminus\{\alpha,\mu_2,\ldots,\mu_{m-1}\};\mu_m}\, \mathsf{f}_{\mu_m\mu_{m-1}} \cdots \mathsf{F}_{\mathcal{G}\setminus\{\alpha\};\mu_2}\, \mathsf{f}_{\mu_2\alpha}\right]^{-1} \tag{5.13b}$$

is the effective weight of the vertex α on $\mathcal{G}$.

Proof. This follows from Theorem 5.3.1 and the properties of the weight function defined in Eq. (5.5). ■

One particular application of Theorem 5.3.2 is found by setting V_μ to be a complex vector space of dimension d_μ. Then $\mathsf{f}_{\nu\mu}$ is a a d_ν-by-d_μ matrix representing a linear mapping from V_μ to V_ν, and Id_μ is the identity matrix of dimension d_μ. Theorem 5.3.2 then provides a compact expression for the sum of all possible mappings from V_α to V_ω; this expression takes the form of a matrix-valued continued fraction. We present the details of this application in Chapter 6.

5.4 Illustrative applications

By using the result of Theorem 5.3.2, any quantity that can be written as a sum of weights of walks on a graph $\mathcal{G}$ can be converted to a sum over weights of paths on $\mathcal{G}$. In this section we give two illustrative examples of this: firstly, we obtain a continued-fraction representation of the walk-generating function of a graph, and secondly, we give a novel recursive formula for the quasideterminants of a matrix.

5.4.1 The walk-generating function of a graph

Given any two vertices α, ω of a graph $\mathcal{G}$, the walk-generating function $g_{\mathcal{G};\alpha\omega}(z)$ is a formal power series in z with non-negative integer coefficients, defined by

$$g_{\mathcal{G};\alpha\omega}(z) = \sum_{n=0}^{\infty} c_{\mathcal{G};\alpha\omega;n}\, z^n \tag{5.14}$$

where $c_{\mathcal{G};\alpha\omega;n} \in \{0, 1, 2, \ldots\}$ is the number of walks of length n from α to ω on $\mathcal{G}$. The function $g_{\mathcal{G};\alpha\omega}(z)$ is commonly computed from the adjacency matrix A of $\mathcal{G}$ through $g_{\mathcal{G};\alpha\omega}(z) = (\mathsf{I} - z\mathsf{A})^{-1}[\alpha, \omega]$, where I is the identity matrix of the appropriate dimension [149]; here we give an alternative formula for it.

Corollary 5.4.1. *The walk-generating function $g_{\mathcal{G};\alpha\omega}(z)$ is given by*

$$g_{\mathcal{G};\alpha\omega}(z) = \sum_{P_{\mathcal{G};\alpha\omega}} z^{\ell}\, g_{\mathcal{G};\alpha\alpha}(z)\, g_{\mathcal{G}\setminus\{\alpha\};\nu_2\nu_2}(z) \cdots g_{\mathcal{G}\setminus\{\alpha,\nu_2,\ldots,\nu_\ell\};\omega\omega}(z) \tag{5.15a}$$

where ℓ is the length of the path $(\alpha\nu_2\cdots\nu_\ell\omega) \in P_{\mathcal{G};\alpha\omega}$, and

$$g_{\mathcal{G};\alpha\alpha}(z) = \Big[1 - \sum_{C_{\mathcal{G};\alpha}} z^m g_{\mathcal{G}\setminus\{\alpha\};\mu_2\mu_2}(z) \cdots g_{\mathcal{G}\setminus\{\alpha,\mu_2,\ldots,\mu_{m-1}\};\mu_m\mu_m}(z)\Big]^{-1} \tag{5.15b}$$

where m is the length of the simple cycle $(\alpha\mu_2\ldots\mu_m\alpha) \in C_{\mathcal{G};\alpha}$.

Proof. Consider the weighted graph formed by pairing $\mathcal{G}$ with a weight function φ that assigns the formal variable z to each edge of $\mathcal{G}$; i.e. $\varphi[e] = z$ for every edge $e \in \mathcal{E}$. Then every walk of length n has the same weight z^n, and we can write

$$g_{\mathcal{G};\alpha\omega}(z) = \varphi\big[\Sigma_{\mathcal{G};\alpha\omega}\big] \tag{5.16a}$$

and

$$g_{\mathcal{G};\alpha\alpha}(z) = \varphi\big[(\alpha)'_{\mathcal{G}}\big]. \tag{5.16b}$$

The result of Corollary 5.4.1 then follows immediately from Theorem 5.3.2. ■

As an example of Corollary 5.4.1, consider computing the walk-generating function $g_{\mathcal{G};12}(z)$ for the directed graph $\mathcal{G}$ defined by the adjacency matrix

$$\mathsf{A}_{\mathcal{G}} = \begin{pmatrix} 1 & 1 & 1 \\ 1 & 1 & 0 \\ 0 & 1 & 0 \end{pmatrix}. \tag{5.17}$$

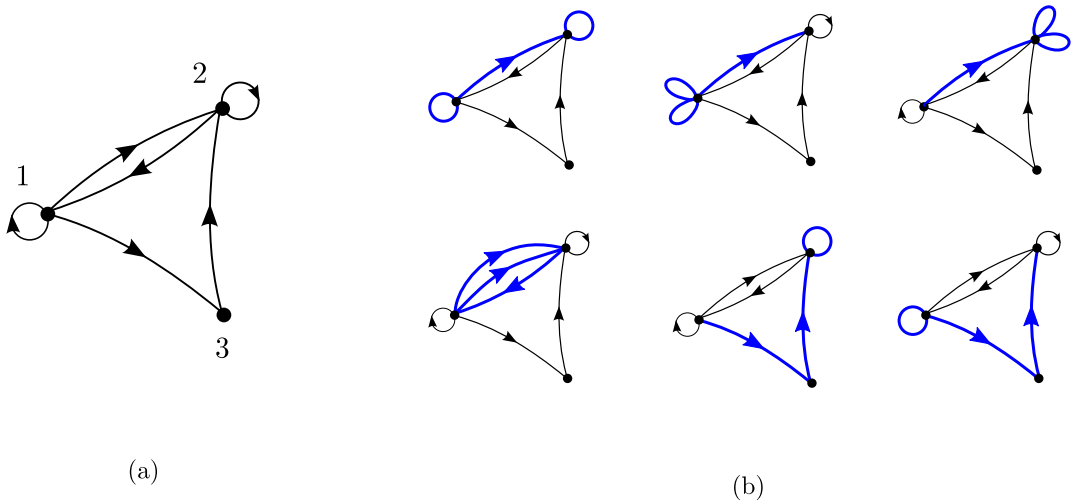

Figure 5.4: (a) The directed graph $\mathcal{G}$ described by the adjacency matrix of Eq. (5.17). (b) The six walks of length 3 from vertex 1 to vertex 2 on $\mathcal{G}$.

This graph is illustrated in Figure 5.4(a). The set of paths from 1 to 2 on $\mathcal{G}$ is $P_{\mathcal{G};12} = \{(12), (132)\}$, so that applying Corollary 5.4.1 gives

$$g_{\mathcal{G};12}(z) = z\, g_{\mathcal{G};11}(z)\, g_{\mathcal{G}\setminus\{1\};22}(z) + z^2\, g_{\mathcal{G};11}(z)\, g_{\mathcal{G}\setminus\{1\};33}(z)\, g_{\mathcal{G}\setminus\{1,3\};22}(z). \tag{5.18}$$

Using the fact that $C_{\mathcal{G};1} = \{(11), (121), (1321)\}$, we find

$$g_{\mathcal{G};11}(z) = \left(1 - z - z^2 g_{\mathcal{G}\setminus\{1\};22}(z) - z^3 g_{\mathcal{G}\setminus\{1\};33}\, g_{\mathcal{G}\setminus\{1,3\};22}\right)^{-1}, \tag{5.19}$$

while $g_{\mathcal{G}\setminus\{1\};22} = \left(1-z\right)^{-1}$, $g_{\mathcal{G}\setminus\{1\};33} = 1$, and $g_{\mathcal{G}\setminus\{1,3\};22} = \left(1-z\right)^{-1}$. Assembling these expressions gives

$$\begin{aligned} g_{\mathcal{G};12}(z) &= z\left(1 - z - z^2(1-z)^{-1} - z^3(1-z)^{-1}\right)^{-1}(1-z)^{-1} \\ &\quad + z^2\left(1 - z - z^2(1-z)^{-1} - z^3(1-z)^{-1}\right)^{-1}(1-z)^{-1} \\ &= \frac{z + z^2}{1 - 2z + z^3} \\ &= z + 3z^2 + 6z^3 + 13z^4 + 29z^5 + \cdots \end{aligned} \tag{5.20}$$

which agrees with the result obtained by computing the matrix $(\mathsf{I} - z\mathsf{A}_{\mathcal{G}})^{-1}$ and extracting the element in the first row and second column. The six walks of length 3 from vertex 1 to vertex 2 are illustrated in Figure 5.4(b).

5.4.2 A path-sum approach to quasideterminants

Matrix determinants are a central object of study in commutative linear algebra. As a consequence of their importance, numerous attempts have been made to extend the definition of a determinant to matrices with non-commuting entries [152, 153, 154, 155, 156]. Quasideterminants are one such extension that have proved useful in the fields of noncommutative algebra, representation theory, and noncommutative geometry. Although their foundations appeared in the literature as early as the 1920s, quasideterminants lay largely dormant until they were rediscovered and popularised in a series of papers by Gel'fand and Retakh over the past two decades [157, 158, 159]. The following definition is taken from their 1992 paper [158].

Let $\mathsf{A} = (a_{ij})$ be a square matrix of size n with formal non-commuting entries a_{ij}. We inductively define n^2 quantities $|\mathsf{A}|_{pq}$ for $1 \leq p \leq n$, $1 \leq q \leq n$, called the quasideterminants of A, as follows. For $n = 1$, we define the single quasideterminant $|\mathsf{A}|_{11} = a_{11}$. For $n \geq 2$, suppose that the quasideterminants for all matrices of size less than n are already defined. We denote by A^{ab} the square matrix of size $n-1$ obtained from A by deleting the a^{th} row and b^{th} column, and set

$$|\mathsf{A}|_{pq} = a_{pq} - \sum_{\substack{i \neq p \\ j \neq q}} a_{pj} |\mathsf{A}^{pq}|^{-1}_{ij} a_{iq}. \tag{5.21}$$

For example, the 2×2 matrix $\mathsf{A} = \begin{pmatrix} a_{11} & a_{12} \\ a_{21} & a_{22} \end{pmatrix}$ has the following four quasideterminants:

$$|\mathsf{A}|_{11} = a_{11} - a_{12} a_{22}^{-1} a_{21} \qquad |\mathsf{A}|_{12} = a_{12} - a_{11} a_{21}^{-1} a_{22} \tag{5.22a}$$

$$|\mathsf{A}|_{21} = a_{21} - a_{22} a_{12}^{-1} a_{11} \qquad |\mathsf{A}|_{22} = a_{22} - a_{21} a_{11}^{-1} a_{12}. \tag{5.22b}$$

Many properties of quasideterminants mirror those of the commutative determinant: they behave well with respect to row and column operations, can be used to solve linear systems of equations in noncommuting variables, and may be used to build the inverse of a matrix with noncommuting entries. However the quasideterminants of a matrix A whose entries do commute reproduce not the ordinary determinant, but rather the ratio of the determinant of A to that of a minor of A: $|\mathsf{A}|_{ij} = (-1)^{i+j} \det \mathsf{A} / \det \mathsf{A}^{ij}$. A recent review article [160] contains a full discussion of the properties of quasideterminants. We now present the main result of this section.

Theorem 5.4.2. *Let $\mathsf{X} = (x_{\mu\nu})$ be a square matrix of size N with formal entries $x_{\mu\nu}$ for $1 \leq \mu, \nu \leq N$, and let $\mathsf{X}^{(\delta_1,\ldots,\delta_m)}$ be the matrix formed by deleting all rows and columns of X with indices $\delta_1, \ldots, \delta_m$. Then the quasideterminants $|\mathsf{I} - \mathsf{X}|_{\omega\alpha}$ for $1 \leq \alpha, \omega \leq N$ are given by*

$$\left|\mathsf{I} - \mathsf{X}\right|^{-1}_{\omega\alpha} = \sum_{P_{\mathcal{G};\alpha\omega}} \left|\mathsf{I} - \mathsf{X}\right|^{-1}_{\alpha\alpha} x_{\alpha\nu_2} \left|\mathsf{I} - \mathsf{X}^{(\alpha)}\right|^{-1}_{\nu_2\nu_2} \cdots x_{\nu_\ell\omega} \left|\mathsf{I} - \mathsf{X}^{(\alpha\nu_2\cdots\nu_\ell)}\right|^{-1}_{\omega\omega} \tag{5.23a}$$

where ℓ is the length of the path $(\alpha\nu_2\cdots\nu_\ell\omega) \in P_{\mathcal{G};\alpha\omega}$, and

$$\left|\mathsf{I} - \mathsf{X}\right|_{\alpha\alpha} = 1 - \sum_{C_{\mathcal{G};\alpha}} x_{\alpha\mu_2} \left|\mathsf{I} - \mathsf{X}^{(\alpha)}\right|^{-1}_{\mu_2\mu_2} x_{\mu_2\mu_3} \cdots \left|\mathsf{I} - \mathsf{X}^{(\alpha\nu_2\cdots\mu_{m-1})}\right|^{-1}_{\mu_m\mu_m} x_{\mu_m\alpha},, \tag{5.23b}$$

where m is the length of the simple cycle $(\alpha\mu_2\cdots\mu_m\alpha) \in C_{\mathcal{G};\alpha}$.

Proof. The fact that quasideterminants can be expressed as sums of weights of walks on a weighted graph is pointed out in Proposition 1.2.8 of [160].[1] In the present notation, that result is

$$\left|\mathsf{I} - \mathsf{X}\right|^{-1}_{\omega\alpha} = \sum_{W_{\mathcal{G};\alpha\omega}} x_{\alpha\eta_2} x_{\eta_2\eta_3} \cdots x_{\eta_n\omega}, \tag{5.24a}$$

$$\left|\mathsf{I} - \mathsf{X}\right|_{\alpha\alpha} = 1 - \sum_{\tilde{C}_{\mathcal{G};\alpha}} x_{\alpha\mu_2} x_{\mu_2\mu_3} \cdots x_{\mu_m\omega}. \tag{5.24b}$$

where $\mathcal{G}$ is the graph on N vertices with a loop on each vertex. By introducing a weight function φ that assigns the formal variable $x_{\mu\nu}$ to the edge $(\mu\nu)$, we rewrite these expressions as

$$\left|\mathsf{I} - \mathsf{X}\right|^{-1}_{\omega\alpha} = \varphi\big[\Sigma_{\mathcal{G};\alpha\omega}\big], \tag{5.25a}$$

$$\left|\mathsf{I} - \mathsf{X}\right|^{-1}_{\omega\alpha} = \varphi\big[(\alpha)'_{\mathcal{G}}\big]. \tag{5.25b}$$

By using Theorem 5.3.2 to recast these sums into a recursive closed form, the result of Theorem 5.4.2 follows directly. ■

Theorem 5.4.2 relates the quasideterminants of a matrix X to those of its submatrices $\mathsf{X}^{(\alpha)}, \ldots, \mathsf{X}^{(\alpha\nu_2\cdots\nu_\ell)}$, and complements a previous result of Gel'fand and

[1] Note that the authors use the term 'path' for our 'walk', 'simple path from i to i' for our 'cycle off vertex i', and 'word' to denote the weight of a walk.

Retakh [158] that relates the quasideterminant $\left|\mathsf{X}\right|_{\omega\alpha}$ to the quasideterminants of $\mathsf{X}^{\omega\alpha}$, the minor of X obtained by deleting the ω^{th} row and α^{th} column of X.

5.5 Summary

We presented a method for decomposing any walk on a graph $\mathcal{G}$ into a simple path and a concatenated collection of recursively-nested simple cycles. We used the path decomposition to obtain a compact expression for the basis of the walk algebra $K\mathcal{G}$. Further, we showed that the sum of all walks linking a given pair of vertices on $\mathcal{G}$ can be written in a compact closed form, and presented two illustrative examples of how this result can be applied to weighted graphs. The summation result is also of key importance in the next chapter, in which we develop the path-sum method of evaluating matrix functions.

Chapter 6

The method of path-sums

In this chapter, which builds on the results of Chapter 5, we introduce the method of path-sums, a novel symbolic method for evaluating a matrix function $f(\mathsf{M})$ analytically and in closed form. The method of path-sums exploits connections between matrix multiplication and walks on weighted directed graphs, and is based on three central concepts. Firstly, the matrix M is partitioned into a collection of submatrices, with which we associate a weighted directed graph $\mathcal{G}$. Secondly, we show that the problem of evaluating any submatrix of $f(\mathsf{M})$ is equivalent to summing the weights of all the walks that join a particular pair of vertices in $\mathcal{G}$. Thirdly, we use the universal result on the structure of walks on directed graphs presented in Chapter 5 to exactly resum the weights of certain families of walks. In this fashion we reduce the sum over walk weights to a sum over weighted paths.

We apply the method of path-sums to four common matrix functions: a matrix raised to an arbitrary complex power, the matrix inverse, matrix exponential, and matrix logarithm. In each case, we obtain an exact closed-form expression that allows the corresponding function $f(\mathsf{M})$ to be analytically evaluated in a finite number of operations.

The chapter is organized as follows. In §6.1 we present the fundamental concepts that underpin the method of path-sums. We describe the partition of a matrix into submatrices, the construction of the corresponding weighted directed graph, and the mapping between matrix multiplication and walks on this graph. In §6.2 we present path-sum expressions for a matrix raised to an arbitrary complex power, the matrix inverse, the matrix exponential, and the matrix logarithm; these results are proved in §6.3. In §6.4 we provide numerical examples of the application of the

method of path-sums, and in §6.5 we comment on prospects for the application of the method to the simulation of strongly-correlated many-body systems.

The work appearing in this chapter was carried out in close collaboration with Pierre-Louis Giscard. The background material of §6.1 is due to Pierre-Louis Giscard, though the current presentation and formulation is due to the present author. The main results of §6.2 and §6.3 are the work of the present author in collaboration with Pierre-Louis Giscard, and represent significant extensions of previous results obtained by Pierre-Louis Giscard linking matrix functions and walks on graphs. The numerical examples of §6.4 are due to Pierre-Louis Giscard, in collaboration with the present author. The work in this chapter forms the basis for a publication that has been submitted to the *SIAM Journal on Matrix Analysis and Applications*; a pre-print of this manuscript, which also includes a number of new developments, has recently been made available [161].

6.1 Background material

In this section we present the three main concepts that underpin the method of path-sums. We begin by outlining the partition of a matrix M into a collection of subarrays, and show how this partitioning leads naturally to the definition of a weighted directed graph $\mathcal{G}$ that encodes the structure of M. We then show that computing any power of the matrix M is equivalent to evaluating the sum of the weights of a certain family of walks on $\mathcal{G}$.

6.1.1 Matrix partitions

A partition of a matrix M is a regrouping of the elements of M into an ensemble of smaller arrays which interpolate between the usual matrix elements of M and the matrix M itself. These subarrays can be used to compute any function of M that can be expressed as a power series.

General partitions

Let $\mathsf{M} \in \mathbb{C}^{D\times D}$ be a square matrix of size D over the complex field $\mathbb{C}$, and let V be a D-dimensional vector space over $\mathbb{C}$ with orthonormal basis $\{\mathsf{v}_i\}_{i=1}^{D}$. Consider an ensemble of vector spaces $V_1, V_2, \ldots, V_n$ such that $V_1 \oplus V_2 \oplus \cdots \oplus V_n = V$. Let the j^{th} vector space have dimension d_j and orthonormal basis $\mathsf{v}_{i_{j,k}}$, with $1 \leq k \leq d_j$

and $1 \leq i_{j,k} \leq D$. We define an orthogonal projector onto V_j by

$$\mathsf{P}_j = \sum_{k=1}^{d_j} \mathsf{v}_{i_{j,k}} \mathsf{v}_{i_{j,k}}^\dagger, \tag{6.1}$$

where $\mathsf{v}^\dagger$ denotes the conjugate transpose of v. These projectors satisfy

$$\mathsf{P}_i \, \mathsf{P}_j = \delta_{ij} \, \mathsf{P}_i \tag{6.2a}$$

$$\sum_{j=1}^{n} \mathsf{P}_j = \mathsf{I} \tag{6.2b}$$

where I is the identity matrix of size D. Finally, we define the restriction matrix $\mathsf{R}_j \in \mathbb{C}^{d_j \times D}$ such that $\mathsf{R}_j^{\mathrm{T}} \mathsf{R}_j = \mathsf{P}_j$.

A *general partition* of the matrix M is the ensemble $\{\mathsf{M}_{ij}\}$ for $1 \leq i, j \leq n$, where

$$\mathsf{M}_{ij} = \mathsf{R}_i \mathsf{M} \mathsf{R}_j^{\mathrm{T}}. \tag{6.3}$$

The matrix $\mathsf{M}_{ij} \in \mathbb{C}^{d_i \times d_j}$ is a subarray of M, and defines a linear map $\phi_{ij} : V_j \to V_i$. For $i \neq j$, we term M_{ij} a flip, while for $i = j$ we term $\mathsf{M}_{ii} = \mathsf{M}_i$ a static. In general there is no relationship between M_{ij} and M_{ji}; however, if M is Hermitian then $\mathsf{M}_{ij} = \mathsf{M}_{ji}^\dagger$ and $\mathsf{M}_i = \mathsf{M}_i^\dagger$. Similar relations can be derived for the case where M is anti-Hermitian, symmetric, or anti-symmetric.

Example: general partition. To illustrate the concept of a general partition, let M be the 4×4 matrix with elements $\mathsf{M}[i, j] = m_{ij}$. This matrix can be interpreted as a linear map on the vector space $V = \mathrm{span}(\mathsf{v}_1, \mathsf{v}_2, \mathsf{v}_3, \mathsf{v}_4)$, where $\mathsf{v}_1 = (1, 0, 0, 0)^{\mathrm{T}}$, $\mathsf{v}_2 = (0, 1, 0, 0)^{\mathrm{T}}$, etc. We choose to partition the matrix M onto vector spaces $V_1 = \mathrm{span}(\mathsf{v}_1, \mathsf{v}_3, \mathsf{v}_4)$ and $V_2 = \mathrm{span}(\mathsf{v}_2)$, which satisfy $V_1 \oplus V_2 = V$. Then the restriction matrices R_i are

$$\mathsf{R}_1 = \begin{pmatrix} 1 & 0 & 0 & 0 \\ 0 & 0 & 1 & 0 \\ 0 & 0 & 0 & 1 \end{pmatrix}, \qquad \mathsf{R}_2 = \begin{pmatrix} 0 & 1 & 0 & 0 \end{pmatrix}, \tag{6.4}$$

so that the general partition of M consists of the four matrices

$$\mathsf{M}_{11} = \mathsf{R}_1\mathsf{M}\mathsf{R}_1^{\mathrm{T}} = \begin{pmatrix} m_{11} & m_{13} & m_{14} \\ m_{31} & m_{33} & m_{34} \\ m_{41} & m_{43} & m_{14} \end{pmatrix}, \qquad \mathsf{M}_{12} = \mathsf{R}_1\mathsf{M}\mathsf{R}_2^{\mathrm{T}} = \begin{pmatrix} m_{12} \\ m_{32} \\ m_{42} \end{pmatrix} \tag{6.5}$$

$$\mathsf{M}_{21} = \mathsf{R}_2\mathsf{M}\mathsf{R}_1^{\mathrm{T}} = \begin{pmatrix} m_{21} & m_{23} & m_{24} \end{pmatrix}, \qquad \mathsf{M}_{22} = \mathsf{R}_2\mathsf{M}\mathsf{R}_2^{\mathrm{T}} = \begin{pmatrix} m_{22} \end{pmatrix}. \tag{6.6}$$

Number of general partitions. The partition of a matrix M into a collection of flips and statics is not unique: any ensemble of vector spaces that satisfy $\bigoplus_{i=1}^{n} V_i = V$ produces a valid partition of M. It follows that a $D \times D$ matrix may be decomposed onto n vector spaces in $S(D,n)$ different ways, where $S(D,n)$ is the Stirling number of the second kind, and the total number of general partitions of M is the D^{th} Bell number, $B_D = \sum_{n=1}^{D} S(D,n)$. Included in this number are the trivial partition of M into a single static $\mathsf{M}_1 = \mathsf{M}$, which is obtained by choosing $V_1 = V$, and the partition of M into its usual matrix elements (i.e. $\mathsf{M}_{ij} = (\mathsf{M}[i,j])$), obtained by choosing $\{V_i\}$ to be D vector spaces of dimension one. Between these extremes, the subarrays M_{ij} interpolate between the normal matrix elements of M and the matrix M itself. Figure 6.1 illustrates the full collection of possible partitions of a 4×4 matrix into submatrices.

Tensor-product partitions. An important subclass of matrix partitions are those that are produced by projectors of tensor-product form. Partitions of this type, which will be referred to as tensor-product partitions, arise when the vector space V is decomposed as the tensor product (instead of the direct sum) of a collection of subspaces.

Let V be a D-dimensional vector space over the complex field $\mathbb{C}$, and consider an ensemble of vector spaces $\mathcal{V}_1, \mathcal{V}_2, \ldots, \mathcal{V}_N$ such that $\mathcal{V}_1 \otimes \mathcal{V}_2 \otimes \cdots \otimes \mathcal{V}_N = V$. Let the i^{th} vector space have dimension d_i, where $2 \leq d_i \leq D$, and orthonormal basis $\{|\mu_i\rangle^{(i)}\}$, where $1 \leq \mu_i \leq d_i$. Let $P_{\mu_i}^{(i)} = |\mu_i\rangle^{(i)}\langle\mu_i|$ be the orthogonal projector onto the one-dimensional subspace of $\mathcal{V}_i$ spanned by $|\mu_i\rangle^{(i)}$. Then a projector of tensor-product form is

$$\varepsilon_{\mu}^{(S)} = \bigotimes_{i=1}^{S-1} P_{\mu_i}^{(i)} \otimes \mathsf{I}^{(S)} \otimes \bigotimes_{i=S+1}^{N} P_{\mu_i}^{(i)}, \tag{6.7}$$

where S is a fixed index between 1 and N, $\mathsf{I}^{(S)}$ is the identity matrix in $\mathcal{V}_S$, and

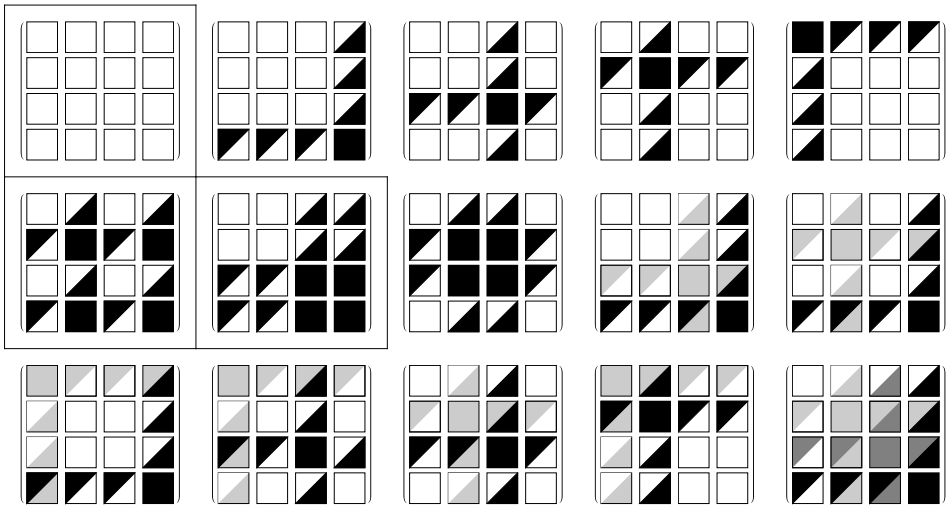

Figure 6.1: An illustration of the $B_4 = 15$ possible partitions of a 4×4 matrix. Solid and bi-color squares represent the matrix elements of statics and flips, respectively. The three tensor-product partitions are framed. The trivial partition is in the upper-left corner, while the partition into the usual matrix elements is in the lower-right corner.

$\mu = (\mu_1, \ldots, \mu_{S-1}, \mu_{S+1}, \ldots, \mu_N)$ is an $(N-1)$-dimensional multi-index denoting which orthogonal projectors are present in $\varepsilon_\mu^{(S)}$. Hence $\varepsilon_\mu^{(S)}$ acts as a projector onto a single basis vector in each subspace $\mathcal{V}_i$ $(i \neq S)$ and applies the identity matrix to the subspace $\mathcal{V}_S$. For fixed S there are D/d_S different projectors corresponding to the different choices of the components of the multi-index μ. For any $D \times D$ matrix M and pair of projectors $\varepsilon_\mu^{(S)}, \varepsilon_\nu^{(S)}$, there exists a matrix $\mathsf{M}_{\mu\nu}^{(S)} \in \mathbb{C}^{d_S \times d_S}$ such that

$$\varepsilon_\mu^{(S)} \mathsf{M}\, \varepsilon_\nu^{(S)} = \bigotimes_{i=1}^{S-1} \mathsf{T}_{\mu_i\nu_i}^{(i)} \otimes \mathsf{M}_{\mu\nu}^{(S)} \otimes \bigotimes_{i=S+1}^{N} \mathsf{T}_{\mu_i\nu_i}^{(i)}, \tag{6.8}$$

where $\mathsf{T}_{\mu_i\nu_i}^{(i)} = |\mu_i\rangle^{(i)}\langle\nu_i|$ is a transition matrix from $|\nu_i\rangle^{(i)}$ to $|\mu_i\rangle^{(i)}$ in $\mathcal{V}_i$. The matrix $\mathsf{M}_{\mu\nu}^{(S)}$ defines a linear map on $\mathcal{V}_S$. The ensemble of $(D/d_S)^2$ matrices $\left\{\mathsf{M}_{\mu\nu}^{(S)}\right\}$ will be referred to as a tensor product partition of M.

Example: tensor-product partition. To illustrate the construction of a tensor-product partition of a matrix, we now present an example. Consider again the general 4×4 matrix M with elements $\mathsf{M}[i,j] = m_{ij}$. In addition to the trivial case of $\mathcal{V}_1 = V$ with corresponding partition $\mathsf{M}_1^{(1)} = \mathsf{M}$, the vector space V can be decomposed into a pair of subspaces $\mathcal{V}_1, \mathcal{V}_2$ such that $\mathcal{V}_1 \otimes \mathcal{V}_2 = V$. In this case there are two possible partitions of M, corresponding to the two different choices of S. Setting $S = 1$ gives

$$\varepsilon_1^{(1)} = \begin{pmatrix} 1 & 0 \\ 0 & 1 \end{pmatrix}^{(1)} \otimes \begin{pmatrix} 1 & 0 \\ 0 & 0 \end{pmatrix}^{(2)}, \qquad \varepsilon_2^{(1)} = \begin{pmatrix} 1 & 0 \\ 0 & 1 \end{pmatrix}^{(1)} \otimes \begin{pmatrix} 0 & 0 \\ 0 & 1 \end{pmatrix}^{(2)}, \tag{6.9}$$

which yields the partition

$$\mathsf{M}_1^{(1)} = \begin{pmatrix} m_{11} & m_{13} \\ m_{31} & m_{33} \end{pmatrix}, \quad \mathsf{M}_2^{(1)} = \begin{pmatrix} m_{22} & m_{24} \\ m_{42} & m_{44} \end{pmatrix}, \tag{6.10a}$$

$$\mathsf{M}_{12}^{(1)} = \begin{pmatrix} m_{12} & m_{14} \\ m_{32} & m_{34} \end{pmatrix}, \quad \mathsf{M}_{21}^{(1)} = \begin{pmatrix} m_{21} & m_{23} \\ m_{41} & m_{43} \end{pmatrix}, \tag{6.10b}$$

while setting $S = 2$ instead gives

$$\varepsilon_1^{(2)} = \begin{pmatrix} 1 & 0 \\ 0 & 0 \end{pmatrix}^{(1)} \otimes \begin{pmatrix} 1 & 0 \\ 0 & 1 \end{pmatrix}^{(2)}, \qquad \varepsilon_2^{(2)} = \begin{pmatrix} 0 & 0 \\ 0 & 1 \end{pmatrix}^{(1)} \otimes \begin{pmatrix} 1 & 0 \\ 0 & 1 \end{pmatrix}^{(2)}, \tag{6.11}$$

and

$$\mathsf{M}_1^{(2)} = \begin{pmatrix} m_{11} & m_{12} \\ m_{21} & m_{22} \end{pmatrix}, \quad \mathsf{M}_2^{(2)} = \begin{pmatrix} m_{33} & m_{34} \\ m_{43} & m_{44} \end{pmatrix}, \tag{6.12a}$$

$$\mathsf{M}_{12}^{(2)} = \begin{pmatrix} m_{13} & m_{14} \\ m_{23} & m_{24} \end{pmatrix}, \quad \mathsf{M}_{21}^{(2)} = \begin{pmatrix} m_{31} & m_{32} \\ m_{41} & m_{42} \end{pmatrix}. \tag{6.12b}$$

The three tensor product partitions of M are illustrated by the framed images in Figure 6.1. ■

To count the number of possible tensor-product partitions of a $D \times D$ matrix, we note that every factorisation of D into a collection of $k \geq 1$ integers $d_1, d_2, \ldots, d_k$, where $d_i \geq 2$, contributes k partitions to the total. The total number of tensor-product partitions is therefore equal to the total number of elements in all the factorisations of D. For $D = 2, 3, 4, 5, 6, 7, 8, \ldots$, this is equal to $1, 1, 3, 1, 3, 1, 6, \ldots$ (sequence A066637 in [162]). A special case arises when D has the form d^N, with d

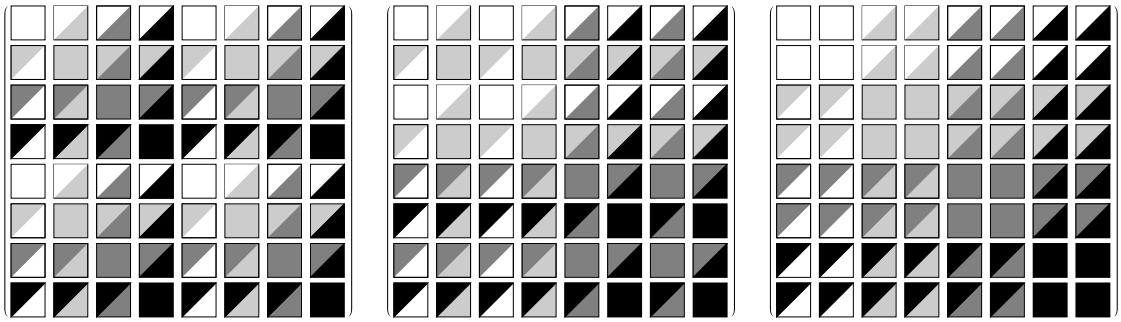

Figure 6.2: Three of the six possible tensor-product partitions of an 8×8 matrix onto three vector spaces of dimension 2. Plain and bi-color squares represent matrix elements of the 2×2 statics (flips) comprising the partition. This matrix admits a further 4134 partitions that are not of tensor-product form, for a total of $B_8 = 4140$ general partitions.

prime. Then the factorisations of D into k parts are in one-to-one correspondence with the additive partitions of N into k parts, and the number of tensor product partitions is equal to the total number of elements in all additive partitions of N. For example, matrices of dimension $D = 2, 4, 8, 16, 32, \ldots$ admit $1, 3, 6, 12, 20, \ldots$ (sequence A006128 in [162]) tensor-product partitions. Three of the six possible tensor-product partitions of an 8×8 matrix are illustrated in Figure 6.2.

6.1.2 Partitions of matrix powers and functions

Since the elements of $\mathsf{M}^2, \mathsf{M}^3, \ldots$ are generated from those of M through the rules of matrix multiplication, the partition of a matrix power can be expressed in terms of the partition of the original matrix. Here we present this relationship for the case of a general partition of M; the case of a tensor-product partition is essentially identical. The proof of these results is deferred to §6.3.

The elements of the partition of M^k for $k \in \{1, 2, 3, \ldots\}$ are given in terms of the partition of M by

$$\big(\mathsf{M}^k\big)_{\omega\alpha} = \sum_{\eta_k,\ldots,\eta_2} \mathsf{M}_{\omega\eta_k} \cdots \mathsf{M}_{\eta_3\eta_2} \mathsf{M}_{\eta_2\alpha}, \tag{6.13}$$

where $\alpha \equiv \eta_1$, $\omega \equiv \eta_{k+1}$, and each of the sums runs over the n values that index the vector spaces of the general partition. It follows that the elements of the partition of a matrix function $f(\mathsf{M})$ with power series expansion $f\big(\mathsf{M}\big) = \sum_{k=0}^{\infty} c_k \, \mathsf{M}^k$ are

given by

$$f\big(\mathsf{M}\big)_{\omega\alpha} = \sum_{k=0}^{\infty} c_k \sum_{\eta_k,\ldots,\eta_2} \mathsf{M}_{\omega\eta_k} \cdots \mathsf{M}_{\eta_3\eta_2} \mathsf{M}_{\eta_2\alpha}. \tag{6.14}$$

This equation provides a method of computing individual subarrays of $f\big(\mathsf{M}\big)$ without evaluating the full result. In the next section, we map the infinite sum of Eq. (6.14) into a sum over the weights of walks on a weighted directed graph, thus allowing families of terms of Eq. (6.14) to be resummed by applying results from graph theory.

6.1.3 The graph of a matrix partition

Given an arbitrary partition of a matrix M, we now construct a weighted directed graph $\mathcal{G}$ that encodes the structure of this partition. Terms that contribute to the matrix power M^k are then in one-to-one correspondence with walks of length k on $\mathcal{G}$.

Let $\{\mathsf{M}_{\mu\nu}\}$ be a partition of the matrix M formed by a particular set of n projectors $\{\varepsilon_\mu\}$. Then the graph of this matrix partition is defined to be the weighted directed graph $(\mathcal{V}, \mathcal{E}, \varphi)$, where $\mathcal{V} = \{v_\mu\}$ is a set of $m \leq n$ vertices with the same labels as the projectors, $\mathcal{E} = \{(\nu\mu) : \mathsf{M}_{\mu\nu} \neq 0\}$ is a set of directed edges among these vertices, and φ is a weight function such that

$$\varphi\big[(\nu\mu)\big] = \mathsf{M}_{\mu\nu} \tag{6.15}$$

for every edge $(\nu\mu) \in \mathcal{E}$. Equivalently, $\mathcal{G}$ can be specified by its adjacency matrix $\mathsf{A}_\mathcal{G}$, where

$$\mathsf{A}_\mathcal{G}[\nu,\mu] = \begin{cases} 1 & \text{if } \mathsf{M}_{\mu\nu} \neq \mathbf{0}, \\ 0 & \text{otherwise,} \end{cases} \tag{6.16}$$

together with the set $\{\mathsf{M}_{\mu\nu}\}$ of edge weights.

The graph $\mathcal{G}$ provides a useful visual representation of a matrix partition: each vertex represents a vector space, and each edge represents a linear mapping between vector spaces. The pattern of edges in $\mathcal{G}$ encodes the structure of M: each loop $(\mu\mu)$ represents a non-zero static, while each edge $(\nu\mu)$ represents a non-zero flip. Further, each walk of length k on $\mathcal{G}$ is in one-to-one correspondence with a

product of k elements of the partition of M, since from Eq. (6.15) together with the properties of the weight function given in Eq. (5.5) we have

$$\varphi\big[(\alpha\eta_2)(\eta_2\eta_3)\cdots(\eta_k\omega)\big] = \mathsf{M}_{\omega\eta_k}\cdots\mathsf{M}_{\eta_3\eta_2}\mathsf{M}_{\eta_2\alpha}. \tag{6.17}$$

This one-to-one correspondence allows partitions of arbitrary powers and functions of M to be recast as sums over weights of walks on $(\mathcal{G},\varphi)$. Equations (6.13) and (6.14) become

$$\big(\mathsf{M}^k\big)_{\omega\alpha} = \varphi\big[\Sigma_{\mathcal{G};\alpha\omega;k}\big] \tag{6.18a}$$

and

$$f\big(\mathsf{M}\big)_{\omega\alpha} = \sum_{k=0}^{\infty} c_k\,\varphi\big[\Sigma_{\mathcal{G};\alpha\omega;k}\big] \tag{6.18b}$$

where $\Sigma_{\mathcal{G};\alpha\omega;k}$ is the sum of all walks of length k from α to ω on $\mathcal{G}$. Recasting matrix functions as sums over walk weights in this way allows graph-theoretic results to be applied to the evaluation of matrix functions.

Example: the graph of a matrix partition. Consider the general partition the 4×4 matrix

$$\mathsf{M} = \begin{pmatrix} m_{11} & m_{12} & m_{13} & m_{14} \\ m_{21} & m_{22} & m_{23} & m_{24} \\ 0 & 0 & m_{33} & m_{34} \\ m_{41} & m_{42} & 0 & 0 \end{pmatrix} \tag{6.19}$$

onto vector spaces $V_1 = \mathrm{span}\big(|1\rangle,|2\rangle\big)$, $V_2 = \mathrm{span}\big(|3\rangle\big)$, $V_3 = \mathrm{span}\big(|4\rangle\big)$. The elements of the partition are

$$\mathsf{M}_1 = \begin{pmatrix} m_{11} & m_{12} \\ m_{21} & m_{22} \end{pmatrix}, \qquad \mathsf{M}_{12} = \begin{pmatrix} m_{13} \\ m_{23} \end{pmatrix}, \qquad \mathsf{M}_{13} = \begin{pmatrix} m_{14} \\ m_{24} \end{pmatrix} \tag{6.20a}$$

$$\mathsf{M}_{21} = \begin{pmatrix} 0 & 0 \end{pmatrix}, \qquad \mathsf{M}_2 = \begin{pmatrix} m_{33} \end{pmatrix}, \qquad \mathsf{M}_{23} = \begin{pmatrix} m_{34} \end{pmatrix} \tag{6.20b}$$

$$\mathsf{M}_{31} = \begin{pmatrix} m_{41} & m_{42} \end{pmatrix}, \qquad \mathsf{M}_{32} = \begin{pmatrix} 0 \end{pmatrix}, \qquad \mathsf{M}_3 = \begin{pmatrix} 0 \end{pmatrix}. \tag{6.20c}$$

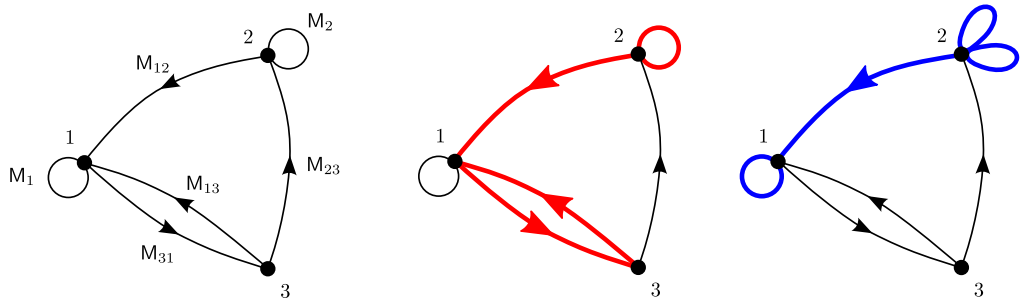

(a) (b)

Figure 6.3: (a) The graph of the general partition of the 4×4 matrix in Eq. (6.19) onto the vector spaces V_1, V_2, V_3 defined in the text. Each edge in the graph is labelled by its weight. (b) Two walks of length 4 from vertex 2 to vertex 1. Their weights $\mathsf{M}_{13}\mathsf{M}_{31}\mathsf{M}_{12}\mathsf{M}_2$ (left) and $\mathsf{M}_1\mathsf{M}_{12}\left(\mathsf{M}_2\right)^2$ (right) form two of the eight terms that sum to $(\mathsf{M}^4)_{12}$.

The corresponding graph $\mathcal{G}$ has adjacency matrix

$$\mathsf{A}_{\mathcal{G}} = \begin{pmatrix} 1 & 0 & 1 \\ 1 & 1 & 0 \\ 1 & 1 & 0 \end{pmatrix}, \tag{6.21}$$

where the zero entries arise since $\mathsf{M}_{21} = \mathsf{M}_{32} = \mathsf{M}_3 = \mathbf{0}$. Now consider the element $(\mathsf{M}^4)_{12}$. By multiplying M by itself, we find that

$$\begin{aligned}\left(\mathsf{M}^4\right)_{12} = {} & \left(\mathsf{M}_1\right)^3 \mathsf{M}_{12} + \mathsf{M}_{13}\,\mathsf{M}_{31}\,\mathsf{M}_1\,\mathsf{M}_{12} + \mathsf{M}_1\,\mathsf{M}_{13}\,\mathsf{M}_{31}\,\mathsf{M}_{12} + \mathsf{M}_{12}\,\mathsf{M}_{23}\,\mathsf{M}_{31}\,\mathsf{M}_{12} \\ & + \left(\mathsf{M}_1\right)^2 \mathsf{M}_{12}\,\mathsf{M}_2 + \mathsf{M}_{13}\,\mathsf{M}_{31}\,\mathsf{M}_{12}\,\mathsf{M}_{22} + \mathsf{M}_1\,\mathsf{M}_{12}\left(\mathsf{M}_2\right)^2 + \mathsf{M}_{12}\left(\mathsf{M}_2\right)^3. \end{aligned} \tag{6.22}$$

Each of the eight terms on the right-hand side of this equation can be identified as the weight of a walk of length 4 from vertex 2 to vertex 1 on $\mathcal{G}$,. This illustrates Eq. (6.18). Figure 6.3 shows the graph $\mathcal{G}$, together with two walks of length 4 from vertex 2 to vertex 1 that contribute to $\left(\mathsf{M}^4\right)_{12}$. ■

6.2 Path-sum expressions for common matrix functions

In the preceding section, we defined the weighted graph $(\mathcal{G}, \varphi)$ of a partition of a matrix M, and showed that the elements of the partition of any power or power

series of M can be expressed as the sum of the weights of various families of walks on $\mathcal{G}$. This mapping enables results from graph theory to be applied to the evaluation of matrix power series.

In this section we exploit this fact by using the results of Chapter 5 to resum, in closed form, certain families of terms in the power series expressions for some common matrix functions. We present results for a matrix raised to a complex power, and the inverse, exponential, and logarithm of a matrix. In each case, we use the result of Theorem 5.3.2 to resum all the terms in the power series that correspond to closed walks on $\mathcal{G}$, and thereby obtain a closed-form expression for the subarrays $f(\mathsf{M})_{\omega\alpha}$ for each matrix function f. Since the resultant expression takes the form of a finite sum over simple paths on $\mathcal{G}$, we refer to it as a path-sum expression. We defer the proofs of these results until §6.3.

6.2.1 A matrix raised to a complex power

Theorem 6.2.1 (Path-sum result for a matrix raised to a complex power)**.** *Let $\mathsf{M} \in \mathbb{C}^{D\times D}$ be a non-nilpotent complex matrix, q be a complex number, and $\{\mathsf{M}_{\mu\nu}\}$ be an arbitrary partition of M. Then the elements of the corresponding partition of M^q are given by*

$$\left(\mathsf{M}^q\right)_{\omega\alpha} = -\mathcal{Z}^{-1}\left\{\sum_{P_{\mathcal{G}_0;\alpha\omega}} \mathsf{F}_{\mathcal{G}\setminus\{\alpha,\nu_2,\ldots,\nu_\ell\};\omega}\,\mathsf{M}_{\omega\nu_\ell}\cdots\mathsf{F}_{\mathcal{G}\setminus\{\alpha\};\nu_2}\,\mathsf{M}_{\nu_2\alpha}\,\mathsf{F}_{\mathcal{G};\alpha}\right\}[n]\Big|_{n=-q-1} \tag{6.23a}$$

where $\mathcal{G}$ is the graph of $\{(\mathsf{M}-\mathsf{I})_{\mu\nu}\}$, ℓ is the length of the path $(\alpha\nu_2\cdots\nu_\ell\omega) \in P_{\mathcal{G}_0;\alpha\omega}$, and

$$\mathsf{F}_{\mathcal{G};\alpha} = \left[\mathsf{I}z^{-1} - \mathsf{M}_\alpha - \sum_{C_{\mathcal{G}_0;\alpha}} \mathsf{M}_{\alpha\mu_m}\,\mathsf{F}_{\mathcal{G}\setminus\{\alpha,\mu_2,\ldots,\mu_{m-1}\};\mu_m}\cdots\mathsf{F}_{\mathcal{G}\setminus\{\alpha\};\mu_2}\,\mathsf{M}_{\mu_2\alpha}\right]^{-1}, \tag{6.23b}$$

where m is the length of the simple cycle $(\alpha\mu_2\cdots\mu_m\omega) \in C_{\mathcal{G}_0;\alpha}$. □

Here $\mathcal{Z}^{-1}\{g(z)\}[n]$ denotes the inverse unilateral Z-transform of $g(z)$. The quantity $\mathsf{F}_{\mathcal{G};\alpha}$ is a matrix-valued continued fraction. It corresponds to an effective weight associated with the vertex α. which is the result of dressing α with the weights of all the closed walks off α on $\mathcal{G}$. If α has no neighbours in $\mathcal{G}$, then $\mathsf{F}_{\mathcal{G};\alpha} = [\mathsf{I}z^{-1} - \mathsf{M}_\alpha]^{-1}$ is the sum of the weights of all sequences of loops off α.

6.2.2 The inverse of a matrix

Theorem 6.2.2 (Path-sum result for the matrix inverse)**.** *Let* $\mathsf{M} \in \mathbb{C}^{D\times D}$ *be an invertible complex matrix, and* $\{\mathsf{M}_{\mu\nu}\}$ *be an arbitrary partition of* M*. Then as long as all of the required inverses exist, the elements of the corresponding partition of* M^{-1} *are given by*

$$\left(\mathsf{M}^{-1}\right)_{\omega\alpha} = \sum_{P_{\mathcal{G}_0;\alpha\omega}} (-1)^{\ell}\, \mathsf{F}_{\mathcal{G}\setminus\{\alpha,\ldots,\nu_\ell\};\omega}\, \mathsf{M}_{\omega\nu_\ell} \cdots \mathsf{F}_{\mathcal{G}\setminus\{\alpha\};\nu_2}\, \mathsf{M}_{\nu_2\alpha}\, \mathsf{F}_{\mathcal{G};\alpha}, \tag{6.24a}$$

where $\mathcal{G}$ *is the graph of* $\{(\mathsf{M}-\mathsf{I})_{\mu\nu}\}$*,* ℓ *is the length of the path* $(\alpha\nu_2\cdots\nu_\ell\omega) \in P_{\mathcal{G}_0;\alpha\omega}$*, and*

$$\mathsf{F}_{\mathcal{G};\alpha} = \left[\mathsf{M}_\alpha - \sum_{C_{\mathcal{G}_0;\alpha}} (-1)^m\, \mathsf{M}_{\alpha\mu_m}\, \mathsf{F}_{\mathcal{G}\setminus\{\alpha,\mu_2,\ldots,\mu_{m-1}\};\mu_m} \cdots \mathsf{F}_{\mathcal{G}\setminus\{\alpha\};\mu_2}\, \mathsf{M}_{\mu_2\alpha}\right]^{-1}, \tag{6.24b}$$

where m *is the length of the simple cycle* $(\alpha\mu_2\cdots\mu_m\alpha) \in C_{\mathcal{G}_0;\alpha}$*.* □

As above, $\mathsf{F}_{\mathcal{G};\alpha}$ is a matrix-valued continued fraction that can be viewed as an effective weight associated with vertex α, resulting from the dressing of α by the weights of all closed walks off α on $\mathcal{G}$. If α has no neighbours in $\mathcal{G}$, then $\mathsf{F}_{\mathcal{G};\alpha} = \mathsf{M}_\alpha^{-1}$ is the sum of the weights of all sequences of loops off α.

Two known matrix inversion results can be straightforwardly recovered as special cases of Theorem 6.2.2. Firstly, by considering the complete directed graph on two vertices, we obtain the well-known block inversion formula

$$\begin{pmatrix} \mathsf{A} & \mathsf{B} \\ \mathsf{C} & \mathsf{D} \end{pmatrix}^{-1} = \begin{pmatrix} (\mathsf{A}-\mathsf{B}\mathsf{D}^{-1}\mathsf{C})^{-1} & -\mathsf{A}^{-1}\mathsf{B}\,(\mathsf{D}-\mathsf{C}\mathsf{A}^{-1}\mathsf{B})^{-1} \\ -\mathsf{D}^{-1}\mathsf{C}\,(\mathsf{A}-\mathsf{B}\mathsf{D}^{-1}\mathsf{C})^{-1} & (\mathsf{D}-\mathsf{C}\mathsf{A}^{-1}\mathsf{B})^{-1} \end{pmatrix}. \tag{6.25}$$

Secondly, by applying Theorem 6.2.2 to the linear graph on D vertices $\mathcal{L}_D$, we obtain known continued fraction formulae for the inverse of a $D \times D$ tridiagonal matrix with commutative entries [163, 164]. This is a consequence of the observation that $\mathcal{L}_D$ is the graph of the partition of a $D \times D$ tridiagonal matrix into the usual scalar matrix elements.

6.2.3 The exponential of a matrix

Theorem 6.2.3 (**Path-sum result for the matrix exponential**)**.** *Let* $\mathsf{M} \in \mathbb{C}^{D\times D}$ *be a complex matrix;* τ *be a complex number; and* $\{\mathsf{M}_{\mu\nu}\}$ *be an arbitrary*

partition of M. *Then the elements of the corresponding partition of* $\exp(\tau\mathsf{M})$ *are given by*

$$\exp\big(\tau\mathsf{M}\big)_{\omega\alpha} = \mathfrak{L}^{-1}\left\{\sum_{P_{\mathcal{G}_0;\alpha\omega}} \mathsf{F}_{\mathcal{G}\setminus\{\alpha,\nu_2,\ldots,\nu_\ell\};\omega}\,\mathsf{M}_{\omega\nu_\ell}\,\cdots\,\mathsf{F}_{\mathcal{G}\setminus\{\alpha\};\nu_2}\,\mathsf{M}_{\nu_2\alpha}\,\mathsf{F}_{\mathcal{G};\alpha}\right\}(t)\Big|_{t=\tau}, \tag{6.26a}$$

where $\mathcal{G}$ *is the graph of* $\{\mathsf{M}_{\mu\nu}\}$, ℓ *is the length of the path* $(\alpha\nu_2\cdots\nu_\ell\omega) \in P_{\mathcal{G}_0;\alpha\omega}$, *and*

$$\mathsf{F}_{\mathcal{G};\alpha} = \left[s\mathsf{I} - \mathsf{M}_\alpha - \sum_{C_{\mathcal{G}_0;\alpha}} \mathsf{M}_{\alpha\mu_m}\,\mathsf{F}_{\mathcal{G}\setminus\{\alpha,\mu_2,\ldots,\mu_{m-1}\};\mu_m}\,\cdots\,\mathsf{F}_{\mathcal{G}\setminus\{\alpha\};\mu_2}\,\mathsf{M}_{\mu_2\alpha}\right]^{-1}, \tag{6.26b}$$

where m *is the length of the simple cycle* $(\alpha\mu_2\cdots\mu_m\alpha) \in C_{\mathcal{G}_0;\alpha}$. □

Here s is the Laplace variable conjugate to t, and $\mathfrak{L}^{-1}\{g(s)\}(t)$ denotes the inverse Laplace transform of $g(s)$. As before, the quantity $\mathsf{F}_{\mathcal{G};\alpha}$ is a matrix-valued continued fraction that corresponds to an effective weight for vertex α, which results from the dressing of α by the weights of all closed walks off α on $\mathcal{G}$. If α has no neighbours in $\mathcal{G}$ then $\mathsf{F}_{\mathcal{G};\alpha} = [s\mathsf{I} - \mathsf{M}_\alpha]^{-1}$ is the sum of the weights of all sequences of loops off α.

6.2.4 The logarithm of a matrix

Theorem 6.2.4 (Path-sum result for the principal logarithm)**.** *Let* $\mathsf{M} \in \mathbb{C}^{D\times D}$ *be a complex matrix with no eigenvalues on the negative real axis, and* $\{\mathsf{M}_{\mu\nu}\}$ *be a partition of* M. *Then as long as all of the required inverses exist, the elements of the corresponding partition of* $\log\mathsf{M}$ *are given by*

$$\big(\log\mathsf{M}\big)_{\omega\alpha} = \begin{cases} \displaystyle\int_0^1 \mathrm{d}x\; x^{-1}\big(\mathsf{I} - \mathsf{F}_{\mathcal{G};\alpha}\big), & \omega = \alpha \\ \displaystyle\sum_{P_{\mathcal{G}_0;\alpha\omega}} \int_0^1 \mathrm{d}x\; (-x)^{\ell-1}\,\mathsf{F}_{\mathcal{G}\setminus\{\alpha,\ldots,\nu_\ell\};\omega}\,\mathsf{M}_{\omega\nu_\ell}\,\cdots\,\mathsf{F}_{\mathcal{G}\setminus\{\alpha\};\nu_2}\,\mathsf{M}_{\nu_2\alpha}\,\mathsf{F}_{\mathcal{G};\alpha} & \omega \neq \alpha, \end{cases} \tag{6.27a}$$

where $\mathcal{G}$ *is the graph of* $\{(\mathsf{I}-\mathsf{M})_{\mu\nu}\}$, ℓ *is the length of the path* $(\alpha\nu_2\cdots\nu_\ell\omega) \in P_{\mathcal{G}_0;\alpha\omega}$, *and*

$$\mathsf{F}_{\mathcal{G};\alpha} = \left[\mathsf{I} - x\big(\mathsf{I}-\mathsf{M}_\alpha\big) - \sum_{C_{\mathcal{G}_0;\alpha}} (-x)^m\, \mathsf{M}_{\alpha\mu_m}\, \mathsf{F}_{\mathcal{G}\setminus\{\alpha,\mu_2,\ldots,\mu_{m-1}\};\mu_m} \cdots \mathsf{M}_{\mu_3\mu_2}\, \mathsf{F}_{\mathcal{G}\setminus\{\alpha\};\mu_2}\, \mathsf{M}_{\mu_2\alpha}\right]^{-1} \tag{6.27b}$$

where m *is the length of the simple cycle* $(\alpha\mu_2\cdots\mu_m\alpha) \in C_{\mathcal{G}_0;\alpha}$. □.

The quantity $\mathsf{F}_{\mathcal{G};\alpha}$ is a matrix-valued continued fraction that corresponds to an effective weight associated with vertex α. If α has no neighbours in $\mathcal{G}$, then $\mathsf{F}_{\mathcal{G};\alpha} = [\mathsf{I} - x(\mathsf{I}-\mathsf{M}_\alpha)]^{-1}$ is the sum of the weights of all sequences of loops off α on $\mathcal{G}$.

The path-sum expression of Theorem 6.2.4 is essentially the well-known integral relation for the matrix logarithm [165, 166, 167]

$$\log \mathsf{M} = \int_0^1 \mathrm{d}x\, (\mathsf{M}-\mathsf{I})\big[x(\mathsf{M}-\mathsf{I})+\mathsf{I}\big]^{-1} \tag{6.28}$$

with the integrand expressed as a path sum. However, the proof of Theorem 6.2.4 that we present in the next section does not make explicit use of Eq. (6.28).

6.3 Proofs of path-sum expressions for common matrix functions

In this section we prove the path-sum results presented earlier without proof. We begin by proving the results of §6.1.2 relating the partitions of M^k and $f(\mathsf{M})$ to the partition of M. We then prove the path-sum results for matrix functions given in §6.2.

6.3.1 Partitions of matrix powers and functions

Consider an element $\mathsf{M}_{\omega\alpha} = \mathsf{R}_\omega \mathsf{M}^k \mathsf{R}_\alpha^{\mathrm{T}}$ of the general partition of M^k. On inserting the identity in the form of the closure relation over projectors (Eq. (6.2b)) between

each appearance of M in the product, and using $\mathsf{P}_\mu = \mathsf{R}_\mu^{\mathrm{T}}\mathsf{R}_\mu$, we obtain

$$\begin{aligned}\left(\mathsf{M}^k\right)_{\omega\alpha} &= \sum_{\eta_k,\ldots,\eta_2} \mathsf{R}_\omega\,\mathsf{M}\,\mathsf{R}_{\eta_k}^{\mathrm{T}}\,\mathsf{R}_{\eta_k}\,\mathsf{M}\cdots\mathsf{M}\,\mathsf{R}_{\eta_2}^{\mathrm{T}}\,\mathsf{R}_{\eta_2}\,\mathsf{M}\,\mathsf{R}_\alpha^{\mathrm{T}} \\ &= \sum_{\eta_k,\ldots,\eta_2} \mathsf{M}_{\omega\eta_k}\cdots\mathsf{M}_{\eta_3\eta_2}\,\mathsf{M}_{\eta_2\alpha}, \end{aligned} \tag{6.29}$$

which proves Eq. (6.13). This expression describes matrix multiplication in terms of the partition of M, and provides an explicit description of which pieces of M contribute to a given piece of M^k. It follows that the elements of the partition of a matrix function $f(\mathsf{M})$ with power series

$$f(\mathsf{M}) = \sum_{k=0}^{\infty} c_k\,\mathsf{M}^k \tag{6.30}$$

are given by

$$f(\mathsf{M})_{\omega\alpha} = \sum_{k=0}^{\infty} c_k \sum_{\eta_k,\ldots,\eta_2} \mathsf{M}_{\omega\eta_k}\cdots\mathsf{M}_{\eta_3\eta_2}\,\mathsf{M}_{\eta_2\alpha}. \tag{6.31}$$

This expression relates the partition of $f(\mathsf{M})$ to that of M, and proves Eq. (6.14).

6.3.2 A matrix raised to a complex power

Proof. In order to prove Theorem 6.2.1 we start from the power series

$$\mathsf{M}^q = \sum_{n=0}^{\infty} \binom{q}{n} (\mathsf{M}-\mathsf{I})^n, \tag{6.32}$$

where q is an arbitrary complex number and $\binom{q}{n} = q^{\underline{n}}/n!$ is a binomial coefficient, with $q^{\underline{n}} = q(q-1)\cdots(q-n+1)$ the falling factorial. Since the infinite sum only converges when $\|\mathsf{M}-\mathsf{I}\| \leq 1$, we assume this inequality in what follows. However, the final result can be extended to matrices of arbitrary norm by analytic continuation, and the result of Theorem 6.2.1 is therefore valid for all matrices, regardless of norm. By applying Eq. (6.14) to Eq. (6.32) we find that the elements of $\{(\mathsf{M}^q)_{\mu\nu}\}$ are given by

$$\left(\mathsf{M}^q\right)_{\omega\alpha} = \sum_{k=0}^{\infty} \binom{q}{k} \sum_{W_{\mathcal{G};\alpha\omega;k}} \bar{\mathsf{M}}_{\omega\eta_k}\cdots\bar{\mathsf{M}}_{\eta_3\eta_2}\bar{\mathsf{M}}_{\eta_2\alpha}, \tag{6.33}$$

where we have introduced the auxiliary matrix $\bar{\mathsf{M}} = \mathsf{M} - \mathsf{I}$, and $\mathcal{G}$ is the graph of $\{\bar{\mathsf{M}}_{\mu\nu}\}$. We now recast this expression in order to make any loops present in each walk appear explicitly. To this end, we note that any walk can be decomposed into a loopless walk and a collection of loops. Specifically, a walk w with vertex string $(\alpha\eta_2\cdots\eta_n\omega)$ can be represented by a vertex string $(\alpha\mu_2\cdots\mu_m\omega)$ satisfying $\mu_i \neq \mu_{i+1}$, together with a collection of $m+1$ 'loop counts' $p_1, p_2, \ldots, p_{m+1}$, where $p_i \in \{0,1,2,\ldots\}$ is the number of times that w traverses the loop $(\mu_i\mu_i)$ off vertex μ_i. Using this result to split the sum over walks into a sum over loopless walks and a sum over loops, we rewrite Eq. (6.33) as

$$\big(\mathsf{M}^q\big)_{\omega\alpha} = \sum_{n=0}^{\infty}\binom{q}{n}\sum_{m=0}^{n}\sum_{W_{\mathcal{G}_0;\alpha\omega;m}}\sum_{\{p_i\}\vdash n-m}\big(\bar{\mathsf{M}}_{\omega}\big)^{p_{m+1}}\bar{\mathsf{M}}_{\omega\mu_m}\cdots\big(\bar{\mathsf{M}}_{\mu_2}\big)^{p_2}\bar{\mathsf{M}}_{\mu_2\alpha}\big(\bar{\mathsf{M}}_{\alpha}\big)^{p_1}, \tag{6.34}$$

where the notation on the final sum indicates that the loop summation runs over all possible distributions of $n-m$ loops among the $m+1$ vertices of the loopless walk $(\alpha\mu_2\cdots\mu_m\omega) \in W_{\mathcal{G}_0;\alpha\omega}$. Mathematically, this corresponds to summing over all sequences of loop counts $p_1, p_2, \ldots, p_{m+1}$ satisfying $p_i \in \{0,1,2,\ldots\}$ and $\sum_{i=1}^{m+1} p_i = n-m$, subject to the restriction that p_i is fixed to zero for any loopless vertex μ_i. The set of loop counts $\{p_i\}$ form a weak composition of $n-m$.

We now note that for any such weak composition, and for arbitrary complex q, the following identity holds:

$$\begin{aligned}\binom{q}{n} = \sum_{k_m}\sum_{k_{m-1}=0}^{k_m}\cdots\sum_{k_1=0}^{k_2}\frac{(-1)^m}{\prod_{i=1}^{m+1}p_i!}(-1)^{p_{m+1}}\big((-q-1)-k_m+p_{m+1}\big)^{\underline{p_{m+1}}}\cdots \\ \cdots(-1)^{p_2}(k_2-k_1+p_2)^{\underline{p_2}}\,(-1)^{p_1}(k_1+p_1)^{\underline{p_1}},\end{aligned} \tag{6.35}$$

where $k^{\underline{p}} = k(k-1)\cdots(k-p+1)$ is a falling factorial, and the first sum is an indefinite sum to be evaluated at $k_m = -q-1$. From now on we will denote this by $\sum_{k_m=0}^{-q-1}$. Equation (6.35), which is independent of the value of each individual p_i, may be proved by induction on m. Upon substituting this relation into Eq. (6.34)

and rearranging the order of the summations we obtain

$$\begin{aligned}\big(\mathsf{M}^q\big)_{\omega\alpha} = \sum_{m=0}^{\infty}(-1)^m \sum_{W_{\mathcal{G}_0;\alpha\omega;m}} \sum_{\{p_i\}=0}^{\infty} \sum_{k_m=0}^{-q-1} \sum_{k_{m-1}=0}^{k_m} \cdots \sum_{k_1=0}^{k_2} (-\bar{\mathsf{M}}_\omega)^{p_{m+1}} \\ \times \big((-q-1)-k_m+p_{m+1}\big)^{\underline{p_{m+1}}}\, \bar{\mathsf{M}}_{\omega\mu_m} \cdots (-\bar{\mathsf{M}}_{\mu_2})^{p_2}\, (k_2-k_1+p_2)^{\underline{p_2}} \\ \times\, \bar{\mathsf{M}}_{\mu_2\alpha}\, (-\bar{\mathsf{M}}_\alpha)^{p_1}\, (k_1+p_1)^{\underline{p_1}}.\end{aligned} \tag{6.36}$$

We evaluate the contributions from the infinite loop sums in closed form by noting that

$$\sum_{p_i=0}^{\infty} (-\bar{\mathsf{M}}_\mu)^{p_i}\, \frac{(k_i-k_{i-1}+p_i)^{\underline{p_i}}}{p_i!} = \big(\mathsf{M}_\mu\big)^{-(k_i-k_{i-1})-1}, \tag{6.37}$$

where we have used the fact that $\|\bar{\mathsf{M}}_\mu\| = \|\mathsf{M}_\mu - \mathsf{I}\| \leq \|\mathsf{M}-\mathsf{I}\| < 1$ to ensure that the sum converges. Inserting Eq. (6.37) into Eq. (6.36), we obtain

$$\begin{aligned}\big(\mathsf{M}^q\big)_{\omega\alpha} = \sum_{m=0}^{\infty}(-1)^m \sum_{W_{\mathcal{G}_0;\alpha\omega;m}} \sum_{k_m=0}^{-q-1} \sum_{k_{m-1}=0}^{k_m} \cdots \sum_{k_1=0}^{k_2} (\mathsf{M}_\omega)^{-((-q-1)-k_m)-1} \mathsf{M}_{\omega\mu_m} \cdots \\ \cdots (\mathsf{M}_{\mu_2})^{-(k_2-k_1)-1} \mathsf{M}_{\mu_2\alpha} (\mathsf{M}_\alpha)^{-k_1-1},\end{aligned} \tag{6.38}$$

where we have used the fact that $\bar{\mathsf{M}}_{\mu\nu} = \mathsf{M}_{\mu\nu}$ to get rid of the auxiliary matrix $\bar{\mathsf{M}}$. Equation (6.38) is an m-fold nested discrete convolution. In order to convert this to a product, we take the unilateral Z-transform of the above expression with respect to the index $n \equiv -q-1$. The result is

$$\begin{aligned}\big(\mathsf{M}^q\big)_{\omega\alpha} = -\mathcal{Z}^{-1}\Bigg\{\sum_{m=0}^{\infty} \sum_{W_{\mathcal{G}_0;\alpha\omega;m}} \big[\mathsf{I}z^{-1}-\mathsf{M}_\omega\big]^{-1} \mathsf{M}_{\omega\mu_m} \cdots \\ \cdots \big[\mathsf{I}z^{-1}-\mathsf{M}_{\mu_2}\big]^{-1} \mathsf{M}_{\mu_2\alpha} \big[\mathsf{I}z^{-1}-\mathsf{M}_\alpha\big]^{-1}\Bigg\}\,[n]\Big|_{n=-q-1},\end{aligned} \tag{6.39}$$

where $z \in \mathbb{C}$ is the complex Z-domain variable. This equation has the following interpretation. The matrix $(\mathsf{M}^q)_{\omega\alpha}$, which was originally expressed as the sum of weights of walks on the graph $\mathcal{G}$ (Eq. (6.33)), has been written as a sum of weights of loopless walks (i.e. walks on the loopless graph $\mathcal{G}_0$) by assigning an effective weight of $\big[\mathsf{I}z^{-1}-\mathsf{M}_\mu\big]^{-1}$ to each vertex μ of $\mathcal{G}_0$. This effective weight corresponds to the dressing of μ by the sum of the weights of all possible sequences of loops off

μ (see Eq. (6.37)).

Following this manipulations, the result of Theorem 5.3.2 can be applied to Eq. (6.39) to convert the sum over loopless walks to a sum over paths. We obtain

$$\left(\mathsf{M}^q\right)_{\omega\alpha} = -\mathcal{Z}^{-1}\left\{\sum_{P_{\mathcal{G}_0;\alpha\omega}} \mathsf{F}_{\mathcal{G}\setminus\{\alpha,\nu_2,\ldots,\nu_\ell\};\omega}\,\mathsf{M}_{\omega\nu_\ell}\,\cdots\,\mathsf{F}_{\mathcal{G}\setminus\{\alpha\};\nu_2}\,\mathsf{M}_{\nu_2\alpha}\,\mathsf{F}_{\mathcal{G};\alpha}\right\}[n]\Big|_{n=-q-1}, \tag{6.40a}$$

where $\mathcal{G}$ is the graph of $\{(\mathsf{M}-\mathsf{I})_{\mu\nu}\}$, ℓ is the length of the path $(\alpha\nu_2\cdots\nu_\ell\omega) \in P_{\mathcal{G}_0;\alpha\omega}$, and $\mathsf{F}_{\mathcal{G};\alpha}$ is an effective vertex weight given by

$$\mathsf{F}_{\mathcal{G};\alpha} = \left[\mathsf{I}z^{-1} - \mathsf{M}_\alpha - \sum_{C_{\mathcal{G}_0;\alpha}} \mathsf{M}_{\alpha\mu_m}\,\mathsf{F}_{\mathcal{G}\setminus\{\alpha,\mu_2,\ldots,\mu_{m-1}\};\mu_m}\,\cdots\,\mathsf{M}_{\mu_3\mu_2}\,\mathsf{F}_{\mathcal{G}\setminus\{\alpha\};\mu_2}\,\mathsf{M}_{\mu_2\alpha}\right]^{-1}, \tag{6.40b}$$

where m is the length of the simple cycle $(\alpha\mu_2\cdots\mu_m\alpha) \in C_{\mathcal{G}_0;\alpha}$. Equation (6.40a) and (6.40b) can be interpreted as follows: the matrix $(\mathsf{M}^q)_{\omega\alpha}$ has been expressed as a sum of weights of paths on $\mathcal{G}$ by assigning an effective weight $\mathsf{F}_{\mathcal{G};\mu}$ to each vertex μ. This effective vertex weight incorporates the sum effect of the weights of all possible closed walks off μ on $\mathcal{G}$. This proves Theorem 6.2.1. ■

6.3.3 The matrix inverse

Proof. In order to prove Theorem 6.2.2, we write the matrix inverse as

$$\mathsf{M}^{-1} = \sum_{n=0}^{\infty} (\mathsf{I}-\mathsf{M})^n\,. \tag{6.41}$$

Since the sum only converges for $\|\mathsf{I}-\mathsf{M}\| < 1$, we assume this inequality in what follows. Nevertheless, the end result can be extended to matrices of arbitrary norm by analytic continuation, and Theorem 6.2.2 is therefore valid for matrices of any norm. Introducing the auxiliary matrix $\bar{\mathsf{M}} \equiv \mathsf{I}-\mathsf{M}$, we apply the result of Eq. (6.14) to the power series to obtain

$$\left(\mathsf{M}^{-1}\right)_{\omega\alpha} = \sum_{n=0}^{\infty}\sum_{W_{\mathcal{G};\alpha\omega;n}} \bar{\mathsf{M}}_{\omega\eta_n}\cdots\bar{\mathsf{M}}_{\eta_3\eta_2}\bar{\mathsf{M}}_{\eta_2\alpha}, \tag{6.42}$$

where $\mathcal{G}$ is the graph of $\{\bar{\mathsf{M}}_{\mu\nu}\}$. We now split the sum over walks on $\mathcal{G}$ into a sum over walks on the loopless graph $\mathcal{G}_0$ and a collection of sums over loops. The procedure we follow is the same as in §6.3.2, and we omit the details; the result is

$$\begin{aligned}\big(\mathsf{M}^{-1}\big)_{\omega\alpha} &= \sum_{m=0}^{\infty} \sum_{W_{\mathcal{G}_0;\alpha\omega;m}} \big[\mathsf{I}-\bar{\mathsf{M}}_{\omega}\big]^{-1}\, \bar{\mathsf{M}}_{\omega\mu_m} \cdots \big[\mathsf{I}-\bar{\mathsf{M}}_{\mu_2}\big]^{-1}\, \bar{\mathsf{M}}_{\mu_2\alpha}\, \big[\mathsf{I}-\bar{\mathsf{M}}_{\alpha}\big]^{-1} \\ &= \sum_{m=0}^{\infty} \sum_{W_{\mathcal{G}_0;\alpha\omega;m}} (-1)^m\, \mathsf{M}_{\omega}^{-1}\, \mathsf{M}_{\omega\mu_m} \cdots \mathsf{M}_{\mu_2}^{-1}\, \mathsf{M}_{\mu_2\alpha}\, \mathsf{M}_{\alpha}^{-1} \end{aligned} \tag{6.43}$$

where we have used $\bar{\mathsf{M}}_{\mu} = \mathsf{I} - \mathsf{M}_{\mu}$ and $\bar{\mathsf{M}}_{\mu\nu} = -\mathsf{M}_{\mu\nu}$ to obtain the second equality. Equation (6.43) has the following interpretation: the matrix $(\mathsf{M}^{-1})_{\omega\alpha}$ is given by a sum of weights of walks on the loopless graph $\mathcal{G}_0$, which, in addition to the edge weights, has an effective weight assigned to each vertex μ that describes the sum effect of dressing μ by all sequences of loops off it.

Finally, we apply the result of Theorem 5.3.2 to Eq. (6.43) to convert the sum over loopless walks to a sum over paths. The result is

$$\big(\mathsf{M}^{-1}\big)_{\omega\alpha} = \sum_{P_{\mathcal{G}_0;\alpha\omega}} (-1)^{\ell}\, \mathsf{F}_{\mathcal{G}\setminus\{\alpha,\nu_2,\ldots,\nu_\ell\};\omega}\, \mathsf{M}_{\omega\nu_\ell} \cdots \mathsf{F}_{\mathcal{G}\setminus\{\alpha\};\nu_2}\, \mathsf{M}_{\nu_2\alpha}\, \mathsf{F}_{\mathcal{G};\alpha}, \tag{6.44}$$

where ℓ is the length of the path $(\alpha\nu_2\cdots\nu_\ell\omega) \in P_{\mathcal{G}_0;\alpha\omega}$, and $\mathsf{F}_{\mathcal{G};\alpha}$ is an effective vertex weight given by

$$\mathsf{F}_{\mathcal{G};\alpha} = \left[\mathsf{M}_{\alpha} - \sum_{C_{\mathcal{G}_0;\alpha}} (-1)^m\, \mathsf{M}_{\alpha\mu_m}\, \mathsf{F}_{\mathcal{G}\setminus\{\alpha,\mu_2,\ldots,\mu_{m-1}\};\mu_m} \cdots \mathsf{M}_{\mu_3\mu_2}\, \mathsf{F}_{\mathcal{G}\setminus\{\alpha\};\mu_2}\, \mathsf{M}_{\mu_2\alpha}\right]^{-1}, \tag{6.45}$$

with m the length of the simple cycle $(\alpha\mu_2\cdots\mu_m\alpha) \in C_{\mathcal{G}_0;\alpha}$. This proves Theorem 6.2.2. ■

6.3.4 The matrix exponential

Proof. In order to prove Theorem 6.2.3 we start from the power series

$$\exp\big(\tau\mathsf{M}\big) = \sum_{n=0}^{\infty} \frac{\tau^n}{n!}\, \mathsf{M}^n, \tag{6.46}$$

where the sum converges regardless of the norm of M. Applying the result of Eq. (6.14) to this series gives

$$\exp\big(\tau\mathsf{M}\big)_{\omega\alpha} = \sum_{n=0}^{\infty} \frac{t^n}{n!} \sum_{W_{\mathcal{G};\alpha\omega;n}} \mathsf{M}_{\omega\eta_n} \cdots \mathsf{M}_{\eta_3\eta_2} \mathsf{M}_{\eta_2\alpha}, \tag{6.47}$$

where $\mathcal{G}$ is the graph of the partition $\{\mathsf{M}_{\mu\nu}\}$. We now split the sum over walks into a sum over loopless walks and a collection of sums over loops by following the same procedure as in §6.3.2; the result is

$$\exp\big(\tau\,\mathsf{M}\big)_{\omega\alpha} = \sum_{n=0}^{\infty} \frac{\tau^n}{n!} \sum_{m=0}^{n} \sum_{W_{\mathcal{G}_0;\alpha\omega;m}} \sum_{\{p_i\}\vdash n-m} \big(\mathsf{M}_{\omega}\big)^{p_{m+1}} \mathsf{M}_{\omega\mu_m} \cdots \big(\mathsf{M}_{\mu_2}\big)^{p_2} \mathsf{M}_{\mu_2\alpha} \big(\mathsf{M}_{\alpha}\big)^{p_1}, \tag{6.48}$$

where the final summation runs over all loop counts $p_1, p_2, \ldots, p_{m+1}$ that satisfy $p_i \in \{0, 1, 2, \ldots\}$ and $\sum_{i=1}^{m+1} p_i = n - m$, with the restriction that the loop counts on any loopless vertices are fixed to zero. Mathematically speaking, the set of loop counts form a weak composition of $n-m$. Any such weak composition satisfies the relation

$$\frac{1}{p_1!\,p_2!\cdots p_{m+1}!} \int_0^{\tau} \mathrm{d}t_m \cdots \int_0^{t_2} \mathrm{d}t_1\, (t-t_m)^{p_{m+1}} \cdots (t_2-t_1)^{p_2}\, t_1^{p_1} = \frac{\tau^n}{n!}, \tag{6.49}$$

where the integration over t_m is to be interpreted as an indefinite integral evaluated at $t_m = \tau$. This result – which does not depend on the value of each individual p_i – is straightforwardly proved by induction on m. By substituting this identity into Eq. (6.48) and rearranging the order of summations we obtain

$$\begin{aligned}
&\exp\big(\tau\mathsf{M}\big)_{\omega\alpha} = \qquad\qquad (6.50)\\
&\sum_{m=0}^{\infty} \sum_{W_{\mathcal{G}_0;\alpha\omega;m}} \sum_{\{p_i\}=0}^{\infty} \int_0^{\tau} \mathrm{d}t_m \cdots \int_0^{t_2} \mathrm{d}t_1 \frac{\big[(\tau-t_m)\mathsf{M}_{\omega}\big]^{p_{m+1}}}{p_{m+1}!} \mathsf{M}_{\omega\mu_m} \cdots \\
&\qquad\qquad \cdots \frac{\big[(t_2-t_1)\mathsf{M}_{\mu_2}\big]^{p_2}}{p_2!} \mathsf{M}_{\mu_2\alpha} \frac{\big[t_1\mathsf{M}_{\alpha}\big]^{p_1}}{p_1!} \\
&\qquad = \sum_{m=0}^{\infty} \sum_{W_{\mathcal{G}_0;\alpha\omega;m}} \int_0^{\tau} \mathrm{d}t_m \cdots \int_0^{t_2} \mathrm{d}t_1\, \mathrm{e}^{(t-t_m)\mathsf{M}_{\omega}} \mathsf{M}_{\omega\mu_m} \cdots \mathrm{e}^{(t_2-t_1)\mathsf{M}_{\mu_2}} \mathsf{M}_{\mu_2\alpha}\, \mathrm{e}^{t_1\mathsf{M}_{\alpha}}.
\end{aligned}$$

This expression is an m-fold nested convolution, and may be written as

$$\exp\big(\tau\mathsf{M}\big)_{\omega\alpha} = \sum_{m=0}^{\infty} \sum_{W_{\mathcal{G}_0;\alpha\omega;m}} \Big[f_\omega \mathsf{M}_{\omega\mu_m} * \cdots * f_{\mu_2} \mathsf{M}_{\mu_2\alpha} * f_\alpha \Big](\tau), \tag{6.51}$$

where $f_\mu(t) = \Theta(t)\exp(t\mathsf{M}_\mu)$, with $\Theta(t)$ the Heaviside function. We convert the convolution to a product by taking the Laplace transform of both sides, obtaining

$$\mathcal{L}\big[\exp(\tau\,\mathsf{M})_{\omega\alpha}\big] = \sum_{m=0}^{\infty} \sum_{W_{\mathcal{G}_0;\alpha\omega;m}} [s\mathsf{I}-\mathsf{M}_\omega]^{-1}\,\mathsf{M}_{\omega\mu_m}\cdots[s\mathsf{I}-\mathsf{M}_{\mu_2}]^{-1}\,\mathsf{M}_{\mu_2\alpha}\,[s\mathsf{I}-\mathsf{M}_\alpha]^{-1}, \tag{6.52}$$

where we have used the fact that $\mathcal{L}\big[f_\mu(t)\big] = \big[s\mathsf{I}-\mathsf{M}_\mu\big]^{-1}$. Equation (6.52) expresses $\mathcal{L}[\exp(\tau\mathsf{M})_{\omega\alpha}]$ as a sum of weights of walks on the loopless graph $\mathcal{G}_0$, where each vertex μ of $\mathcal{G}_0$ has been given an effective weight of $[s\mathsf{I}-\mathsf{M}_\mu]^{-1}$. Finally, we apply the result of Theorem 5.3.2 to convert the sum over loopless walks to a sum over paths. We obtain

$$\mathcal{L}\Big[\exp\big(t\,\mathsf{M}\big)_{\omega\alpha}\Big] = \sum_{P_{\mathcal{G}_0;\alpha\omega}} \mathsf{F}_{\mathcal{G}\setminus\{\alpha,\nu_2,\ldots,\nu_\ell\};\omega}\,\mathsf{M}_{\omega\nu_\ell}\cdots\mathsf{F}_{\mathcal{G}\setminus\{\alpha\};\nu_2}\,\mathsf{M}_{\nu_2\alpha}\,\mathsf{F}_{\mathcal{G};\alpha}, \tag{6.53}$$

where ℓ is the length of the path $(\alpha\nu_2\cdots\nu_\ell\omega) \in P_{\mathcal{G}_0;\alpha\omega}$, and $\mathsf{F}_{\mathcal{G};\alpha}$ is an effective vertex weight given by

$$\mathsf{F}_{\mathcal{G};\alpha} = \Bigg[s\mathsf{I} - \mathsf{M}_\alpha - \sum_{C_{\mathcal{G}_0;\alpha}} \mathsf{M}_{\alpha\mu_m}\,\mathsf{F}_{\mathcal{G}\setminus\{\alpha,\mu_2,\ldots,\mu_{m-1}\};\mu_m}\cdots\mathsf{F}_{\mathcal{G}\setminus\{\alpha\};\mu_2}\,\mathsf{M}_{\mu_2\alpha}\Bigg]^{-1}, \tag{6.54}$$

where m is the length of the simple cycle $(\alpha\mu_2\cdots\mu_m\omega) \in C_{\mathcal{G}_0;\alpha}$. This proves Theorem 6.2.3.

6.3.5 The matrix logarithm

In order to prove Theorem 6.2.4 we write the matrix logarithm as

$$\log\mathsf{M} = -\sum_{n=1}^{\infty} \frac{(\mathsf{I}-\mathsf{M})^n}{n}. \tag{6.55}$$

Again we assume that $\|\mathsf{I}-\mathsf{M}\| < 1$; nevertheless, the end result of this proof can be extended to matrices of arbitrary norm by analytic continuation, and Theorem

6.2.4 is therefore valid for all matrices, regardless of norm. Introducing the auxiliary matrix $\bar{\mathsf{M}} = \mathsf{I} - \mathsf{M}$, we rewrite the power series as

$$\big(\log \mathsf{M}\big)_{\omega\alpha} = -\sum_{n=1}^{\infty} \frac{1}{n} \sum_{W_{\mathcal{G};\alpha\omega;n}} \bar{\mathsf{M}}_{\omega\eta_n} \cdots \bar{\mathsf{M}}_{\eta_3\eta_2} \bar{\mathsf{M}}_{\eta_2\alpha}, \tag{6.56}$$

$$= -\sum_{n=1}^{\infty} \frac{1}{n} \sum_{m=0}^{n} \sum_{W_{\mathcal{G}_0;\alpha\omega;m}} \sum_{\{p_i\}\vdash n-m} \big(\bar{\mathsf{M}}_{\omega}\big)^{p_{m+1}} \bar{\mathsf{M}}_{\omega\mu_m} \cdots \big(\bar{\mathsf{M}}_{\mu_2}\big)^{p_2} \bar{\mathsf{M}}_{\mu_2\alpha} \big(\bar{\mathsf{M}}_{\alpha}\big)^{p_1}, \tag{6.57}$$

where $\mathcal{G}$ is the graph of the partition $\{\bar{\mathsf{M}}_{\mu\nu}\}$, and the second equality has been obtained by splitting the sum over walks into a sum over loopless walks and a collection of sums over loop counts as in the previous sections. Here the loop numbers $p_1, p_2, \ldots, p_{m+1}$ form a weak composition of $n - m$. Any such weak composition satisfies the relation

$$\int_0^1 \mathrm{d}x\, x^{m-1} x^{p_{m+1}} \cdots x^{p_2} x^{p_1} = \frac{1}{n}. \tag{6.58}$$

This identity allows the contributions from the infinite loop sums in Eq. (6.57) to be evaluated in closed form. By restructuring the double summation we obtain

$$\big(\log \mathsf{M}\big)_{\omega\alpha} = -\delta_{\omega\alpha} \int_0^1 \bar{\mathsf{M}}_{\alpha} \big[\mathsf{I} - x\bar{\mathsf{M}}_{\alpha}\big]^{-1} \mathrm{d}x \tag{6.59}$$

$$-\sum_{m=1}^{\infty} \sum_{W_{\mathcal{G}_0;\alpha\omega;m}} \int_0^1 x^{m-1} \big[\mathsf{I} - x\bar{\mathsf{M}}_{\omega}\big]^{-1} \bar{\mathsf{M}}_{\omega\mu_m} \cdots \big[\mathsf{I} - x\bar{\mathsf{M}}_{\mu_2}\big]^{-1} \bar{\mathsf{M}}_{\mu_2\alpha} \big[\mathsf{I} - x\bar{\mathsf{M}}_{\alpha}\big]^{-1} \mathrm{d}x,$$

where we have written $\big[\mathsf{I} - x\bar{\mathsf{M}}_{\mu}\big]^{-1}$ for $\sum_{p=0}^{\infty}(x\bar{\mathsf{M}}_{\mu})^p$, and $\delta_{\omega\alpha}$ is the Kronecker delta. Note that the first part of this expression – which represents contributions from walks consisting entirely of loops – has a slightly different structure to the second part, owing to the absence of the term with zero loops when $\omega = \alpha$. Similarly to previous sections, Eq. (6.59) expresses the matrix $\big(\log \mathsf{M}\big)_{\omega\alpha}$ as a sum over the weights of walks on the loopless graph $\mathcal{G}_0$, each vertex of which has an effective weight associated with it.

Finally, we apply the result of Theorem 5.3.2 to Eq. (6.59) to convert the sum

over loopless walks to a sum over paths. The result is

$$\big(\log \mathsf{M}\big)_{\omega\alpha} = \begin{cases} \displaystyle\int_0^1 \mathrm{d}x\, x^{-1}\,(\mathsf{I} - \mathsf{F}_{\mathcal{G};\alpha}) & \omega = \alpha \\ \displaystyle -\sum_{P_{\mathcal{G}_0;\alpha\omega}} \int_0^1 \mathrm{d}x\, x^{\ell-1}\, \mathsf{F}_{\mathcal{G}\setminus\{\alpha,\nu_2,\ldots,\nu_\ell\};\omega}\, \bar{\mathsf{M}}_{\omega\nu_\ell} \cdots \mathsf{F}_{\mathcal{G}\setminus\{\alpha\};\nu_2}\, \bar{\mathsf{M}}_{\nu_2\alpha}\, \mathsf{F}_{\mathcal{G};\alpha} & \omega \neq \alpha \end{cases} \tag{6.60}$$

where ℓ is the length of the path $(\alpha\nu_2\cdots\nu_\ell\omega) \in P_{\mathcal{G}_0;\alpha\omega}$, and $\mathsf{F}_{\mathcal{G};\alpha}$ is an effective vertex weight given by

$$\mathsf{F}_{\mathcal{G};\alpha} = \left[\mathsf{I} - x\bar{\mathsf{M}}_\alpha - \sum_{C_{\mathcal{G}_0};\alpha} x^m\, \bar{\mathsf{M}}_{\alpha\mu_m}\, \mathsf{F}_{\mathcal{G}\setminus\{\alpha,\ldots,\mu_{m-1}\};\mu_m} \cdots \bar{\mathsf{M}}_{\mu_3\mu_2}\, \mathsf{F}_{\mathcal{G}\setminus\{\alpha\};\mu_2}\, \bar{\mathsf{M}}_{\mu_2\alpha}\right]^{-1}, \tag{6.61}$$

where m is the length of the simple cycle $(\alpha\mu_2\cdots\mu_m\omega) \in C_{\mathcal{G}_0;\alpha}$. Theorem (6.2.4) follows immediately on making the substitution $\bar{\mathsf{M}} = \mathsf{I} - \mathsf{M}$. ■

6.4 Examples

In this section we present several numerical examples of the application of the path-sum expressions for matrix functions. We provide simple numerical examples for a matrix raised to a complex power, the matrix inverse, matrix exponential, and matrix logarithm.

6.4.1 Matrix raised to a complex power

To illustrate the result of Theorem 6.2.1 we consider raising the matrix

$$\mathsf{M} = \begin{pmatrix} -4 & 0 & -1 & 0 & -1 \\ -2 & -2 & 6 & -2 & 4 \\ 6 & 2 & 1 & -2 & 3 \\ 0 & 0 & -1 & -4 & -1 \\ -6 & -2 & -5 & 2 & -7 \end{pmatrix} \tag{6.62}$$

to an arbitrary complex power q. We have chosen this matrix since in addition to being singular (non-invertible) it is defective (non-diagonalizable), so that methods based on diagonalising M cannot be applied. Indeed, numerical methods imple-

mented by standard software packages such as MATLAB and *Mathematica* suffer from serious stability problems and return incorrect results, as can be straightforwardly checked by attempting to compute $\mathsf{M}^{1/2}$ with either of these programs.

To implement the method of path sums we work with a general partition of M onto vector spaces $V_1 = \mathrm{span}(\mathsf{v}_1, \mathsf{v}_2)$ and $V_2 = \mathrm{span}(\mathsf{v}_3, \mathsf{v}_4, \mathsf{v}_5)$, where $\mathsf{v}_1 = (1,0,0,0)^{\mathrm{T}}$, $\mathsf{v}_2 = (0,1,0,0)^{\mathrm{T}}$, etc. The corresponding graph $\mathcal{G}$ of this partition is the complete graph on two vertices with a loop on each vertex. Applying Theorem 6.2.1, we find that the elements of $\{(\mathsf{M}^q)_{\mu\nu}\}$ are given by

$$\big(\mathsf{M}^q\big)_{11} = -\mathcal{Z}^{-1}\big\{\mathsf{F}_{\mathcal{G};1}\big\}[n]\Big|_{n=-q-1}, \tag{6.63a}$$

$$\big(\mathsf{M}^q\big)_{22} = -\mathcal{Z}^{-1}\big\{\mathsf{F}_{\mathcal{G};2}\big\}[n]\Big|_{n=-q-1}, \tag{6.63b}$$

$$\big(\mathsf{M}^q\big)_{12} = -\mathcal{Z}^{-1}\big\{\mathsf{F}_{\mathcal{G}\setminus\{2\};1}\,\mathsf{M}_{12}\,\mathsf{F}_{\mathcal{G};2}\big\}[n]\Big|_{n=-q-1}, \tag{6.63c}$$

$$\big(\mathsf{M}^q\big)_{21} = -\mathcal{Z}^{-1}\big\{\mathsf{F}_{\mathcal{G}\setminus\{1\};2}\,\mathsf{M}_{21}\,\mathsf{F}_{\mathcal{G};1}\big\}[n]\Big|_{n=-q-1}. \tag{6.63d}$$

In order to evaluate $\mathsf{F}_{\mathcal{G};1}$ and $\mathsf{F}_{\mathcal{G};2}$ we note that $C_{\mathcal{G}_0;1} = \{(121)\}$ and $C_{\mathcal{G}_0;2} = \{(212)\}$, so that

$$\mathsf{F}_{\mathcal{G};1} = \big[\mathsf{I}z^{-1} - \mathsf{M}_1 - \mathsf{M}_{12}\,\mathsf{F}_{\mathcal{G}\setminus\{1\};2}\,\mathsf{M}_{21}\big]^{-1}, \tag{6.63e}$$

$$\mathsf{F}_{\mathcal{G};2} = \big[\mathsf{I}z^{-1} - \mathsf{M}_2 - \mathsf{M}_{21}\,\mathsf{F}_{\mathcal{G}\setminus\{2\};1}\,\mathsf{M}_{12}\big]^{-1} \tag{6.63f}$$

and finally

$$\mathsf{F}_{\mathcal{G}\setminus\{2\};1} = \big[\mathsf{I}z^{-1} - \mathsf{M}_1\big]^{-1}, \qquad \mathsf{F}_{\mathcal{G}\setminus\{1\};2} = \big[\mathsf{I}z^{-1} - \mathsf{M}_2\big]^{-1}. \tag{6.63g}$$

Assembling the pieces of M, evaluating the inverse Z-transform, and setting $n = -q-1$ gives

$$\mathsf{M}^q = \mathrm{i}\,(\mathrm{i}/2)^{3-2q}\begin{pmatrix} 8 & 0 & 2q & 0 & 2q \\ 8q-4 & 4 & q(q-2)-11 & 4 & q(q-2)-7 \\ -8q-4 & -4 & -q(q-2)-3 & 4 & -q(q-2)-7 \\ 0 & 0 & 2q & 8 & 2q \\ 8q+4 & 4 & q(q-2)+11 & -4 & q(q-2)+15 \end{pmatrix}. \tag{6.64}$$

This expression is valid for any complex q. Setting $q = 1/2$, we obtain

$$\mathsf{M}^{1/2} = -\frac{\mathrm{i}}{16}\begin{pmatrix} 32 & 0 & 4 & 0 & 4 \\ 0 & 16 & -47 & 16 & -31 \\ -32 & -16 & -9 & 16 & -25 \\ 0 & 0 & 4 & 32 & 4 \\ 32 & 16 & 41 & -16 & 57 \end{pmatrix}, \tag{6.65}$$

for which it is easily verified that $(\mathsf{M}^{1/2})^2 = \mathsf{M}$. Further, although M is not invertible, setting $q = -1$ in Eq. (6.64) yields the Drazin inverse of M, denoted by M^{D} [168, 169]:

$$\mathsf{M}^{\mathrm{D}} = \frac{1}{16}\begin{pmatrix} -4 & 0 & 1 & 0 & 1 \\ 6 & -2 & 4 & -2 & 2 \\ -2 & 2 & 3 & -2 & 5 \\ 0 & 0 & 1 & -4 & 1 \\ 2 & -2 & -7 & 2 & -9 \end{pmatrix}. \tag{6.66}$$

The Drazin inverse satisfies $\mathsf{M}\mathsf{M}^{\mathrm{D}}\mathsf{M} = \mathsf{M}$, $\mathsf{M}^{\mathrm{D}}\mathsf{M}\mathsf{M}^{\mathrm{D}} = \mathsf{M}^{\mathrm{D}}$ and $\mathsf{M}^{\mathrm{D}}\mathsf{M}^{q} = \mathsf{M}^{q}\mathsf{M}^{\mathrm{D}} = \mathsf{M}^{q-1}$. The path-sum formula of Theorem 6.2.1 thus naturally produces a pseudo-inverse when applied to non-invertible matrices. Further, setting $q = 0$ in Eq. (6.64) yields a left and right identity

$$\mathsf{M}^{\flat} = \frac{1}{8}\begin{pmatrix} 8 & 0 & 0 & 0 & 0 \\ -4 & 4 & -11 & 4 & -7 \\ -4 & -4 & -3 & 4 & -7 \\ 0 & 0 & 0 & 8 & 0 \\ 4 & 4 & 11 & -4 & 15 \end{pmatrix} \tag{6.67}$$

which satisfies $\mathsf{M}^{\flat}\mathsf{M}^{q} = \mathsf{M}^{q}\mathsf{M}^{\flat} = \mathsf{M}^{q}$ for any complex q, and $\mathsf{M}^{\mathrm{D}}\mathsf{M} = \mathsf{M}\mathsf{M}^{\mathrm{D}} = \mathsf{M}^{\flat}$, as expected of the Drazin inverse.

6.4.2 The matrix inverse

To illustrate the application of Theorem 6.2.2 we compute the inverse of the matrix

$$\mathsf{M} = \begin{pmatrix} \mathrm{i} & 0 & -\mathrm{i} & 0 \\ 0 & 1 & 1 & -5/2 \\ 2 & 8-\mathrm{i} & 3 & 0 \\ 0 & 4 & 0 & 2 \end{pmatrix}. \tag{6.68}$$

We use the general partition M onto vector spaces $V_1 = \mathrm{span}\big(|1\rangle, |3\rangle\big)$, $V_2 = \mathrm{span}\big(|2\rangle\big)$ and $V_3 = \mathrm{span}\big(|4\rangle\big)$ such that $V_1 \oplus V_2 \oplus V_3 = V$, giving

$$\mathsf{M}_1 = \begin{pmatrix} \mathrm{i} & -\mathrm{i} \\ 2 & 3 \end{pmatrix}, \quad \mathsf{M}_2 = 1, \quad \mathsf{M}_3 = 2, \tag{6.69}$$

$$\mathsf{M}_{12} = \begin{pmatrix} 0 \\ 8-\mathrm{i} \end{pmatrix}, \quad \mathsf{M}_{21} = \begin{pmatrix} 0 & 1 \end{pmatrix}, \quad \mathsf{M}_{23} = -5/2, \quad \mathsf{M}_{32} = 4, \tag{6.70}$$

and $\mathsf{M}_{13} = \mathsf{M}_{31} = \mathbf{0}$. The corresponding graph $\mathcal{G}$ is the linear directed graph on three vertices, with a loop on each vertex. Following Theorem 6.2.2, the diagonal elements of M^{-1} are given by

$$\big(\mathsf{M}^{-1}\big)_{11} = \mathsf{F}_{\mathcal{G};1}, \qquad \big(\mathsf{M}^{-1}\big)_{22} = \mathsf{F}_{\mathcal{G};2}, \qquad \big(\mathsf{M}^{-1}\big)_{33} = \mathsf{F}_{\mathcal{G};3}, \tag{6.71a}$$

while the off-diagonal elements are

$$\big(\mathsf{M}^{-1}\big)_{21} = -\mathsf{F}_{\mathcal{G}\setminus\{1\};2}\,\mathsf{M}_{21}\,\mathsf{F}_{\mathcal{G};1}, \qquad \big(\mathsf{M}^{-1}\big)_{12} = -\mathsf{F}_{\mathcal{G}\setminus\{2\};1}\,\mathsf{M}_{12}\,\mathsf{F}_{\mathcal{G};2}, \tag{6.71b}$$

$$\big(\mathsf{M}^{-1}\big)_{32} = -\mathsf{F}_{\mathcal{G}\setminus\{2\};3}\,\mathsf{M}_{32}\,\mathsf{F}_{\mathcal{G};2}, \qquad \big(\mathsf{M}^{-1}\big)_{23} = -\mathsf{F}_{\mathcal{G}\setminus\{3\};2}\,\mathsf{M}_{23}\,\mathsf{F}_{\mathcal{G};3}, \tag{6.71c}$$

$$\big(\mathsf{M}^{-1}\big)_{31} = \mathsf{F}_{\mathcal{G}\setminus\{1,2\};3}\,\mathsf{M}_{32}\,\mathsf{F}_{\mathcal{G}\setminus\{1\};2}\,\mathsf{M}_{21}\,\mathsf{F}_{\mathcal{G};1}, \tag{6.71d}$$

$$\big(\mathsf{M}^{-1}\big)_{13} = \mathsf{F}_{\mathcal{G}\setminus\{3,2\};1}\,\mathsf{M}_{12}\,\mathsf{F}_{\mathcal{G}\setminus\{3\};2}\,\mathsf{M}_{23}\,\mathsf{F}_{\mathcal{G};3}. \tag{6.71e}$$

The matrices $\mathsf{F}_{\mathcal{G};\alpha}$ are evaluated according to the recursive definition in Eq. (6.24b); for example

$$\begin{aligned} \mathsf{F}_{\mathcal{G};1} &= \big[\mathsf{M}_1 - \mathsf{M}_{12}\,\mathsf{F}_{\mathcal{G}\setminus\{1\};2}\,\mathsf{M}_{21}\big]^{-1} \\ &= \big[\mathsf{M}_1 - \mathsf{M}_{12}[\mathsf{M}_2 - \mathsf{M}_{23}\,\mathsf{F}_{\mathcal{G}\setminus\{1,2\};3}\,\mathsf{M}_{32}]^{-1}\mathsf{M}_{21}\big]^{-1} \\ &= \big[\mathsf{M}_1 - \mathsf{M}_{12}[\mathsf{M}_2 - \mathsf{M}_{23}\,\mathsf{M}_3^{-1}\,\mathsf{M}_{32}]^{-1}\mathsf{M}_{21}\big]^{-1}. \end{aligned}$$

Evaluating the elements of the partition and reassembling them into matrix form gives

$$\mathsf{M}^{-1} = \frac{1}{1940}\begin{pmatrix} 48-884\mathrm{i} & -700+120\mathrm{i} & 528-24\mathrm{i} & -875+150\mathrm{i} \\ -8-176\mathrm{i} & 440-20\mathrm{i} & -88+4\mathrm{i} & 550-25\mathrm{i} \\ 48+1056\mathrm{i} & -700+120\mathrm{i} & 528-24\mathrm{i} & -875+150\mathrm{i} \\ 16+352\mathrm{i} & -880+40\mathrm{i} & 176-8\mathrm{i} & -130+50\mathrm{i} \end{pmatrix}, \tag{6.72}$$

which is readily verified to be the inverse of M.

6.4.3 The matrix exponential

Since the graph-theoretic result that lies behind the matrix function path-sum expressions respects the correct ordering of the graph edges at all times, the results of Theorems 6.2.1–6.2.4 can be applied to matrices with non-commuting elements. In this section we present an example of this by evaluating the matrix exponential of a quaternionic matrix. Specifically, we calculate $\exp(\pi\mathsf{M})$, where M is the matrix

$$\mathsf{M} = \begin{pmatrix} \mathrm{i} & \mathrm{j} \\ \mathrm{k} & 1 \end{pmatrix} \tag{6.73}$$

where i, j, and k are the quaternions, which satisfy $\mathrm{i}^2 = \mathrm{j}^2 = \mathrm{k}^2 = \mathrm{ijk} = -1$. Partitioning M into its usual matrix elements and applying Theorem 6.2.3 on the resultant graph $\mathcal{G}$, we find that the Laplace transforms of the elements of the partition of $\exp(\tau\mathsf{M})$ are

$$\mathcal{L}\big[\exp(t\mathsf{M})_{11}\big] = \big(s - \mathrm{i} - \mathrm{j}\,(s-1)^{-1}\,\mathrm{k}\big)^{-1} \tag{6.74a}$$
$$\mathcal{L}\big[\exp(t\mathsf{M})_{12}\big] = \big(s-\mathrm{i}\big)^{-1}\,\mathrm{j}\,\big(s - 1 - \mathrm{k}\,(s-\mathrm{i})^{-1}\,\mathrm{j}\big)^{-1} \tag{6.74b}$$
$$\mathcal{L}\big[\exp(t\mathsf{M})_{21}\big] = \big(s-1\big)^{-1}\,\mathrm{k}\,\big(s - \mathrm{i} - \mathrm{j}\,(s-1)^{-1}\,\mathrm{k}\big)^{-1} \tag{6.74c}$$
$$\mathcal{L}\big[\exp(t\mathsf{M})_{22}\big] = \big(s - 1 - \mathrm{k}\,(s-\mathrm{i})^{-1}\,\mathrm{j}\big)^{-1}. \tag{6.74d}$$

Inverting the Laplace transforms and setting $\tau = \pi$ in the result gives

$$\exp\big(\pi\mathsf{M}\big) = -\frac{1+\mathrm{e}^{\pi}}{2}\begin{pmatrix} \mathrm{i} + \tanh\left(\frac{\pi}{2}\right) & \mathrm{j}-\mathrm{k} \\ \mathrm{k}-\mathrm{j} & \mathrm{i} + \tanh\left(\frac{\pi}{2}\right). \end{pmatrix} \tag{6.75}$$

6.4.4 The matrix logarithm

As a final example, we compute the principal logarithm of the matrix

$$\mathsf{M} = \begin{pmatrix} 4 & 1 & 1 & 2 & -1 \\ -2 & 7 & 1 & 0 & -1 \\ 0 & -1 & 5 & 2 & 1 \\ -2 & 0 & 0 & 8 & 0 \\ -2 & -4 & -4 & 6 & 6 \end{pmatrix}. \tag{6.76}$$

This matrix has only a single eigenvalue 6, which is five-fold degenerate. We partition M onto vector spaces $V_1 = \mathrm{span}(\mathsf{v}_1, \mathsf{v}_3, \mathsf{v}_4)$ and $V_2 = \mathrm{span}(\mathsf{v}_2, \mathsf{v}_5)$. The corresponding graph $\mathcal{G}$ is the complete directed graph on two vertices, with a loop on each vertex. Following Theorem 6.2.4, we have

$$\mathsf{F}_{\mathcal{G};1} = \left[\mathsf{I} - x(\mathsf{I} - \mathsf{M}_1) - x^2\, \mathsf{M}_{12}\, \mathsf{F}_{\mathcal{G}\setminus\{1\};2}\, \mathsf{M}_{21}\right]^{-1}, \tag{6.77a}$$

$$\mathsf{F}_{\mathcal{G};2} = \left[\mathsf{I} - x(\mathsf{I} - \mathsf{M}_2) - x^2\, \mathsf{M}_{21}\, \mathsf{F}_{\mathcal{G}\setminus\{2\};1}\, \mathsf{M}_{12}\right]^{-1}, \tag{6.77b}$$

$$\mathsf{F}_{\mathcal{G}\setminus\{2\};1} = \left[\mathsf{I} - x(\mathsf{I} - \mathsf{M}_1)\right]^{-1}, \tag{6.77c}$$

$$\mathsf{F}_{\mathcal{G}\setminus\{1\};2} = \left[\mathsf{I} - x(\mathsf{I} - \mathsf{M}_2)\right]^{-1}. \tag{6.77d}$$

The elements of the partition of $\log \mathsf{M}$ are then

$$(\log \mathsf{M})_{11} = \int_0^1 \mathrm{d}x\, x^{-1}\, (\mathsf{I} - \mathsf{F}_{\mathcal{G};1}), \qquad (\log \mathsf{M})_{12} = -\int_0^1 \mathrm{d}x\, \mathsf{F}_{\mathcal{G}\setminus\{2\};1}\, \mathsf{M}_{12}\, \mathsf{F}_{\mathcal{G};2},$$

$$(\log \mathsf{M})_{22} = \int_0^1 \mathrm{d}x\, x^{-1}\, (\mathsf{I} - \mathsf{F}_{\mathcal{G};2}), \qquad (\log \mathsf{M})_{21} = -\int_0^1 \mathrm{d}x\, \mathsf{F}_{\mathcal{G}\setminus\{1\};2}\, \mathsf{M}_{21}\, \mathsf{F}_{\mathcal{G};1}.$$

Reassembling these elements into matrix form gives

$$\log \mathsf{M} = \mathsf{I} \log 6 + \frac{1}{324} \begin{pmatrix} -108 & 41 & 41 & 130 & -63 \\ -126 & 42 & 42 & 41 & -65 \\ 18 & -37 & -37 & 71 & 56 \\ -108 & 5 & 5 & 112 & -9 \\ -108 & -211 & -211 & 328 & -9 \end{pmatrix}. \tag{6.78}$$

6.5 Applications to the simulation of many-body Rydberg systems

The method of path-sums is still a work in progress, and time constraints have meant that we have not had the opportunity to apply the method to obtain physical results on many-body Rydberg systems. However, a variant of the method of path-sums has already been successfully applied to study the dynamics of a Rydberg-excited Mott insulator, with system sizes of up to several thousands of atoms being readily accessible [170]. This method, which is known as the method of walk-sums, was developed by Pierre-Louis Giscard. An overview of the application of walk-sums to simulating the dynamics of quantum many-body systems is given in [171].

Part of the power of the method of path-sums arises from the use of a directed graph to encode the structure of a matrix, which allows any structure and symmetries that the matrix possesses to be easily recognised and exploited. Since the Hamiltonian for a many-body system is sparse and frequently highly structured, we believe that applying the method of path-sums to the time evolution operator $\mathsf{U}(t) = \exp(-\mathrm{i}\mathsf{H}t/\hbar)$ provides a promising new approach to the study of quantum many-body systems in any number of dimensions.

6.6 Summary and Outlook

In this chapter we introduced the method of path-sums, a novel symbolic method for analytically evaluating functions of matrices. This method is based on three main concepts: firstly, the partition of a matrix M into an ensemble of submatrices whose dimensionalities may be freely chosen; secondly, the mapping of matrix multiplication to walks on a graph $\mathcal{G}$ whose edge pattern encodes the structure of M; and thirdly, the exact closed-form resummation of certain classes of walks on $\mathcal{G}$ by dressing vertices with cycles. By combining these concepts, subarrays of various functions of M can be evaluated analytically and in closed form. Further, because the walk resummation is performed in a fashion that natively respects the ordering of edges in $\mathcal{G}$, these results are valid for matrices with non-commuting entries: for example, quaternionic matrices. We obtained path-sum expressions for four common matrix functions: a matrix raised to a complex power, the matrix inverse, matrix exponential, and matrix logarithm.

Applying the method of path-sums to the time-evolution of quantum many-

body systems forms a very interesting and important avenue of future research. In this case, the underlying graph on which the cycle resummations are performed has a clear physical interpretation: each vertex corresponds to a particular quantum state of the many-body system, and each edge corresponds to a particular physical process that takes the system from one state to another. Every edge is thus weighted by an element of the many-body Hamiltonian, and the cycle resummations that we carry out correspond in this context to a closed-form resummation of various families of transition amplitudes in the time-evolution operator $\mathsf{U}(t)$.

Computing the dynamics of collections of Rydberg-excited ultracold atoms held in an optical lattice is an ideal first step in this direction. Such systems are attractive testing grounds for the first applications of path-sums for several reasons: firstly, the symmetries present in the system typically mean that the many-body Hamiltonian and its underlying graph are highly structured, so the symbolic expressions generated by the path-sum method remain relatively short and tractable; and secondly, within the Rydberg blockade regime the system only explores a small fraction of the exponentially large number of possible many-body states. Time evolution to the energetically unfavourable portion of the Hilbert space can be neglected, which neatly separates the problem of computing the time evolution of the many-body system – for which the method of path-sums is relevant – from the separate problem of finding an efficient representation of the quantum state – for which it is not. Finally, studying such Rydberg systems means that the path-sum predictions could be checked against recent existing results [56, 58], providing a useful source of validation.

The development and study of numerical implementations of the method of path-sums is another topic of key importance for future work. In particular, since the number of cycles by which a vertex α must be dressed to form the dressed vertex $(\alpha)'_{\mathcal{G}}$ is prohibitively large if $\mathcal{G}$ is highly connected, any tractable numerical implementation of path-sums is likely to be based on a truncation of the exact continued-fraction expressions of Theorems 6.2.1–6.2.4 at some pre-defined depth. The accuracy and convergence of such approximations is a result of key interest and importance. Recent results on the relative magnitudes and decay behaviour of the entries of certain matrix functions form a promising starting point for this avenue of research [172, 173, 174, 175, 176].

Some guidance towards a suitable form for such approximations could also be provided by the context in which the method of path-sums is used: for example, each cycle by which a vertex on the graph of the many-body Hamiltonian is dressed

represents a particular physical process. The transition amplitudes for some such processes will certainly be negligible, and the corresponding cycles can be omitted from the vertex dressing without affecting the accuracy of the result significantly.

Chapter 7

Summary and Outlook

We now provide a summary of the work presented in this thesis, and indicate future directions in which each of the research topics could be profitably extended.

7.1 Radiative cascades from Rydberg states

In Chapter 2 we studied the statistics of radiative cascades from Rydberg states of rubidium atoms. We used quantum defect theory to obtain approximate wavefunctions for Rydberg states with principal quantum numbers up to $n = 40$, and used these wavefunctions to compute branching ratios for decay events from Rydberg states. We found that the decay probabilities from high Rydberg states are significantly biased towards states with $n \lesssim 10$. By carrying out Monte Carlo simulations of the cascade process, we found that the most common path taken to the ground $5S$ state consists of a 2-, 3-, or 4-photon cascade, so that the common approximation that all decay events lead directly to the ground $5S$ state is not very accurate. Instead, a full atomic level scheme should be used in cases where a quantitatively correct treatment of spontaneous emission from Rydberg states is required.

7.2 Ultra-large Rydberg dimers

In Chapter 3 we investigated the stability of diatomic molecules with ultra-large internuclear distances formed by a pair of rubidium atoms in Rydberg states. Starting

from an optical superlattice consisting of an array of isolated double-well potentials, we studied the equilibrium distance and binding energy of dimers formed by promoting a pair of atoms in neighbouring wells to sufficiently high Ryderg states that the charge distributions of the atoms in neighbouring wells overlap. By using quantum defect theory to model the Rydberg wavefunctions at distances far from the nuclear, combined with an efficient symbolic method for evaluating one- and two-centre molecular integrals, we found that the resultant molecular states are expected to have equilibrium distances of up to several hundred nanometres and binding energies of up to 10^3 GHz, several orders of magnitude larger than the binding energies of molecules stabilised solely by long-range dipole-dipole forces. Further, we computed an approximate radiative lifetime for these molecules, and found that it is several orders of magnitude longer than the time scales required to interrogate and characterise them by way of short laser pulses. However, it has recently become clear that molecular decay via autoionisation will play a more important role than radiative decay in determining the final lifetime of these Rydberg dimers; the calculation of autoionisation decay rates remains a topic for future research.

7.2.1 Future directions

There are a range of possible directions in which the work presented in Chapter 3 could be extended. Perhaps the most crucial topic is to compute of the rate of decay due to autoionisation rates, in order to better estimate the lifetime of the Rydberg dimers. As pointed out in §3.2.5, this computation would require knowledge of the molecular bound-state wavefunctions.

Another aspect that deserves further investigation and modelling is the process of excitation of a pair of ground-state atoms to a Rydberg dimer state. A complete model would include realistic experimental effects such as finite temperature and an investigation of the efficiency of dimer formation on the detuning, duration, and shape of the laser pulse.

A third interesting possibility is to investigate the application of a regular lattice of atoms excited to Rydberg states to the quantum simulation of condensed matter models. In the regime where the charge-density distributions of neighbouring atoms overlap, the valence electrons are expected to tunnel between lattice sites, mimicking the behaviour of electrons in metals. If the dominant terms governing the electron behaviour are the inter-site hopping and on-site interactions, the dy-

namics of the Rydberg electrons could be described by a Fermi-Hubbard model. The hopping and interaction terms in such a system can be computed by using the molecular integrals presented here, as demonstrated in [75]. While the experimental creation of such a state is expected to be experimentally challenging, a better understanding of the excitation dynamics and efficiency of population transfer to Rydberg states would prove valuable for understanding a suitable experimental parameter regime.

7.3 Mesoscopic crystals of Rydberg-dressed atoms

In Chapter 4 we investigated the stability of mesoscopic crystals of Rydberg-dressed atoms in the face of heating due to spontaneous emission. In the first part of the chapter, we studied the structure and melting behaviour of mesoscopic two-dimensional clusters of dipolar particles in a harmonic trap. By using Monte Carlo techniques to generate a distribution of crystal configurations in accordance with the canonical ensemble, we found that the melting temperature of these crystals is a non-monotonic function of their size, and is likely to be less than 100 nK for realistic experimental parameters.

We then analysed a Rydberg dressing scheme that has previously been proposed as a method of inducing dipolar interactions between neutral alkali atoms. By extending the radiative cascade simulations of Chapter 2 to include recoil kicks from the emitted photons, we computed the rate of heating due to spontaneous emission within the dressing scheme, and found that it was approximately a factor of two lower when the full atomic level scheme was used in place of a truncated three-level approximation. While this rate of heating is likely to threaten the stability of mesoscopic crystals of Rydberg-dressed atoms, the final word on the stability of such a crystal will depend on how strongly the motional dynamics of neighbouring atoms within the crystal are coupled.

7.3.1 Future directions

There are two main directions in which the work in this chapter could be extended.

The first extension is to investigate the interplay of the atomic motion within the crystal with the heating induced by spontaneous emission. This work would be aimed at providing a quantitative estimate of the lifetime of the crystal in the face of spontaneous emission, and would involve combining the quantum trajectory

simulations carried out here with molecular dynamics simulations of interacting dipolar atoms.

Secondly, our elementary analysis of the Rydberg dressing scheme could be extended by including aspects of the internal atomic dynamics that were neglected here. One important factor is the effect of black-body radiation on Rydberg states: it is known that black-body radiation at typical experimental temperatures can act both to redistribute the atomic population among neighbouring Rydberg states through stimulated transitions, and also photoionise atoms in a Rydberg state [107, 177]. Including these effects in an analysis of the dressing scheme would provide a more detailed picture of the feasibility of preparing mesoscopic crystalline states using Rydberg-dressed atoms.

7.4 The method of path-sums

In the latter portion of this thesis we introduced the method of path-sums, a new technique for evaluating matrix functions. The method of path-sums is based on two central concepts: firstly, a mapping between matrix multiplication and walks on directed graphs, and secondly, a universal result on the structure of such walks.

In Chapter 5 we presented this graph-theoretic result, which states that every walk on an arbitrary directed graph can be decomposed into a simple path plus a collection of recursively-nested simple cycles. This observation is similar in spirit to the decomposition of a positive integer into a product of prime numbers, and allows the basis of the path algebra of a graph to be written in a compact closed form.

In Chapter 6 we described the correspondence between matrix multiplication and walks on directed graphs, and showed that this mapping can be used to recast the evaluation of a matrix function $f(\mathsf{M})$ in terms of a sum over the weights of walks on a weighted graph whose edge structure encodes the structure of M. By using the results of Chapter 5 to resum certain families of terms appearing in this sum, we obtained exact closed-form expressions for four common matrix functions: a matrix raised to a complex power, the matrix inverse, matrix exponential, and matrix logarithm. We presented numerical examples of each of these functions, and discussed the applications of the path-sum expression for the matrix exponential to simulations of the dynamics of quantum many-body systems.

7.4.1 Future directions

The method of path-sums is very new, and consequently provides a wide range of promising avenues for future research.

As noted in Chapter 6, the use of a directed graph to encode the structure of a matrix allows any special properties of the matrix to be recognised and exploited. Since the Hamiltonian of a quantum many-body system is highly sparse, we expect that applying path-sum techniques to the evaluation of the time-evolution operator $\mathsf{U}(t) = \exp(-\mathrm{i}\mathsf{H}t/\hbar)$ will lead to interesting new approaches to the study of strongly-correlated quantum many-body systems. A variant of the path-sum method has already been used to study the dynamics of Rydberg excitations within a Mott insulator state of cold atoms in an optical lattice, yielding promising results and scaling well to systems of several thousand atoms [170, 171]. Such a lattice system would form an ideal testing ground for the application of the method of path-sums to strongly-correlated many-body systems, since the predictions can then be compared with the results of established techniques such as density matrix renormalisation group methods.

A topic of key importance in considering future applications of the method of path-sums is the development and study of practical numerical implementations of the method. As pointed out in Chapter 6, recent results on the relative magnitudes and decay behaviour of the entries of matrix functions form a promising starting point for this avenue of research, which will also benefit from interactions with mathematicians.

Several topics within the theory of path-sums are also of mathematical interest. In particular, the similarities of the path decomposition of a walk presented in Chapter 5 with the decomposition of a positive integer into a product of primes merits further exploration. A generalisation of the results of Chapter 5 to continuous graphs or graphs with multiple edges would also form an interesting extension.

Appendix A

Coulomb functions for attractive potentials

In §1.2.2 of Chapter 1, we derived the differential equation for the reduced radial wavefunction $\chi_{\varepsilon,\ell}(r)$ of a single electron moving in the Coulomb field of an idealized atomic nucleus of infinite mass and charge +e:

$$\left[\frac{\mathrm{d}^2}{\mathrm{d}r^2} - \frac{\ell(\ell+1)}{r^2} + \frac{2}{r} + 2\varepsilon\right]\chi_{\varepsilon,\ell}(r) = 0. \tag{A.1}$$

The solutions to this equation, which are known as Coulomb functions, represent the radial portions of the energy eigenfunctions of the valence electron in the Coulomb field of the nucleus. In this Appendix we provide a concise overview of Coulomb functions in the form most commonly used for atomic quantum defect theory.

A.1 The Whittaker equation and its solutions

Equation (A.1) is a special case of the Whittaker differential equation

$$\left[\frac{\mathrm{d}^2}{\mathrm{d}z^2} + \frac{\frac{1}{4} - \lambda^2}{z^2} + \frac{\kappa}{z} - \frac{1}{4}\right] w(z) = 0 \tag{A.2}$$

corresponding to $\kappa = (-2\varepsilon)^{-1/2}$, $z = 2r/\kappa$, $\lambda = \ell + 1/2$. The standard solutions to Eq. (A.2) are the Whittaker functions $M_{\kappa,\lambda}(z)$ and $W_{\kappa,\lambda}(z)$, which are defined by

$$M_{\kappa,\lambda}(z) = \mathrm{e}^{-z/2} z^{\lambda+1/2}\, M\big(\tfrac{1}{2} + \lambda - \kappa, 1 + 2\lambda, z\big), \tag{A.3a}$$

$$W_{\kappa,\lambda}(z) = \mathrm{e}^{-z/2} z^{\lambda+1/2}\, U\big(\tfrac{1}{2} + \lambda - \kappa, 1 + 2\lambda, z\big), \tag{A.3b}$$

where $M(a, b; z)$ and $U(a, b; z)$ are confluent hypergeometric functions of the first and second kinds. A full account of the mathematical properties of $M_{\kappa,\lambda}(z)$, $W_{\kappa,\lambda}(z)$, $M(a, b; z)$, and $U(a, b; z)$ may be found in standard references on special functions; see for example [178, 179, 180, 181, 182].

A.2 Coulomb functions for attractive potentials

When constructing the solutions of Eq. (A.1) from the Whittaker functions $M_{\kappa,\lambda}(z)$ and $W_{\kappa,\lambda}(z)$, it is convenient to work not with the Whittaker functions themselves, but with selected linear combinations that have more convenient analytic properties and asymptotic forms. Two suitable linear combinations are the regular and irregular Coulomb functions, denoted by $f(\varepsilon, \ell; r)$ and $h(\varepsilon, \ell; r)$ respectively. Here we provide a brief summary of the most important properties of $f(\varepsilon, \ell; r)$ and $h(\varepsilon, \ell; r)$; for full details of their development and mathematical properties, together with a discussion of alternative sets of solutions that are useful in different situations (e.g. for repulsive Coulomb potentials) we refer to the literature by Seaton [183, 184, 69, 185] or Greene *et al.* [70, 71], and references therein.

Throughout this section, ε is real, ℓ is a non-negative integer, and r is real and non-negative. Following Seaton [69, 185], we set

$$\kappa = (-2\varepsilon)^{-1/2} \equiv \begin{cases} \mathrm{i}/k & \text{for } \varepsilon > 0, \\ \nu & \text{for } \varepsilon < 0, \end{cases} \tag{A.4}$$

where k and ν are real and positive.

A.2.1 The regular Coulomb function $f(\varepsilon, \ell; r)$.

The regular Coulomb function $f(\varepsilon, \ell; r)$ is defined by

$$f(\varepsilon, \ell; r) = \frac{\kappa^{\ell+1}}{(2\ell+1)!}\, M_{\kappa,\ell+\frac{1}{2}}\left(\frac{2r}{\kappa}\right). \tag{A.5}$$

The function $f(\varepsilon,\ell;r)$ is real, and is an analytic function of each of r and ε in the intervals $0 \le r < \infty$ and $-\infty < \varepsilon < \infty$. It vanishes at the origin, and satisfies

$$\lim_{r\to 0} r^{-\ell-1}\, f(\varepsilon,\ell;r) = \frac{2^{\ell+1}}{(2\ell+1)!}. \tag{A.6}$$

For $\varepsilon > 0$, $f(\varepsilon,\ell;r)$ is given by

$$f(\varepsilon,\ell;r) = \left(\frac{2}{\pi k}\right)^{1/2} \mathrm{e}^{-\pi/2k} \left[\frac{1-\mathrm{e}^{-2\pi/k}}{A_\ell(\varepsilon)}\right]^{1/2} \mathrm{Im}\Big\{\mathrm{e}^{\mathrm{i}(\sigma_\ell(k)-\ell\pi/2)}\, W_{\mathrm{i}/k,\ell+1/2}\big(-2\mathrm{i}kr\big)\Big\}, \tag{A.7}$$

where $\sigma_\ell(k)$ is the Coulomb phase shift:

$$\sigma_\ell(k) = \arg\Gamma(\ell+1-\mathrm{i}/k), \tag{A.8}$$

and $A_\ell(\varepsilon)$ is defined by

$$A_\ell(\varepsilon) = \prod_{n=0}^{\ell}(1+2n^2\varepsilon) = \frac{\Gamma(\kappa+\ell+1)}{\kappa^{2\ell+1}\,\Gamma(\kappa-\ell)}. \tag{A.9}$$

For $\varepsilon < 0$, $f(\varepsilon,\ell;r)$ can be written as

$$f(\varepsilon,\ell;r) = (-1)^\ell \nu^{\ell+1}\left[-\frac{\cos\pi\nu}{\Gamma(\ell+1+\nu)}\,\Theta(\nu,\ell;r) + \frac{\Gamma(\nu-\ell)\sin\pi\nu}{\pi}\,\xi(\nu,\ell;r)\right], \tag{A.10}$$

where

$$\Theta(\nu,\ell;r) = W_{\nu,\ell+1/2}\left(\frac{2r}{\nu}\right), \tag{A.11a}$$

$$\xi(\nu,\ell;r) = \mathrm{Re}\left\{\mathrm{e}^{\mathrm{i}\pi\nu}\, W_{-\nu,\ell+1/2}\left(\mathrm{e}^{\mathrm{i}\pi}\frac{2r}{\nu}\right)\right\}. \tag{A.11b}$$

A.2.2 The irregular Coulomb function $h(\varepsilon,\ell;r)$.

For nonzero ε and r, the irregular Coulomb function $h(\varepsilon,\ell;r)$ is defined by

$$h(\varepsilon,\ell;r) = \frac{\Gamma(\ell+1-\kappa)}{\pi\kappa^\ell} W_{\kappa,\ell+1/2}\left(\frac{2r}{\kappa}\right) + \big[\mathrm{i}\mathcal{H}(\varepsilon) + \cot\pi\kappa\big] A_\ell(\varepsilon)\, f(\varepsilon,\ell;r), \tag{A.12}$$

where

$$\mathcal{H}(\varepsilon) = \begin{cases} [1 - \exp(2\pi/k)]^{-1} & \varepsilon > 0, \\ 0 & \varepsilon < 0. \end{cases} \tag{A.13}$$

The function $h(\varepsilon, \ell; r)$ is real, and is an analytic function of each of r and ε in the intervals $0 < r < \infty$ and $-\infty < \varepsilon < \infty$, except when $r = 0$ or $\varepsilon = 0$. It diverges at the origin, and satisfies

$$\lim_{r\to 0} r^\ell \, h(\varepsilon, \ell; r) = \frac{(2\ell)!}{\pi 2^\ell}. \tag{A.14}$$

For $\varepsilon > 0$, $h(\varepsilon, \ell; r)$ is given by

$$h(\varepsilon, \ell; r) = \left(\frac{2}{\pi k}\right)^{1/2} \mathrm{e}^{-\pi/2k} \left[\frac{A_\ell(\varepsilon)}{1 - \mathrm{e}^{-2\pi/k}}\right]^{1/2} \mathrm{Re}\Big\{\mathrm{e}^{\mathrm{i}(\sigma_\ell(k) - \ell\pi/2)} W_{\mathrm{i}/k, \ell+1/2}\big(-2\mathrm{i}kr\big)\Big\}, \tag{A.15}$$

while for $\varepsilon < 0$, $h(\varepsilon, \ell; r)$ can be written as

$$h(\varepsilon, \ell; r) = (-1)^\ell \nu^{\ell+1} A_\ell(\varepsilon) \left[\frac{\sin \pi\nu}{\Gamma(\ell + 1 + \nu)} \, \Theta(\nu, \ell; r) + \frac{\Gamma(\nu - \ell) \cos \pi\nu}{\pi} \, \xi(\nu, \ell; r)\right], \tag{A.16}$$

where $\Theta(\nu, \ell; r)$ and $\xi(\nu, \ell; r)$ are given by Eq. (A.11).

A.2.3 Asymptotic behaviour for large r.

For large $|z|$, the Whittaker function $W_{\kappa,\lambda}(z)$ has asymptotic form

$$W_{\kappa,\lambda}(z) \overset{z\to\infty}{\sim} \mathrm{e}^{-z/2} z^\kappa. \tag{A.17}$$

This relation can be used to find the asymptotic forms of $f(\varepsilon, \ell; r)$ and $h(\varepsilon, \ell; r)$ for large r. By combining Eq. (A.17) with Eqs. (A.7) and (A.15), we find that for $\varepsilon > 0$ the Coulomb functions are oscillatory for large r, with a phase difference of

$\pi/2$:

$$f(\varepsilon,\ell;r) \overset{r\to\infty}{\sim} \left(\frac{2}{\pi k}\right)^{1/2} \left[\frac{1-\mathrm{e}^{-2\pi/k}}{A_\ell(\varepsilon)}\right]^{1/2} \sin\big(\zeta_\ell(k;r)\big), \tag{A.18a}$$

$$h(\varepsilon,\ell;r) \overset{r\to\infty}{\sim} \left(\frac{2}{\pi k}\right)^{1/2} \left[\frac{A_\ell(\varepsilon)}{1-\mathrm{e}^{-2\pi/k}}\right]^{1/2} \cos\big(\zeta_\ell(k;r)\big), \tag{A.18b}$$

where $\zeta_\ell(k;r)$ is defined by

$$\zeta_\ell(k;r) = kr + \frac{1}{k}\ln 2kr - \frac{\ell\pi}{2} + \sigma_\ell(k), \tag{A.19}$$

with $\sigma_\ell(k)$ the Coulomb phase shift of Eq. (A.8). For $\varepsilon < 0$, we combine Eq. (A.17) with Eqs. (A.10) and (A.16) to obtain

$$f(\varepsilon,\ell;r) \overset{r\to\infty}{\sim} (-1)^\ell\, \nu^{\ell+1}\, \frac{\Gamma(\nu-\ell)\sin\pi\nu}{\pi} \left(\frac{2r}{\nu}\right)^{-\nu} \mathrm{e}^{r/\nu}, \tag{A.20a}$$

$$h(\varepsilon,\ell;r) \overset{r\to\infty}{\sim} (-1)^\ell\, \nu^{-\ell}\, \frac{\Gamma(\nu+\ell+1)\cos\pi\nu}{\pi} \left(\frac{2r}{\nu}\right)^{-\nu} \mathrm{e}^{r/\nu}. \tag{A.20b}$$

The functions $f(\varepsilon,\ell;r)$ and $h(\varepsilon,\ell;r)$ either grow exponentially or decay to zero as $r\to\infty$ for $\varepsilon<0$, depending on the value taken by $\nu = (-2\varepsilon)^{-1/2}$.

A.2.4 The quantum defect functions $s(\varepsilon,\ell;r)$ and $c(\varepsilon,\ell;r)$.

Finally, we define the Coulomb functions $s(\varepsilon,\ell;r)$ and $c(\varepsilon,\ell;r)$, which are forms of the regular and irregular Coulomb functions that are appropriately normalised for constructing atomic wavefunctions in quantum defect theory. We set

$$B_\ell(\varepsilon) = \begin{cases} A_\ell(\varepsilon)\big[1-\mathrm{e}^{-2\pi/k}\big]^{-1} & \varepsilon > 0 \\ A_\ell(\varepsilon) & \varepsilon \le 0, \end{cases} \tag{A.21}$$

and define the functions $s(\varepsilon,\ell;r)$ and $c(\varepsilon,\ell;r)$ by

$$s(\varepsilon,\ell;r) = 2^{1/2} B(\varepsilon,\ell)^{1/2}\, f(\varepsilon,\ell;r), \tag{A.22a}$$

$$c(\varepsilon,\ell;r) = 2^{-1/2} B(\varepsilon,\ell)^{-1/2}\, h(\varepsilon,\ell;r). \tag{A.22b}$$

Note that s and c are only real for $\varepsilon > -1/\ell^2$, $\nu > \ell$ [185]. For $\varepsilon > 0$, the asymptotic forms of s and c are

$$s(\varepsilon, \ell; r) \overset{r\to\infty}{\sim} (\pi k)^{-1/2} \sin\big(\zeta_\ell(k; r)\big), \tag{A.23a}$$

$$c(\varepsilon, \ell; r) \overset{r\to\infty}{\sim} (\pi k)^{-1/2} \cos\big(\zeta_\ell(k; r)\big). \tag{A.23b}$$

For $\varepsilon < 0$, s and c can be written as

$$s(\varepsilon, \ell; r) = (-1)^\ell \left[\frac{\sin \pi\nu}{\pi (2\nu)^{1/2} K(\nu, \ell)} \, \xi(\nu, \ell; r) - \cos \pi\nu \left(\frac{\nu^3}{2} \right)^{1/2} K(\nu, \ell) \, \Theta(\nu, \ell; r) \right], \tag{A.24a}$$

$$c(\varepsilon, \ell; r) = (-1)^\ell \left[\frac{\cos \pi\nu}{\pi (2\nu)^{1/2} K(\nu, \ell)} \, \xi(\nu, \ell; r) + \sin \pi\nu \left(\frac{\nu^3}{2} \right)^{1/2} K(\nu, \ell) \, \Theta(\nu, \ell; r) \right], \tag{A.24b}$$

where

$$K(\nu, \ell) = \big[\nu^2 \Gamma(\nu + \ell + 1) \Gamma(\nu - \ell) \big]^{-1/2}. \tag{A.25}$$

Appendix B

Spontaneous emission in hydrogenic atoms

An atom in an excited state is unstable: due to the coupling between the atom and the modes of the quantized electromagnetic field, the atom decays to a lower energy level, and a photon is emitted. In this Appendix, we present a summary of the theory of spontaneous emission in hydrogenic atoms, with a focus on calculating the rate at which spontaneous emission occurs and the angular distribution of the emitted photons. We follow the treatment of Cohen-Tannoudji *et al.* [142], where further details can be found.

B.1 Emission characteristics of a single transition

Consider a hydrogenic atom in a state with quantum numbers (n_i, ℓ_i, m_i), energy E_i, and wavefunction $\psi_{n_i,\ell_i,m_i}(\mathbf{r})$. The probability per unit time per unit solid angle for this atom to emit a photon with polarization $\boldsymbol{\varepsilon}$ and decay to the state (n_f, ℓ_f, m_f) with energy E_f and wavefunction $\psi_{n_f,\ell_f,m_f}(\mathbf{r})$, as predicted by time-dependent perturbation theory, is [142]

$$\Gamma^{n_f,\ell_f,m_f}_{n_i,\ell_i,m_i}(\theta,\phi;\boldsymbol{\varepsilon}) = \frac{\omega_{if}^3 q^2}{8\pi^2\varepsilon_0\hbar c^3}\left|\mathbf{r}^{n_f,\ell_f,m_f}_{n_i,\ell_i,m_i}\cdot\boldsymbol{\varepsilon}\right|^2 \tag{B.1}$$

where $\omega_{if} = (E_i - E_f)/\hbar$ is the energy difference measured in frequency units, $q = -e$ is the electronic charge, ε_0 is the permittivity of free space, c is the speed of

light, and $\mathbf{r}_{n_i,\ell_i,m_i}^{n_f,\ell_f,m_f}$ is the dipole matrix element between the initial and final states, defined by

$$\mathbf{r}_{n_i,\ell_i,m_i}^{n_f,\ell_f,m_f} = \int \mathrm{d}^3\mathbf{r}\, \psi^*_{n_f,\ell_f,m_f}(\mathbf{r})\, \mathbf{r}\, \psi_{n_i,\ell_i,m_i}(\mathbf{r}). \tag{B.2}$$

B.1.1 Evaluating the dipole matrix element

To evaluate the dipole matrix elements we decompose the energy eigenfunction $\psi_{n,\ell,m}(\mathbf{r})$ into a radial and an angular piece:

$$\psi_{n,\ell,m}(\mathbf{r}) = \frac{\chi_{n,\ell}(r)}{r}\, Y_\ell^m(\theta,\phi). \tag{B.3}$$

By substituting this expression into Eq. (B.2) and writing the position operator for the electron as $\mathbf{r} = r\hat{\mathbf{r}}$, we find that the dipole matrix element is given by

$$\mathbf{r}_{n_i,\ell_i,m_i}^{n_f,\ell_f,m_f} = \mathcal{R}_{n_i,\ell_i}^{n_f,\ell_f}\, \boldsymbol{\mathcal{A}}_{\ell_i,m_i}^{\ell_f,m_f}, \tag{B.4}$$

where $\mathcal{R}_{n_i,\ell_i}^{n_f,\ell_f}$ arises from the overlap of the radial wavefunctions, and $\boldsymbol{\mathcal{A}}_{\ell_i,m_i}^{\ell_f,m_f}$ contains the contribution from the overlap of the angular pieces:

$$\mathcal{R}_{n_i,\ell_i}^{n_f,\ell_f} = \int_0^\infty \mathrm{d}r\, \chi^*_{n_f,\ell_f}(r)\, r\, \chi_{n_i,\ell_i}(r), \tag{B.5a}$$

$$\boldsymbol{\mathcal{A}}_{\ell_i,m_i}^{\ell_f,m_f} = \int \mathrm{d}\Omega \left[Y_{\ell_f}^{m_f}(\theta,\phi)\right]^*\, \hat{\mathbf{r}}\, Y_{\ell_i}^{m_i}(\theta,\phi). \tag{B.5b}$$

Since the quantity $\mathcal{R}_{n_i,\ell_i}^{n_f,\ell_f}$ depends on the reduced radial wavefunctions $\chi_{n,\ell}(r)$, it depends on the exact form of the potential seen by the valence electron. On the other hand, the angular factor $\boldsymbol{\mathcal{A}}_{\ell_i,m_i}^{\ell_f,m_f}$ is independent of the radial form of the potential, and is the same for any central potential. To evaluate it, we write the radial unit vector as

$$\hat{\mathbf{r}} = \sqrt{\frac{4\pi}{3}} \left[Y_1^{-1}(\theta,\phi)\, \hat{\mathbf{e}}_+ + Y_1^0(\theta,\phi)\, \hat{\mathbf{e}}_0 - Y_1^1(\theta,\phi)\, \hat{\mathbf{e}}_-\right], \tag{B.6}$$

where the circular basis vectors $\hat{\mathbf{e}}_\pm, \hat{\mathbf{e}}_0$ are defined by $\hat{\mathbf{e}}_\pm = (\hat{\mathbf{x}} \pm \mathrm{i}\hat{\mathbf{y}})/\sqrt{2}$ and $\hat{\mathbf{e}}_0 = \hat{\mathbf{z}}$. Using the spherical harmonic relation $\left[Y_\ell^m(\theta,\phi)\right]^* = (-1)^m\, Y_\ell^m(\theta,\phi)$ and Gaunt's

integral

$$\int Y_{\ell_1}^{m_1} Y_{\ell_2}^{m_2} Y_{\ell_3}^{m_3} \,\mathrm{d}\Omega = \sqrt{\frac{(2\ell_1+1)(2\ell_2+1)(2\ell_3+1)}{4\pi}} \begin{pmatrix} \ell_1 & \ell_2 & \ell_3 \\ 0 & 0 & 0 \end{pmatrix} \begin{pmatrix} \ell_1 & \ell_2 & \ell_3 \\ m_1 & m_2 & m_3 \end{pmatrix},$$

where the bracketed objects on the right-hand side are Wigner 3-j symbols, we find

$$\boldsymbol{\mathcal{A}}_{\ell_i,m_i}^{\ell_f,m_f} = \begin{cases} \mathcal{A}_{\ell_i,m_i}^{(\Delta\ell,\Delta m)}\, \hat{\mathbf{e}}_{-\Delta m} & \text{if } \Delta\ell = \pm 1 \text{ and } \Delta m = 0 \text{ or } \pm 1, \\ 0 & \text{otherwise,} \end{cases} \tag{B.7}$$

where $\Delta\ell = \ell_f - \ell_i$, $\Delta m = m_f - m_i$, and

$$\mathcal{A}_{\ell_i,m_i}^{(-1,-1)} = -\sqrt{\frac{(\ell_i+m_i-1)(\ell_i+m_i)}{2(2\ell_i-1)(2\ell_i+1)}}, \quad \mathcal{A}_{\ell_i,m_i}^{(+1,-1)} = \sqrt{\frac{(\ell_i-m_i+1)(\ell_i-m_i+2)}{2(2\ell_i+1)(2\ell_i+3)}},$$

$$\mathcal{A}_{\ell_i,m_i}^{(-1,0)} = \sqrt{\frac{(\ell_i-m_i)(\ell_i+m_i)}{(2\ell_i-1)(2\ell_i+1)}}, \qquad \mathcal{A}_{\ell_i,m_i}^{(+1,0)} = \sqrt{\frac{(\ell_i-m_i+1)(\ell_i+m_i+1)}{(2\ell_i+1)(2\ell_i+3)}},$$

$$\mathcal{A}_{\ell_i,m_i}^{(-1,+1)} = \sqrt{\frac{(\ell_i-m_i)(\ell_i-m_i-1)}{2(2\ell_i-1)(2\ell_i+1)}}, \quad \mathcal{A}_{\ell_i,m_i}^{(+1,+1)} = -\sqrt{\frac{(\ell_i+m_i+1)(\ell_i+m_i+2)}{2(2\ell_i+1)(2\ell_i+3)}}.$$

B.1.2 Evaluating the sum over photon polarisations

Equation (B.1) gives the rate of emission of photons with polarisation $\boldsymbol{\varepsilon}$. If the polarisation of the emitted photon is undetected or unimportant, this rate must be summed over all polarisations (i.e. over a pair of polarisation vectors orthogonal to the emission direction $\hat{\mathbf{k}}$). The rate of emission per unit solid angle of photons with arbitrary polarisation is thus

$$\Gamma_{n_i,\ell_i,m_i}^{n_f,\ell_f,m_f}(\theta,\phi) = \sum_{\boldsymbol{\varepsilon}\perp\hat{\mathbf{k}}} \Gamma_{n_i,\ell_i,m_i}^{n_f,\ell_f,m_f}(\theta,\phi;\boldsymbol{\varepsilon}). \tag{B.8}$$

A suitable (real) polarisation basis $(\hat{\varepsilon}_1, \hat{\varepsilon}_2)$ perpendicular to the emission direction $\hat{\mathbf{k}} = \sin\theta\cos\phi\,\hat{\mathbf{x}} + \sin\theta\sin\phi\,\hat{\mathbf{y}} + \cos\theta\,\hat{\mathbf{z}}$ is given by

$$\hat{\varepsilon}_1 = \sin\phi\,\hat{\mathbf{x}} - \cos\phi\,\hat{\mathbf{y}} \tag{B.9a}$$

$$\hat{\varepsilon}_2 = \cos\theta\cos\phi\,\hat{\mathbf{x}} + \cos\theta\sin\phi\,\hat{\mathbf{y}} - \sin\theta\,\hat{\mathbf{z}}, \tag{B.9b}$$

from which we define a pair of circular polarisation vectors $\hat{\varepsilon}_\pm = (\hat{\varepsilon}_1 \pm \mathrm{i}\,\hat{\varepsilon}_2)/\sqrt{2}$. The unit vectors $(\hat{\varepsilon}_\pm, \hat{\mathbf{k}})$ are related to $(\hat{\mathbf{e}}_\pm, \hat{\mathbf{e}}_0)$ through

$$\begin{pmatrix} \hat{\varepsilon}_+ \\ \hat{\varepsilon}_- \\ \hat{\mathbf{k}} \end{pmatrix} = \begin{pmatrix} \frac{\mathrm{i}}{2}\mathrm{e}{-\mathrm{i}\phi}(1+\cos\theta) & -\frac{\mathrm{i}}{2}\mathrm{e}{\mathrm{i}\phi}(1-\cos\theta) & -\frac{\mathrm{i}}{\sqrt{2}}\sin\theta \\ \frac{\mathrm{i}}{2}\mathrm{e}{-\mathrm{i}\phi}(1-\cos\theta) & -\frac{\mathrm{i}}{2}\mathrm{e}{\mathrm{i}\phi}(1+\cos\theta) & \frac{\mathrm{i}}{\sqrt{2}}\sin\theta \\ \frac{1}{\sqrt{2}}\mathrm{e}{-\mathrm{i}\phi}\sin\theta & \frac{1}{\sqrt{2}}\mathrm{e}{\mathrm{i}\phi}\sin\theta & \cos\theta \end{pmatrix} \begin{pmatrix} \hat{\mathbf{e}}_+ \\ \hat{\mathbf{e}}_- \\ \hat{\mathbf{e}}_0 \end{pmatrix}. \tag{B.10}$$

The sum over polarisations can now be evaluated; we find

$$\begin{aligned} \sum_{\boldsymbol{\varepsilon}\perp\hat{\mathbf{k}}} \left| \boldsymbol{\mathcal{A}}^{\ell_f,m_f}_{\ell_i,m_i} \cdot \boldsymbol{\varepsilon} \right|^2 &= \left[\mathcal{A}^{(\Delta\ell,\Delta m)}_{\ell_i,m_i}\right]^2 \left[\left|\hat{\mathbf{e}}_{-\Delta m} \cdot \hat{\varepsilon}_+\right|^2 + \left|\hat{\mathbf{e}}_{-\Delta m} \cdot \hat{\varepsilon}_-\right|^2 \right] \\ &= \frac{8\pi}{3}\left[\mathcal{A}^{(\Delta\ell,\Delta m)}_{\ell_i,m_i}\right]^2 f^{(\Delta m)}(\hat{\mathbf{k}}), \end{aligned} \tag{B.11}$$

where $f^{(\Delta m)}(\hat{\mathbf{k}})$ is a probability density function for the angular distribution of the emitted radiation for a transition with a given value of Δm. They are given by

$$f^{(0)}(\hat{\mathbf{k}}) = \frac{3}{8\pi}\sin^2\theta, \qquad f^{(\pm1)}(\hat{\mathbf{k}}) = \frac{3}{16\pi}(1+\cos^2\theta),$$

and are normalised over the full solid angle:

$$\int f^{(\Delta m)}(\hat{\mathbf{k}})\,\mathrm{d}\hat{\mathbf{k}} = \int_0^{2\pi}\mathrm{d}\phi \int_0^{\pi} \sin\theta\,\mathrm{d}\theta\, f^{(\Delta m)}(\theta,\phi) = 1. \tag{B.12}$$

B.1.3 Emission characteristics of a single transition

Putting together the above results gives the probability per unit time per unit solid angle for emission of a photon of arbitrary polarisation on the $(n_i,\ell_i,m_i) \to (n_f,\ell_f,m_f)$ transition as:

$$\Gamma^{n_f,\ell_f,m_f}_{n_i,\ell_i,m_i}(\theta,\phi) = \frac{\omega_{if}^3 q^2}{3\pi\varepsilon_0\hbar c^3}\left[\mathcal{R}^{n_f,\ell_f}_{n_i,\ell_i}\right]^2 \left[\mathcal{A}^{(\Delta\ell,\Delta m)}_{\ell_i,m_i}\right]^2 f^{(\Delta m)}(\theta,\phi). \tag{B.13}$$

B.2 Emission rate from a single magnetic sublevel

We now consider the total rate of decay of the magnetic sublevel (n_i,ℓ_i,m_i) into the (n_f,ℓ_f) manifold. Typically, several decay channels lead out of the state (n_i,ℓ_i,m_i), so that the total rate of decay is the sum of the individual decay rates.

B.2.1 Evaluating the sum over final states

Defining the total decay rate per unit solid angle from (n_i, ℓ_i, m_i) into the (n_f, ℓ_f) manifold as

$$\Gamma^{n_f,\ell_f}_{n_i,\ell_i,m_i}(\theta,\phi) = \sum_{m_f=m_i-1}^{m_i+1} \Gamma^{n_f,\ell_f,m_f}_{n_i,\ell_i,m_i}(\theta,\phi), \tag{B.14}$$

we find

$$\Gamma^{n_f,\ell_f}_{n_i,\ell_i,m_i}(\theta,\phi) = \frac{\omega_{if}^3 q^2}{3\pi\varepsilon_0\hbar c^3}\left[\mathcal{R}^{n_f,\ell_f}_{n_i,\ell_i}\right]^2 \times \begin{cases} \frac{\ell_i(\ell_i-1)+m_i^2}{(2\ell_i-1)(2\ell_i+1)} f^{(1)}(\theta) + \frac{\ell_i^2-m_i^2}{(2\ell_i-1)(2\ell_i+1)} f^{(0)}(\theta), & \Delta\ell = -1 \\ \frac{\ell_i(\ell_i+3)+m_i^2+2}{(2\ell_i+1)(2\ell_i+3)} f^{(1)}(\theta) + \frac{\ell_i^2-m_i^2+2\ell_i+1}{(2\ell_i+1)(2\ell_i+3)} f^{(0)}(\theta), & \Delta\ell = +1. \end{cases}$$

Since the emission pattern out of a given sublevel is spherically uniform if and only if the weight of $f_1(\theta)$ is equal to twice the weight of $f_0(\theta)$, we find that the only sublevels that have a spherically uniform emission pattern are those satisfying $3m_i^2 = \ell_i(\ell_i+1)$; (i.e. only $(0,0)$ and $(3,\pm 2)$ below $\ell = 10$). If this condition is satisfied, then both $\Delta\ell = \pm 1$ emissions are spherically uniform.

B.2.2 Integrating over the solid angle

The total decay rate from the state (n_i, ℓ_i, m_i) into the (n_f, ℓ_f) manifold is

$$\Gamma^{n_f,\ell_f}_{n_i,\ell_i,m_i} = \int \mathrm{d}\Omega\, \Gamma^{n_f,\ell_f}_{n_i,\ell_i,m_i}(\theta,\phi) = \frac{\omega_{if}^3 q^2}{3\pi\varepsilon_0\hbar c^3}\left[\mathcal{R}^{n_f,\ell_f}_{n_i,\ell_i}\right]^2 \frac{\max(\ell_i,\ell_f)}{(2\ell_i+1)}. \tag{B.15}$$

Note that this is independent of m_i. This indicates that all of the magnetic sublevels in the (n_i, ℓ_i) manifold have the same radiative lifetime, as is to be expected in the absence of any preferred direction in space.

B.3 Heating effect of spontaneous emission

Consider the emission of a photon with wavevector $\mathbf{k} = k\hat{\mathbf{k}}$ by an atom with momentum $\mathbf{p}$. Treating the atomic motion classically, the change in the kinetic energy of the atom due to the recoil is

$$\Delta E(\mathbf{k}) = \Delta E_x(\mathbf{k}) + \Delta E_y(\mathbf{k}) + \Delta E_z(\mathbf{k}), \tag{B.16}$$

where the quantity $\Delta E_\alpha(\mathbf{k})$ for $\alpha = x, y, z$ is the change in the kinetic energy due to motion in the α-direction:

$$\begin{aligned}\Delta E_\alpha(\mathbf{k}) &= \frac{\big[(\mathbf{p} - \hbar\mathbf{k}) \cdot \hat{\mathbf{e}}_\alpha\big]^2}{2m} - \frac{(\mathbf{p} \cdot \hat{\mathbf{e}}_\alpha)^2}{2m} \\ &= \frac{\hbar^2 k^2}{2m}\big(\hat{\mathbf{k}} \cdot \hat{\mathbf{e}}_\alpha\big)^2 - \frac{\hbar k}{m}\big(\mathbf{p} \cdot \hat{\mathbf{e}}_\alpha\big)\big(\hat{\mathbf{k}} \cdot \hat{\mathbf{e}}_\alpha\big). \end{aligned} \tag{B.17}$$

Let the emission direction of the photon be distributed according to the probability density $g(\hat{\mathbf{k}})$, which is normalised such that

$$\int \mathrm{d}\hat{\mathbf{k}}\, g(\hat{\mathbf{k}}) = 1. \tag{B.18}$$

Then the average change in the kinetic energy of the atom per photon emitted is

$$\big\langle \Delta E(\mathbf{k}) \big\rangle = \big\langle \Delta E_x(\mathbf{k}) \big\rangle + \big\langle \Delta E_y(\mathbf{k}) \big\rangle + \big\langle \Delta E_z(\mathbf{k}) \big\rangle, \tag{B.19}$$

where

$$\big\langle \Delta E_\alpha(\mathbf{k}) \big\rangle = \int \mathrm{d}\hat{\mathbf{k}}\, \Delta E_\alpha(\mathbf{k})\, g(\hat{\mathbf{k}}). \tag{B.20}$$

It is typically the case that $g(\hat{\mathbf{k}})$ is an even function about the origin; i.e. $g(\hat{\mathbf{k}}) = g(-\hat{\mathbf{k}})$. Since $\big(\hat{\mathbf{k}} \cdot \hat{\mathbf{e}}_\alpha\big)$ is odd, it follows that

$$\int \mathrm{d}\hat{\mathbf{k}}\, \big(\hat{\mathbf{k}} \cdot \hat{\mathbf{e}}_\alpha\big)\, g(\hat{\mathbf{k}}) = 0, \tag{B.21}$$

and so from Eqs. (B.17) and (B.20) we find

$$\big\langle \Delta E_\alpha(\mathbf{k}) \big\rangle = \frac{\hbar^2 k^2}{2m}\beta_\alpha, \tag{B.22}$$

where β_α is the fraction of the kinetic energy that is added in the α-direction:

$$\beta_\alpha = \int \mathrm{d}\hat{\mathbf{k}}\, \big(\hat{\mathbf{k}} \cdot \hat{\mathbf{e}}_\alpha\big)^2 g(\hat{\mathbf{k}}). \tag{B.23}$$

Note that it follows from the normalization of $g(\hat{\mathbf{k}})$ that $\beta_x + \beta_y + \beta_z = 1$.

B.3.1 Uniform emission

In the case that the emitted photons are uniformly distributed over the full solid angle, the angular distribution function is $g(\hat{\mathbf{k}}) = 1/(4\pi)$. In this case it is straightforward to check that

$$\beta_x = \beta_y = \beta_z = \frac{1}{3}, \tag{B.24}$$

so that the increase in kinetic energy is shared equally among the x, y, and z directions.

B.3.2 Emission on a $\Delta m = 0$ transition

If the emitted photons originate from a transition with $\Delta m = 0$, the angular distribution function is $g(\hat{\mathbf{k}}) = f^{(0)}(\hat{\mathbf{k}}) = 3\sin^2\theta/(8\pi)$, so that

$$\beta_x = \beta_y = \frac{2}{5}, \qquad \beta_z = \frac{1}{5}. \tag{B.25}$$

The atomic motion in the x-y plane is heated more strongly than the motion in the z-direction, reflecting the preferential spontaneous emission in this plane.

B.3.3 Emission on a $\Delta m = \pm 1$ transition

For emitted photons originating from a transition with $\Delta m = \pm 1$, the angular distribution function is $g(\hat{\mathbf{k}}) = f^{(\pm 1)}(\hat{\mathbf{k}}) = 3(1 + \cos^2\theta)/(16\pi)$. In this case the heating coefficients are

$$\beta_x = \beta_y = \frac{3}{10}, \qquad \beta_z = \frac{2}{5}. \tag{B.26}$$

Appendix C

Quantum trajectory simulations of a master equation

In many cases of interest, the dynamics of a quantum system coupled to its environment are accurately described by a master equation for the system density matrix $\rho(t)$ of the form

$$\mathrm{i}\hbar\frac{\mathrm{d}\rho}{\mathrm{d}t} = \big[H,\rho\big] + \frac{\mathrm{i}\hbar}{2}\sum_{\alpha}\gamma_{\alpha}\big(2a_{\alpha}\rho\,a_{\alpha}^{\dagger} - a_{\alpha}^{\dagger}a\,\rho - \rho\,a_{\alpha}^{\dagger}a\big) \tag{C.1}$$

where α is an index labelling the decay channels of the system, a_{α} is a system operator, and γ_{α} is the decay rate for channel α. By flattening the density matrix ρ into a vector, this set of N^2 coupled differential equations can be written as

$$\frac{\mathrm{d}\boldsymbol{\rho}}{\mathrm{d}t} = \mathbf{M}\boldsymbol{\rho} \tag{C.2}$$

where $\boldsymbol{\rho}$ is a vector of length N^2 and $\mathbf{M}$ is an $N^2\times N^2$ matrix. If the number of basis states of the system is small, it is possible to construct and solve this set of equations directly; however, as N increases this rapidly becomes infeasible. A more efficient approach is to compute an approximate density matrix for the system by carrying out quantum jump simulations of Eq. (C.1) (see e.g. [143, 144, 145, 146, 147]). A suitable algorithm is [144]:

1. Initialise the system state to $|\phi(t=0)\rangle$.

2. Draw a random number r from the uniform distribution on $[0, 1]$ and evolve the atomic state vector according to the Schrödinger equation

$$i\hbar\frac{\mathrm{d}|\phi(t)\rangle}{\mathrm{d}t} = H_{\mathrm{eff}}|\phi(t)\rangle \tag{C.3}$$

where

$$H_{\mathrm{eff}} = H - \frac{\mathrm{i}\hbar}{2}\sum_{\alpha}\gamma_{\alpha}a_{\alpha}^{\dagger}a_{\alpha} \tag{C.4}$$

until $t = t_1$, where t_1 is determined by the condition $\langle\phi(t_1)|\phi(t_1)\rangle = r$.

3. Select among the various types of quantum jumps according to the conditional probabilities

$$p(\alpha|t) = \frac{p(t,\alpha)}{\sum_{\alpha}p(t,\alpha)}, \qquad \text{where} \qquad p(t,\alpha) = \gamma_{\alpha}\langle\phi(t)|a_{\alpha}^{\dagger}a_{\alpha}|\phi(t)\rangle. \tag{C.5}$$

4. Having selected a particular decay channel α_n, update the system state as

$$|\phi(t_1^+)\rangle = \frac{\sqrt{\gamma_{\alpha_n}}a_{\alpha_n}|\phi(t_1^-)\rangle}{\sqrt{\langle\phi(t_1^-)|\,\gamma_{\alpha_n}a_{\alpha_n}^{\dagger}a_{\alpha_n}|\phi(t_1^-)\rangle}} \tag{C.6}$$

and continue evolving the state until the next quantum jump occurs (see Step 2).

5. An approximation for the system density matrix is given by

$$\rho(t) \approx \left\langle\!\!\left\langle \frac{|\phi(t)\rangle\langle\phi(t)|}{\langle\phi(t)|\phi(t)\rangle} \right\rangle\!\!\right\rangle \tag{C.7}$$

where the angled brackets denote an average over different realizations of the system wavefunction.

Bibliography

[1] Claude N. Cohen-Tannoudji, *Nobel lecture: Manipulating atoms with photons*, Rev. Mod. Phys. **70**, 707–719 (1998).

[2] Steven Chu, *Nobel lecture: The manipulation of neutral particles*, Rev. Mod. Phys. **70**, 685–706 (1998).

[3] William D. Phillips, *Nobel lecture: Laser cooling and trapping of neutral atoms*, Rev. Mod. Phys. **70**, 721–741 (1998).

[4] H. J. Metcalf and P. van der Straten, **Laser Cooling and Trapping** (Springer, 1999).

[5] J. Ye, S. Blatt, M. M. Boyd, S. M. Foreman, E. R. Hudson, T. Ido, B. Lev, A. D. Ludlow, B. C. Sawyer, B. Stuhl, and T. Zelinsky, *Precision measurement based on ultracold atoms and cold molecules*, Int. J. Mod. Phys. D **16**, 2481–2494 (2007).

[6] J. J. Hudson, D. M. Kara, I. J. Smallman, B. E. Sauer, M. R. Tarbutt, and E. A. Hinds, *Improved measurement of the shape of the electron*, Nature **473**, 493 (2011).

[7] D. Jaksch, C. Bruder, J. I. Cirac, C. W. Gardiner, and P. Zoller, *Cold Bosonic Atoms in Optical Lattices*, Phys. Rev. Lett. **81**, 3108–3111 (1998).

[8] Maciej Lewenstein, Anna Sanpera, Veronica Ahufinger, Bogdan Damski, Aditi Sen(De), and Ujjwal Sen, *Ultracold atomic gases in optical lattices: mimicking condensed matter physics and beyond*, Adv. Phys. **56**, 243–379 (2007).

[9] Immanuel Bloch, Jean Dalibard, and Wilhelm Zwerger, *Many-body physics with ultracold gases*, Rev. Mod. Phys. **80**, 885–964 (2008).

[10] H. Häffner, C.F. Roos, and R. Blatt, *Quantum computing with trapped ions*, Phys. Rep. **469**, 155 – 203 (2008).

[11] Antonio Negretti, Philipp Treutlein, and Tommaso Calarco, *Quantum computing implementations with neutral particles*, Quant. Inf. Proc. **10**, 721–753 (2011).

[12] Andrei Derevianko and Hidetoshi Katori, *Colloquium : Physics of optical lattice clocks*, Rev. Mod. Phys. **83**, 331–347 (2011).

[13] Gretchen K. Campbell and William D. Phillips, *Ultracold atoms and precise time standards*, Philos. T. Roy. Soc. A **369**, 4078–4089 (2011).

[14] T. F. Gallagher, **Rydberg Atoms** (Cambridge University Press, 1994).

[15] J.-H. Choi, B. Knuffman, T. Cubel Liebisch, A. Reinhard, and G. Raithel. *Cold Rydberg Atoms.* volume 54 of *Advances In Atomic, Molecular, and Optical Physics*, pages 131 – 202. Academic Press, 2006.

[16] Robert Löw, Hendrik Weimer, Johannes Nipper, Jonathan B Balewski, Björn Butscher, Hans Peter Büchler, and Tilman Pfau, *An experimental and theoretical guide to strongly interacting Rydberg gases*, J. Phys. B **45**, 113001 (2012).

[17] Thomas F. Gallagher and Pierre Pillet. *Dipole-Dipole Interactions of Rydberg Atoms.* in Arimondo *et al.*, editor, **Advances in Atomic, Molecular, and Optical Physics**, volume 56 of *Advances In Atomic, Molecular, and Optical Physics*, pages 161 – 218. Academic Press, 2008.

[18] M. Marinescu and A. Dalgarno, *Dispersion forces and long-range electronic transition dipole moments of alkali-metal dimer excited states*, Phys. Rev. A **52**, 311–328 (1995).

[19] M. Marinescu, *Dispersion coefficients for the np-np asymptote of homonuclear alkali-metal dimers*, Phys. Rev. A **56**, 4764–4773 (1997).

[20] Kilian Singer, Jovica Stanojevic, Matthias Weidemüller, and Robin Côté, *Long-range interactions between alkali Rydberg atom pairs correlated to the ns-ns, np-np and nd-nd asymptotes*, J. Phys. B **38**, S295 (2005).

[21] T. G. Walker and M. Saffman, *Zeros of Rydberg-Rydberg Föster interactions*, J. Phys. B **38**, S309 (2005).

[22] A. Reinhard, T. Cubel Liebisch, B. Knuffman, and G. Raithel, *Level shifts of rubidium Rydberg states due to binary interactions*, Phys. Rev. A **75**, 032712 (2007).

[23] Thad G. Walker and M. Saffman, *Consequences of Zeeman degeneracy for the van der Waals blockade between Rydberg atoms*, Phys. Rev. A **77**, 032723 (2008).

[24] W. R. Anderson, J. R. Veale, and T. F. Gallagher, *Resonant Dipole-Dipole Energy Transfer in a Nearly Frozen Rydberg Gas*, Phys. Rev. Lett. **80**, 249–252 (1998).

[25] Thibault Vogt, Matthieu Viteau, Amodsen Chotia, Jianming Zhao, Daniel Comparat, and Pierre Pillet, *Electric-Field Induced Dipole Blockade with Rydberg Atoms*, Phys. Rev. Lett. **99**, 073002 (2007).

[26] P. Bohlouli-Zanjani, J. A. Petrus, and J. D. D. Martin, *Enhancement of Rydberg Atom Interactions Using ac Stark Shifts*, Phys. Rev. Lett. **98**, 203005 (2007).

[27] J. A. Petrus, P. Bohlouli-Zanjani, and J. D. D. Martin, *ac electric-field-induced resonant energy transfer between cold Rydberg atoms*, J. Phys. B **41**, 245001 (2008).

[28] E. Urban, T. A. Johnson, T. Henage, L. Isenhower, D. D. Yavuz, T. G. Walker, and M. Saffman, *Observation of Rydberg blockade between two atoms*, Nature Phys. **5**, 110–114 (2009).

[29] A. Gaetan, Y. Miroshnychenko, T. Wilk, A. Chotia, M. Viteau, D. Comparat, P. Pillet, A. Browaeys, and P. Grangier, *Observation of collective excitation of two individual atoms in the Rydberg blockade regime*, Nature Phys. **5**, 115–118 (2009).

[30] M. Saffman and T. G. Walker, *Creating single-atom and single-photon sources from entangled atomic ensembles*, Phys. Rev. A **66**, 065403 (2002).

[31] Y. O. Dudin and A. Kuzmich, *Strongly Interacting Rydberg Excitations of a Cold Atomic Gas*, Science **336**, 887–889 (2012).

[32] D. Jaksch, J. I. Cirac, P. Zoller, S. L. Rolston, R. Côté, and M. D. Lukin, *Fast quantum gates for neutral atoms*, Phys. Rev. Lett. **85**, 2208–2211 (2000).

[33] M. Saffman and T. G. Walker, *Analysis of a quantum logic device based on dipole-dipole interactions of optically trapped Rydberg atoms*, Phys. Rev. A **72**, 022347 (2005).

[34] E. Brion, L. H. Pedersen, and K. Mølmer, *Implementing a neutral atom Rydberg gate without populating the Rydberg state*, J. Phys. B **40**, S159 (2007).

[35] L. Isenhower, E. Urban, X. L. Zhang, A. T. Gill, T. Henage, T. A. Johnson, T. G. Walker, and M. Saffman, *Demonstration of a Neutral Atom Controlled-NOT Quantum Gate*, Phys. Rev. Lett. **104**, 010503 (2010).

[36] M. Saffman, T. G. Walker, and K. Mølmer, *Quantum information with Rydberg atoms*, Rev. Mod. Phys. **82**, 2313–2363 (2010).

[37] M. D. Lukin, M. Fleischhauer, R. Cote, L. M. Duan, D. Jaksch, J. I. Cirac, and P. Zoller, *Dipole Blockade and Quantum Information Processing in Mesoscopic Atomic Ensembles*, Phys. Rev. Lett. **87**, 037901 (2001).

[38] R. G. Unanyan and M. Fleischhauer, *Efficient and robust entanglement generation in a many-particle system with resonant dipole-dipole interactions*, Phys. Rev. A **66**, 032109 (2002).

[39] Ditte Møller, Lars Bojer Madsen, and Klaus Mølmer, *Quantum Gates and Multiparticle Entanglement by Rydberg Excitation Blockade and Adiabatic Passage*, Phys. Rev. Lett. **100**, 170504 (2008).

[40] M. Saffman and K. Mølmer, *Efficient Multiparticle Entanglement via Asymmetric Rydberg Blockade*, Phys. Rev. Lett. **102**, 240502 (2009).

[41] M. Müller, I. Lesanovsky, H. Weimer, H. P. Büchler, and P. Zoller, *Mesoscopic Rydberg Gate Based on Electromagnetically Induced Transparency*, Phys. Rev. Lett. **102**, 170502 (2009).

[42] M. Saffman and T. G. Walker, *Entangling single- and N-atom qubits for fast quantum state detection and transmission*, Phys. Rev. A **72**, 042302 (2005).

[43] E. Brion, K. Mølmer, and M. Saffman, *Quantum Computing with Collective Ensembles of Multilevel Systems*, Phys. Rev. Lett. **99**, 260501 (2007).

[44] Hendrik Weimer, Markus Müller, Igor Lesanovsky, Peter Zoller, and Hans Peter Büchler, *A Rydberg quantum simulator*, Nature Phys. **6**, 382–388 (2010).

[45] H. Weimer, M. Müller, H. Büchler, and I. Lesanovsky, *Digital quantum simulation with Rydberg atoms*, Quant. Inf. Proc. **10**, 885–906 (2011).

[46] Chris H. Greene, A. S. Dickinson, and H. R. Sadeghpour, *Creation of Polar and Nonpolar Ultra-Long-Range Rydberg Molecules*, Phys. Rev. Lett. **85**, 2458–2461 (2000).

[47] A. A. Khuskivadze, M. I. Chibisov, and I. I. Fabrikant, *Adiabatic energy levels and electric dipole moments of Rydberg states of Rb_2 and Cs_2 dimers*, Phys. Rev. A **66**, 042709 (2002).

[48] Chris H. Greene, Edward L. Hamilton, Heather Crowell, Cedomil Vadla, and Kay Niemax, *Experimental Verification of Minima in Excited Long-Range Rydberg States of Rb_2*, Phys. Rev. Lett. **97**, 233002 (2006).

[49] Vera Bendkowsky, Bjorn Butscher, Johannes Nipper, James P. Shaffer, Robert Low, and Tilman Pfau, *Observation of ultralong-range Rydberg molecules*, Nature **458**, 1005–1008 (2009).

[50] Christophe Boisseau, Ionel Simbotin, and Robin Côté, *Macrodimers: Ultralong Range Rydberg Molecules*, Phys. Rev. Lett. **88**, 133004 (2002).

[51] Arne Schwettmann, K. Richard Overstreet, Jonathan Tallant, and James P. Shaffer, *Analysis of long-range Cs Rydberg potential wells*, J. Mod. Opt. **54**, 2551–2562 (2007).

[52] Nolan Samboy and Robin Ct, *Rubidium Rydberg macrodimers*, J. Phys. B **44**, 184006 (2011).

[53] Nolan Samboy, Jovica Stanojevic, and Robin Côté, *Formation and properties of Rydberg macrodimers*, Phys. Rev. A **83**, 050501 (2011).

[54] K. R. Overstreet, A. Schwettmann, J. Tallant, D. Booth, and J. P. Shaffer, *Observation of electric-field-induced Cs Rydberg atom macrodimers*, Nature Phys. **5**, 581–585 (2009).

[55] Hendrik Weimer, Robert Löw, Tilman Pfau, and Hans Peter Büchler, *Quantum Critical Behavior in Strongly Interacting Rydberg Gases*, Phys. Rev. Lett. **101**, 250601 (2008).

[56] J Schachenmayer, I Lesanovsky, A Micheli, and A J Daley, *Dynamical crystal creation with polar molecules or Rydberg atoms in optical lattices*, New J. Phys. **12**, 103044 (2010).

[57] R M W van Bijnen, S Smit, K A H van Leeuwen, E J D Vredenbregt, and S J J M F Kokkelmans, *Adiabatic formation of Rydberg crystals with chirped laser pulses*, J. Phys. B **44**, 184008 (2011).

[58] M. Gärttner, K. P. Heeg, T. Gasenzer, and J. Evers, *Finite-size effects in strongly interacting Rydberg gases*, Phys. Rev. A **86**, 033422 (2012).

[59] C. Ates and I. Lesanovsky, *Entropic enhancement of spatial correlations in a laser-driven rydberg gas*, Phys. Rev. A **86**, 013408 (2012).

[60] Peter Schau, Marc Cheneau, Manuel Endres, Takeshi Fukuhara, Sebastian Hild, Ahmed Omran, Thomas Pohl, Christian Gross, Stefan Kuhr, and Immanuel Bloch, *Observation of spatially ordered structures in a two-dimensional Rydberg gas*, Nature **491**, 87–91 (2012).

[61] F. Robicheaux and J. V. Hernández, *Many-body wave function in a dipole blockade configuration*, Phys. Rev. A **72**, 063403 (2005).

[62] K. C. Younge, A. Reinhard, T. Pohl, P. R. Berman, and G. Raithel, *Mesoscopic Rydberg ensembles: Beyond the pairwise-interaction approximation*, Phys. Rev. A **79**, 043420 (2009).

[63] U. Schollwöck, *The density-matrix renormalization group*, Rev. Mod. Phys. **77**, 259–315 (2005).

[64] Ulrich Schollwöck, *The density-matrix renormalization group in the age of matrix product states*, Ann. Phys. **326**, 96 – 192 (2011).

[65] J Ignacio Cirac and Frank Verstraete, *Renormalization and tensor product states in spin chains and lattices*, J. Phys. A **42**, 504004 (2009).

[66] F. Verstraete and J. I. Cirac, *Renormalization algorithms for Quantum-Many Body Systems in two and higher dimensions*, arXiv:cond-mat/0407066 (2004).

[67] Peter J. Mohr, Barry N. Taylor, and David B. Newell, *CODATA recommended values of the fundamental physical constants: 2006*, Rev. Mod. Phys. **80**, 633–730 (2008).

[68] H. A. Bethe and E. E. Salpeter, **Quantum Mechanics of One- and Two-Electron Atoms** (Dover Publications, 1977).

[69] M. J. Seaton, *Quantum defect theory*, Rep. Prog. Phys. **46**, 167 (1983).

[70] C. Greene, U. Fano, and G. Strinati, *General form of the quantum-defect theory*, Phys. Rev. A **19**, 1485–1509 (1979).

[71] C. H. Greene, A. R. P. Rau, and U. Fano, *General form of the quantum-defect theory. II*, Phys. Rev. A **26**, 2441–2459 (1982).

[72] Mireille Aymar, Chris H. Greene, and Eliane Luc-Koenig, *Multichannel Rydberg spectroscopy of complex atoms*, Rev. Mod. Phys. **68**, 1015–1123 (1996).

[73] L. Santos, G. V. Shlyapnikov, P. Zoller, and M. Lewenstein, *Bose-Einstein Condensation in Trapped Dipolar Gases*, Phys. Rev. Lett. **85**, 1791–1794 (2000).

[74] G. Pupillo, A. Micheli, M. Boninsegni, I. Lesanovsky, and P. Zoller, *Strongly Correlated Gases of Rydberg-Dressed Atoms: Quantum and Classical Dynamics*, Phys. Rev. Lett. **104**, 223002 (2010).

[75] B. Vaucher, S. J. Thwaite, and D. Jaksch, *Ultralarge Rydberg dimers in optical lattices*, Phys. Rev. A **78**, 043415 (2008).

[76] Lincoln D Carr, David DeMille, Roman V Krems, and Jun Ye, *Cold and ultracold molecules: science, technology and applications*, New J. Phys. **11**, 055049 (2009).

[77] O Dulieu and C Gabbanini, *The formation and interactions of cold and ultracold molecules: new challenges for interdisciplinary physics*, Rep. Prog. Phys. **72**, 086401 (2009).

[78] Cheng Chin, V V Flambaum, and M G Kozlov, *Ultracold molecules: new probes on the variation of fundamental constants*, New J. Phys. **11**, 055048 (2009).

[79] A. Micheli, G. K. Brennen, and P. Zoller, *A toolbox for lattice-spin models with polar molecules*, Nature Phys. **2**, 341–347 (2006).

[80] Alexey V. Gorshkov, Salvatore R. Manmana, Gang Chen, Jun Ye, Eugene Demler, Mikhail D. Lukin, and Ana Maria Rey, *Tunable Superfluidity and Quantum Magnetism with Ultracold Polar Molecules*, Phys. Rev. Lett. **107**, 115301 (2011).

[81] Peter W. Graham and Surjeet Rajendran, *Axion dark matter detection with cold molecules*, Phys. Rev. D **84**, 055013 (2011).

[82] E. S. Shuman, J. F. Barry, and D. DeMille, *Laser cooling of a diatomic molecule*, Nature **467**, 820–823 (2010).

[83] Markus Kowalewski, Giovanna Morigi, Pepijn W. H. Pinkse, and Regina de Vivie-Riedle, *Cavity sideband cooling of trapped molecules*, Phys. Rev. A **84**, 033408 (2011).

[84] L. R. Hunter, S. K. Peck, A. S. Greenspon, S. Saad Alam, and D. DeMille, *Prospects for laser cooling TlF*, Phys. Rev. A **85**, 012511 (2012).

[85] Samuel A Meek, Horst Conrad, and Gerard Meijer, *A Stark decelerator on a chip*, New J. Phys. **11**, 055024 (2009).

[86] Nicholas R. Hutzler, Hsin-I Lu, and John M. Doyle, *The Buffer Gas Beam: An Intense, Cold, and Slow Source for Atoms and Molecules*, Chem. Rev. **112**, 4803–4827 (2012).

[87] Sebastiaan Y. T. van de Meerakker, Hendrick L. Bethlem, Nicolas Vanhaecke, and Gerard Meijer, *Manipulation and Control of Molecular Beams*, Chem. Rev. **112**, 4828–4878 (2012).

[88] Jeremy M. Hutson and Pavel Soldàn, *Molecule formation in ultracold atomic gases*, Int. Rev. Phys. Chem. **25**, 497–526 (2006).

[89] S. M. Farooqi, D. Tong, S. Krishnan, J. Stanojevic, Y. P. Zhang, J. R. Ensher, A. S. Estrin, C. Boisseau, R. Côté, E. E. Eyler, and P. L. Gould, *Long-Range Molecular Resonances in a Cold Rydberg Gas*, Phys. Rev. Lett. **91**, 183002 (2003).

[90] R. J. Le Roy, *Long-range potential coefficients from RKR turning points: C_6 and C_8 for $B(^3\Pi_{0u}^+)$-state Cl_3, Br_2, and I_2*, Can. J. Phys. **52**, 246 (1974).

[91] Peter W. Atkins and Ronald S. Friedman, **Molecular Quantum Mechanics** (Oxford University Press, Oxford, United Kingdom, 2005).

[92] J. Sebby-Strabley, M. Anderlini, P. S. Jessen, and J. V. Porto, *Lattice of double wells for manipulating pairs of cold atoms*, Phys. Rev. A **73**, 033605 (2006).

[93] J. C. Slater, **Quantum Theory of Molecules and Solids** (McGraw-Hill, 1974).

[94] J. Stanojevic, R. Côté, D. Tong, E. E. Eyler, and P. L. Gould, *Long-range potentials and* $(n-1)d+ns$ *molecular resonances in an ultracold Rydberg gas*, Phys. Rev. A **78**, 052709 (2008).

[95] J. Stanojevic, R. Côté, D. Tong, E. E. Eyler, and P. L. Gould, *Long-range Rydberg-Rydberg interactions and molecular resonances*, Eur. Phys. J. D **30**, 3–12 (2006).

[96] A V Stolyarov and M S Child, *Radiative properties of diatomic Rydberg states in quantum defect theory. Application to the hydrogen molecule*, J. Phys. B **32**, 527–535 (1999).

[97] B. G. Wilson, C. Iglesias, and F. Rogers, *Near-threshold photoabsorption cross sections for nonhydrogenic ions*, Phys. Rev. A **38**, 4633– (1988).

[98] Robert J. Buehler and Joseph O. Hirschfelder, *Bipolar Expansion of Coulombic Potentials*, Phys. Rev. **83**, 628–633 (1951).

[99] J. Fernández Rico, R. López, G. Ramírez, and C. Tablero, *Exchange integrals: Comparison of numerical and analytical procedures*, Phys. Rev. A **49**, 3381–(1994).

[100] Michael P. Barnett, *Molecular integrals and information processing*, Int. J. Quantum Chem. **95**, 791–805 (2003).

[101] Michael P. Barnett, *Mathscape and molecular integrals*, J. Symb. Comput. **42**, 265–289 (2007).

[102] E. Toth, A. M. Rey, and P. B. Blakie, *Theory of correlations between ultracold bosons released from an optical lattice*, Phys. Rev. A **78**, 013627 (2008).

[103] G Vitrant, J M Raimond, M Gross, and S Haroche, *Rydberg to plasma evolution in a dense gas of very excited atoms*, J. Phys. B **15**, L49 (1982).

[104] M. P. Robinson, B. Laburthe Tolra, Michael W. Noel, T. F. Gallagher, and P. Pillet, *Spontaneous Evolution of Rydberg Atoms into an Ultracold Plasma*, Phys. Rev. Lett. **85**, 4466–4469 (2000).

[105] S. K. Dutta, D. Feldbaum, A. Walz-Flannigan, J. R. Guest, and G. Raithel, *High-Angular-Momentum States in Cold Rydberg Gases*, Phys. Rev. Lett. **86**, 3993–3996 (2001).

[106] Wenhui Li, Michael W. Noel, Michael P. Robinson, Paul J. Tanner, Thomas F. Gallagher, Daniel Comparat, Bruno Laburthe Tolra, Nicolas Vanhaecke, Thibault Vogt, Nassim Zahzam, Pierre Pillet, and Duncan A. Tate, *Evolution dynamics of a dense frozen Rydberg gas to plasma*, Phys. Rev. A **70**, 042713 (2004).

[107] I I Beterov, D B Tretyakov, I I Ryabtsev, V M Entin, A Ekers, and N N Bezuglov, *Ionization of Rydberg atoms by blackbody radiation*, New J. Phys. **11**, 013052 (2009).

[108] Wenhui Li, Paul J. Tanner, and T. F. Gallagher, *Dipole-Dipole Excitation and Ionization in an Ultracold Gas of Rydberg Atoms*, Phys. Rev. Lett. **94**, 173001 (2005).

[109] B. Knuffman and G. Raithel, *Emission of fast atoms from a cold Rydberg gas*, Phys. Rev. A **73**, 020704 (2006).

[110] T. Amthor, M. Reetz-Lamour, S. Westermann, J. Denskat, and M. Weidemüller, *Mechanical Effect of van der Waals Interactions Observed in Real Time in an Ultracold Rydberg Gas*, Phys. Rev. Lett. **98**, 023004 (2007).

[111] Matthieu Viteau, Amodsen Chotia, Daniel Comparat, Duncan A. Tate, T. F. Gallagher, and Pierre Pillet, *Melting a frozen Rydberg gas with an attractive potential*, Phys. Rev. A **78**, 040704 (2008).

[112] Linjie Zhang, Zhigang Feng, Jianming Zhao, Changyong Li, and Suotang Jia, *Many-Body Ionization of a Dense Rydberg Gas in Repulsive Potential*, J. Phys. Soc. Jpn. **79**, 054301 (2010).

[113] Hyunwook Park, E. S. Shuman, and T. F. Gallagher, *Ionization of Rb Rydberg atoms in the attractive ns-np dipole-dipole potential*, Phys. Rev. A **84**, 052708 (2011).

[114] T. Amthor, J. Denskat, C. Giese, N. N. Bezuglov, A. Ekers, L. S. Cederbaum, and M. Weidemüller, *Autoionization of an ultracold Rydberg gas through resonant dipole coupling*, Eur. Phys. J. D **53**, 329–335 (2009).

[115] Paul J. Tanner, Jianing Han, E. S. Shuman, and T. F. Gallagher, *Many-Body Ionization in a Frozen Rydberg Gas*, Phys. Rev. Lett. **100**, 043002 (2008).

[116] Vitali Averbukh, Imke B. Müller, and Lorenz S. Cederbaum, *Mechanism of Interatomic Coulombic Decay in Clusters*, Phys. Rev. Lett. **93**, 263002 (2004).

[117] H. P. Büchler, E. Demler, M. Lukin, A. Micheli, N. Prokof'ev, G. Pupillo, and P. Zoller, *Strongly Correlated 2D Quantum Phases with Cold Polar Molecules: Controlling the Shape of the Interaction Potential*, Phys. Rev. Lett. **98**, 060404 (2007).

[118] A. Micheli, G. Pupillo, H. P. Büchler, and P. Zoller, *Cold polar molecules in two-dimensional traps: Tailoring interactions with external fields for novel quantum phases*, Phys. Rev. A **76**, 043604 (2007).

[119] H. P. Büchler, A. Micheli, and P. Zoller, *Three-body interactions with cold polar molecules*, Nature Phys. **3**, 726–731 (2007).

[120] L. Bonnes, H. Büchler, and S. Wessel, *Polar molecules with three-body interactions on the honeycomb lattice*, New J. Phys. **12** (2010).

[121] L. Bonnes and S. Wessel, *Supersolid polar molecules beyond pairwise interactions*, Phys. Rev. B **83** (2011).

[122] Emanuele G. Dalla Torre, Erez Berg, and Ehud Altman, *Hidden Order in 1D Bose Insulators*, Phys. Rev. Lett. **97**, 260401 (2006).

[123] N. R. Cooper and G. V. Shlyapnikov, *Stable Topological Superfluid Phase of Ultracold Polar Fermionic Molecules*, Phys. Rev. Lett. **103**, 155302 (2009).

[124] S. G. Bhongale, L. Mathey, Shan-Wen Tsai, Charles W. Clark, and Erhai Zhao, *Bond Order Solid of Two-Dimensional Dipolar Fermions*, Phys. Rev. Lett. **108**, 145301 (2012).

[125] C. Trefzger, C. Menotti, B. Capogrosso-Sansone, and M. Lewenstein, *Ultracold dipolar gases in optical lattices*, J. Phys. B **44**, 193001 (2011).

[126] K. Góral, L. Santos, and M. Lewenstein, *Quantum phases of dipolar bosons in optical lattices*, Phys. Rev. Lett. **88**, 170406 (2002).

[127] L. Pollet, J. D. Picon, H. P. Büchler, and M. Troyer, *Supersolid Phase with Cold Polar Molecules on a Triangular Lattice*, Phys. Rev. Lett. **104**, 125302 (2010).

[128] B. Capogrosso-Sansone, C. Trefzger, M. Lewenstein, P. Zoller, and G. Pupillo, *Quantum Phases of Cold Polar Molecules in 2D Optical Lattices*, Phys. Rev. Lett. **104**, 125301 (2010).

[129] M.A. Baranov, *Theoretical progress in many-body physics with ultracold dipolar gases*, Phys. Rep. **464**, 71 – 111 (2008).

[130] T. Lahaye, J. Metz, T. Koch, B. Fröhlich, A. Griesmaier, and T. Pfau, *A purely dipolar quantum gas*, in R. Cote, P. L. Gould, M. G. Rozman, and W. W. Smith, editors, **PUSHING THE FRONTIERS OF ATOMIC PHYSICS, Proceedings of the XXI International Conference on Atomic Physics** 2009).

[131] Axel Griesmaier, Jörg Werner, Sven Hensler, Jürgen Stuhler, and Tilman Pfau, *Bose-Einstein Condensation of Chromium*, Phys. Rev. Lett. **94**, 160401 (2005).

[132] Mingwu Lu, Nathaniel Q. Burdick, Seo Ho Youn, and Benjamin L. Lev, *Strongly Dipolar Bose-Einstein Condensate of Dysprosium*, Phys. Rev. Lett. **107**, 190401 (2011).

[133] Thierry Lahaye, Tobias Koch, Bernd Frohlich, Marco Fattori, Jonas Metz, Axel Griesmaier, Stefano Giovanazzi, and Tilman Pfau, *Strong dipolar effects in a quantum ferrofluid*, Nature **448**, 672–675 (2007).

[134] A. W. Glaetzle, R. Nath, B. Zhao, G. Pupillo, and P. Zoller, *Driven-dissipative dynamics of a strongly interacting Rydberg gas*, Phys. Rev. A **86**, 043403 (2012).

[135] G. E. Astrakharchik, J. Boronat, I. L. Kurbakov, and Yu. E. Lozovik, *Quantum Phase Transition in a Two-Dimensional System of Dipoles*, Phys. Rev. Lett. **98**, 060405 (2007).

[136] G. Pupillo, A. Micheli, M. Boninsegni, I. Lesanovsky, and P. Zoller, *Mesoscopic phases of dipolar ensembles with polar molecules and Rydberg atoms*, arXiv:0904.2735 (2009).

[137] Yu.E. Lozovik and E.A. Rakoch, *Structure and melting of dipole clusters*, Phys. Lett. A **235**, 55 – 64 (1997).

[138] A. I. Belousov and Y. E. Lozovik, *Mesoscopic and macroscopic dipole clusters: Structure and phase transitions*, Eur. Phys. J. D **8**, 251–264 (2000).

[139] Myron L. Zimmerman, Michael G. Littman, Michael M. Kash, and Daniel Kleppner, *Stark structure of the Rydberg states of alkali-metal atoms*, Phys. Rev. A **20**, 2251–2275 (1979).

[140] B. M. Smirnov, **Physics of Atoms and Ions** (Springer, 2003).

[141] J. E. Johnson and S. L. Rolston, *Interactions between Rydberg-dressed atoms*, Phys. Rev. A **82**, 033412 (2010).

[142] Claude Cohen-Tannoudji, Jacques Dupont-Roc, and Gilbert Grynberg, **Atom-Photon Interactions: Basic Processes and Applications** (Wiley-VCH, 2004).

[143] R. Dum, A. S. Parkins, P. Zoller, and C. W. Gardiner, *Monte Carlo simulation of master equations in quantum optics for vacuum, thermal, and squeezed reservoirs*, Phys. Rev. A **46**, 4382–4396 (1992).

[144] R. Dum, P. Zoller, and H. Ritsch, *Monte Carlo simulation of the atomic master equation for spontaneous emission*, Phys. Rev. A **45**, 4879–4887 (1992).

[145] Howard Carmichael, **An Open Systems Approach to Quantum Optics** (Springer-Verlag, 1993).

[146] Klaus Mølmer, Yvan Castin, and Jean Dalibard, *Monte Carlo wave-function method in quantum optics*, J. Opt. Soc. Am. B **10**, 524–538 (1993).

[147] M. B. Plenio and P. L. Knight, *The quantum-jump approach to dissipative dynamics in quantum optics*, Rev. Mod. Phys. **70**, 101–144 (1998).

[148] P.-L. Giscard, S. J. Thwaite, and D. Jaksch, *Continued Fractions and Unique Factorization on Quivers*, arXiv:1202.5523 (2012).

[149] N. Biggs, **Algebraic Graph Theory** (Cambridge University Press, Cambridge, 2nd edition, 1993).

[150] Reinhard Diestel, **Graph Theory** (Springer-Verlag, 2010).

[151] G.H. Hardy and E.M. Wright, **An introduction to the theory of numbers** (Oxford University Press, 5th edition, 1979).

[152] A. Cayley, *XIII. On certain results relating to quaternions*, Philos. Mag. Ser. 3 **3**, 141–145 (1845).

[153] E. Study, *Zur Theorie der linearen Gleichungen*, Act. Math. **42**, 1–61 (1920).

[154] A. Heyting, *Die Theorie der linearen Gleichungen in einer Zahlenspezies mit nichtkommutativer Multiplikation*, Math. Ann. **98**, 465–490 (1928).

[155] A.R. Richardson, *Simultaneous linear equations over a division algebra*, Proc. London Math. Soc. **55**, 395–420 (1928).

[156] Oystein Ore, *Linear equations in non-commutative fields*, Ann. Math. **32**, pp. 463–477 (1931).

[157] I. M. Gel'fand and V. S. Retakh, *Determinants of matrices over noncommutative rings*, Funct. Anal. Appl. **25**, 91–102 (1991).

[158] I. M. Gel'fand and V. S. Retakh, *A theory of noncommutative determinants and characteristic functions of graphs*, Funct. Anal. Appl. **26**, 231–246 (1992).

[159] I. Gelfand and V. Retakh, *Quasideterminants, I*, Sel. Math. - New Ser. **3**, 517–546 (1997).

[160] Israel Gelfand, Sergei Gelfand, Vladimir Retakh, and Robert Lee Wilson, *Quasideterminants*, Adv. Math. **193**, 56 – 141 (2005).

[161] P.-L. Giscard, S. J. Thwaite, and D. Jaksch, *Evaluating matrix functions by resummations on graphs: the method of path-sums*, arXiv:1112.1588 (2012).

[162] *The On-Line Encyclopedia of Integer Sequences*, 2012. http://oeis.org/.

[163] Ranjan K. Mallik, *The inverse of a tridiagonal matrix*, Linear Algebra Appl. **325**, 109 – 139 (2001).

[164] Emrah Kılıç, *Explicit formula for the inverse of a tridiagonal matrix by backward continued fractions*, Appl. Math. Comput. **197**, 345 – 357 (2008).

[165] Hans Richter, *Zum logarithmus einer matrix*, Arch. Math. **2**, 360–363 (1949).

[166] A. Wouk, *Integral representation of the logarithm of matrices and operators*, J. Math. Anal. Appl. **11**, 131–138 (1965).

[167] Nicholas J. Higham, **Functions of Matrices: theory and computation** (SIAM, Philadelphia, PA, USA, 2008).

[168] M. P. Drazin, *Pseudo-Inverses in Associative Rings and Semigroups*, Am. Math. Mon. **65**, pp. 506–514 (1958).

[169] Stephen L. Campbell and Carl D. Meyer, **Generalized inverses of linear transformations** (SIAM, 2009).

[170] P.-L. Giscard and D. Jaksch, *Tunable Supersolids of Rydberg Excitations Described by Quantum Evolutions on Graphs*, arXiv:1108:1177 (2011).

[171] P.-L. Giscard, M. Kiffner, and D. Jaksch, *The walk-sum method for simulating quantum many-body systems*, arXiv:1204:5087 (2012).

[172] Michele Benzi and Gene H. Golub, *Bounds for the entries of matrix functions with applications to preconditioning*, BIT **39**, 417–438 (1999).

[173] Arieh Iserles, *How large is the exponential of a banded matrix?*, New Zealand J. Math. **29**, 177–192 (2000).

[174] M. Cramer and J. Eisert, *Correlations, spectral gap and entanglement in harmonic quantum systems on generic lattices*, New J. Phys. **8**, 71 (2006).

[175] M. Benzi and N. Razouk, *Decay bounds and O(n) algorithms for approximating functions of sparse matrices*, Electron. Trans. Numer. Anal. **28**, 16–39 (2007).

[176] M. Benzi, P. Boito, and N. Razouk, *Decay properties of spectral projectors with applications to electronic structure*, arXiv:1203.3953 (2012).

[177] V D Ovsiannikov, I L Glukhov, and E A Nekipelov, *Rates of blackbody radiation-induced transitions from Rydberg states of alkali atoms*, J. Phys. B **44**, 195010 (2011).

[178] E. T. Whittaker and G. N. Watson, **A course of modern analysis : an introduction to the general theory of infinite processes and of analytic functions, with an account of the principal transcendental functions** (Cambridge University Press, 1927).

[179] L. J. Slater, **Confluent Hypergeometric Functions** (Cambridge University Press, 1960).

[180] H. Buchholz, **The confluent hypergeometric function: with special emphasis on its applications** (Berlin: Springer-Verlag, 1969).

[181] Z. X. Wang and D. R. Guo, **Special Functions** (World Scientific Publishing Co., 1989).

[182] National Institute of Standards and Technology from http://dlmf.nist.gov/. *Digital library of mathematical functions*, updated 2012-03-23.

[183] M. J. Seaton, *The Quantum Defect Method*, Mon. Not. R. Astron. Soc. **118**, 504 (1958).

[184] M. J. Seaton, *Quantum defect theory I. General formulation*, Proc. Phys. Soc. (London) **88**, 801 (1966).

[185] M.J. Seaton, *Coulomb functions for attractive and repulsive potentials and for positive and negative energies*, Comput. Phys. Commun. **146**, 225 – 249 (2002).